Universidade Federal de Goiás
Instituto de Física
Programa de Pós-Graduação em Física

Daniel Araújo de Azevedo

Phenomenological Study of Neutrino Invisible Decay on MINOS and MINOS+ Experiments

Estudo Fenomenológico de Decaimento Invisível de Neutrinos nos Experimentos MINOS e MINOS+

GOIÂNIA

2025

UNIVERSIDADE FEDERAL DE GOIÁS
INSTITUTO DE FÍSICA

TERMO DE CIÊNCIA E DE AUTORIZAÇÃO (TECA) PARA DISPONIBILIZAR VERSÕES ELETRÔNICAS DE TESES

E DISSERTAÇÕES NA BIBLIOTECA DIGITAL DA UFG

Na qualidade de titular dos direitos de autor, autorizo a Universidade Federal de Goiás (UFG) a disponibilizar, gratuitamente, por meio da Biblioteca Digital de Teses e Dissertações (BDTD/UFG), regulamentada pela Resolução CEPEC nº 832/2007, sem ressarcimento dos direitos autorais, de acordo com a Lei 9.610/98, o documento conforme permissões assinaladas abaixo, para fins de leitura, impressão e/ou download, a título de divulgação da produção científica brasileira, a partir desta data.

O conteúdo das Teses e Dissertações disponibilizado na BDTD/UFG é de responsabilidade exclusiva do autor. Ao encaminhar o produto final, o autor(a) e o(a) orientador(a) firmam o compromisso de que o trabalho não contém nenhuma violação de quaisquer direitos autorais ou outro direito de terceiros.

1. Identificação do material bibliográfico

[X] Dissertação [ ] Tese [ ] Outro*:_____

*No caso de mestrado/doutorado profissional, indique o formato do Trabalho de Conclusão de Curso, permitido no documento de área, correspondente ao programa de pós-graduação, orientado pela legislação vigente da CAPES.

Exemplos: Estudo de caso ou Revisão sistemática ou outros formatos.

2. Nome completo do autor

Daniel Araújo de Azevedo

3. Título do trabalho

Phenomenological study of neutrino invisible decay on MINOS and MINOS+ experiments

4. Informações de acesso ao documento (este campo deve ser preenchido pelo orientador)

Concorda com a liberação total do documento [X] SIM [ ] NÃO[1]

[1] Neste caso o documento será embargado por até um ano a partir da data de defesa. Após esse período, a possível disponibilização ocorrerá apenas mediante:
a) consulta ao(à) autor(a) e ao(à) orientador(a);
b) novo Termo de Ciência e de Autorização (TECA) assinado e inserido no arquivo da tese ou dissertação.
O documento não será disponibilizado durante o período de embargo.
Casos de embargo:
- Solicitação de registro de patente;
- Submissão de artigo em revista científica;
- Publicação como capítulo de livro;
- Publicação da dissertação/tese em livro.

Obs. Este termo deverá ser assinado no SEI pelo orientador e pelo autor.

Documento assinado eletronicamente por **Ricardo Avelino Gomes**, **Professor do Magistério Superior**, em 30/04/2025, às 08:48, conforme horário oficial de Brasília, com fundamento no § 3º do art. 4º do Decreto nº 10.543, de 13 de novembro de 2020 .

Documento assinado eletronicamente por **Daniel Araújo De Azevedo**, **Discente**, em 30/04/2025, às 12:10, conforme horário oficial de Brasília, com fundamento no § 3º do art. 4º do Decreto nº 10.543, de 13 de novembro de 2020.

A autenticidade deste documento pode ser conferida no site https://sei.ufg.br/sei/controlador_externo.php?acao=documento_conferir&id_orgao_acesso_externo=0, informando o código verificador **5341857** e o código CRC **AC7537DB**.

Referência: Processo nº 23070.017231/2025-91 SEI nº 5341857

Daniel Araújo de Azevedo

Phenomenological Study of Neutrino Invisible Decay on MINOS and MINOS+ Experiments

Estudo Fenomenológico de Decaimento Invisível de Neutrinos nos Experimentos MINOS e MINOS+

Dissertation presented at the Programa de Pós-Graduação em Física (PPGF), at the Instituto de Física (IF) at the Universidade Federal de Goiás (UFG), as a requisite for obtaining the title of Master of Science in Physics.

Field of study: Physics.

Line of research: High Energy Physics.

Advisor: Professor PhD Ricardo Avelino Gomes

GOIÂNIA

2025

Ficha de identificação da obra elaborada pelo autor, através do
Programa de Geração Automática do Sistema de Bibliotecas da UFG.

Azevedo, Daniel Araújo de
Phenomenological Study of Neutrino Invisible Decay on MINOS and MINOS+ Experiments [manuscrito] / Daniel Araújo de Azevedo. - 2025.
xxi, 131 f.: il.

Orientador: Prof. Dr. Ricardo Avelino Gomes.
Dissertação (Mestrado) - Universidade Federal de Goiás, Instituto de Física (IF), Programa de Pós-Graduação em Física, Goiânia, 2025.
Bibliografia. Anexos. Apêndice.
Inclui siglas, abreviaturas, símbolos, gráfico, tabelas, lista de figuras, lista de tabelas.

1. Decaimento invisível. 2. Efeito de matéria. 3. MINOS. 4. MINOS+. 5. Oscilação de neutrinos. I. Gomes, Ricardo Avelino, orient. II. Título.

CDU 539.12

UNIVERSIDADE FEDERAL DE GOIÁS

INSTITUTO DE FÍSICA

ATA DE DEFESA DE DISSERTAÇÃO

Ata nº 225 da sessão de Defesa de Dissertação de Daniel Araújo de Azevedo, que confere o título de Mestre em Física, na área de concentração em Física.

Aos 03 dias do mês de abril de 2025, a partir das 14h00min, por meio de videoconferência, realizou-se a sessão pública de Defesa de Dissertação intitulada “Phenomenological study of neutrino invisible decay on MINOS and MINOS+ experiments”. Os trabalhos foram instalados pelo Orientador, Professor Doutor Ricardo Avelino Gomes (IF/UFG), com a participação dos demais membros da Banca Examinadora: Professor Doutor Ademar Paulo Júnior (IFTO), membro titular externo; e Professor Doutor Guilherme Colherinhas de Oliveira (IF/UFG), membro titular interno. Durante a arguição, os membros da banca não fizeram sugestão de alteração do título do trabalho. A Banca Examinadora reuniu-se em sessão secreta a fim de concluir o julgamento da Dissertação, tendo sido o candidato aprovado pelos seus membros. Proclamados os resultados pelo Professor Doutor Ricardo Avelino Gomes, Presidente da Banca Examinadora, foram encerrados os trabalhos e, para constar, lavrou-se a presente ata que é assinada pelos membros da Banca Examinadora, aos 03 dias do mês de abril de 2025.

TÍTULO SUGERIDO PELA BANCA

Documento assinado eletronicamente por **Ricardo Avelino Gomes**, **Professor do Magistério Superior**, em 03/04/2025, às 16:47, conforme horário oficial de Brasília, com fundamento no § 3º do art. 4º do Decreto nº 10.543, de 13 de novembro de 2020 .

Documento assinado eletronicamente por **Guilherme Colherinhas De Oliveira**, **Professor do Magistério Superior**, em 03/04/2025, às 16:47, conforme horário oficial de Brasília, com fundamento no § 3º do art. 4º do Decreto nº 10.543, de 13 de novembro de 2020 .

Documento assinado eletronicamente por **Ademar Paulo Júnior**, **Usuário Externo**, em 03/04/2025, às 16:49, conforme horário oficial de Brasília, com fundamento no § 3º do art. 4º do Decreto nº 10.543, de 13 de novembro de 2020.

A autenticidade deste documento pode ser conferida no site https://sei.ufg.br/sei/controlador_externo.php?acao=documento_conferir&id_orgao_acesso_externo=0, informando o código verificador **5269746** e o código CRC **A15308AB**.

Referência: Processo nº 23070.017231/2025-91 SEI nº 5269746

" *Fantasy is hardly an escape from reality. It's a way of understanding it.*"

Lloyd Alexander

Acknowledgements

I would like to thank my parents, Professor PhD Neucírio Ricardo de Azevedo and MSc Rosilda Araújo de Oliveira Azevedo, for giving me all the support, help and encouragement not with just this work, but with all the other things that life has already showed me. I thank my sister Professor PhD Lorena Araújo de Oliveira Borges for being more than a reference for achieving my objectives, but also for being one of my biggest friends. I also thank my brother Edgar Borges Júnior for all the conversations that went from the beauty of mathematics to the ones in language.

I want to thank my advisor, Professor PhD Ricardo Avelino Gomes, for presenting me with such a hot topic as neutrino physics. But even more than that, for all the knowledge, interesting conversations that lead to profound meditations and for also helping me to awaken a scientific mind and curiosity and for all the help he provided me throughout this journey.

All of the members and associates of the High Energy Physics Laboratory, Alessandro Rosa, Davi Assis, Isabella Rocha and Pedro Eloi, I thank all of you for the support and help you have provided me in times of need and for making physics more understandable from the perspective of a chemist. Also I thank PhD Abner Leonel Gomes, PhD Luiz Prais, and PhD Michelle Medeiros, for their thesis and dissertations were used as a reference material for this one.

I thank the NOνA collaboration, for allowing me to have an amazing experience as part of such a large collaboration, even in a small way.

The members of the LEEDMOL laboratory, Professor PhD Heibbe C. B. Oliveira, PhD Ana Gabriela, MSc Mateus Barbosa, MSc Pedro Henrique, MSc Ana Carolina, Rafael Verrísimo, for all the hospitality, laughts, conversations and help with being a graduate student, I thank you all.

I did not have a coffee machine by my side for support, but I had a much better therapist, LMHC Renan Rozzetto, who helped me make the best out of the worst situations I

encountered during these years of study. For this, I thank you.

I also want to thank a personal friend, Iago M. B. de Sá Vaz da Silva, for helping me with the computational part of this work. Without his help with optimizations, the code would have taken days to finish running instead of seconds. And also all of my friends that stood by my side in moments of great need: Bruno Kanzler, Carlos Scherer, Felipe Aguiar, Gabriel Ceneviva, Guilherme Martins, João Vitor Marinho, Marcelo Custódio, Morgana F. Hoefel, Miguel Dantas, Nicolas Ardanuy, Nicolas Grinet, Pedro Luiz T. C. de Oliveira, Pedro Victor M. Amaral, Rafael Carvalho, and many others that I might have forgotten the name, but do deserve a place here.

I am grateful beyond words with the *Brazilian National Council for Scientific and Technological Development* (CNPq, *Conselho Nacional de Desenvolvimento Científico e Tecnológico*) for the funding of this work. Without this help, I do not think this work could have been done.

Finally, I thank one dear friend of mine, that is not among us. However, in every starry night sky, has made his presence in my life.

Abstract

The neutrino oscillation model is already well stablished; however, there is still interest in investigating phenomena that may occur alongside it. One of them being decay, already ruled out as happening alone, but can still occur with oscillation. Some of the recent analysis in the literature try to, using experimental data from accelerator experiments, have a measurement of the parameter τ_3/m_3, carrying information about the decay of the mass eigenstate ν_3. The following work consider the data from the MINOS and MINOS+ long-baseline experiments, for different models of neutrino oscillation: the standard oscillation and the oscillation with decay in vacuum and in matter. From the $P_{\nu_\mu \to \nu_\mu}$ probability, and considering the charged current events of ν_μ, we want to show: how the presence of the MINOS+ data affects the results obtained with the MINOS experiment; we also implement the oscillation with decay in matter model, which is a more suited one as a proof of concept, considering that modern studies do consider the matter effects; a value for the τ_3/m_3 parameter. This analysis also yields a best fit value for the oscillation with decay in matter of the combined experimental data, having $\Delta m^2_{32} = 2.226 \times 10^{-3}\ eV^2$, $\sin^2\theta_{23} = 0.715$ and a lower bound limit of 90% C.L. for the decay parameter of $\tau_3/m_3 > 1.52 \times 10^{-12}\ s/eV$.

Keywords: Invisible Decay, Matter Effects, MINOS, MINOS+, Neutrino, Neutrino Oscillation, Oscillation with Decay.

Resumo

O modelo de oscilação de neutrinos já está bem estabelecido, no entanto, há o interesse na investigação de fenômenos que ocorram de forma paralela a este. Um desses sendo o decaimento, fenômeno que isoladamente já foi descartado, mas que pode ocorrer de forma não dominante junto à oscilação. Algumas das análises mais recentes da literatura visam, através de medidas experimentais de dados de acelerador, mensurar o valor de τ_3/m_3, o parâmetro que carrega informações a cerca do decaimento do auto-estado de massa ν_3. O presente trabalho visa analisar os dados dos experimentos MINOS e MINOS+, experimentos de long-baseline, para diferentes modelos de oscilação de neutrinos: oscilação padrão e oscilação com decaimento no vácuo e na matéria. A partir da probabilidade $P_{\nu_\mu \to \nu_\mu}$, considerando os eventos de corrente carregada ν_μ, desejamos mostrar como que a presença dos dados do MINOS+ afetam os resultados obtidos com o experimento MINOS; a implementação do modelo de oscilação com decaimento na matéria, que é mais adequado e servirá como uma prova de conceito, considerando que estudos modernos já consideram o efeito de materia; e um valor para o parâmetro τ_3/m_3. Essa análise também resulta em um valor de best fit para a oscilação com decaimento e efeito de materia considerando ambos os experimentos, obtendo: $\Delta m^2_{32} = 2.226 \times 10^{-3}\ eV^2$, $\sin^2\theta_{23} = 0.715$ e um limite inferior com 90% de C.L. para o parâmetro de decaimento $\tau_3/m_3 > 1.52 \times 10^{-12}\ s/eV$.

Palavras-Chave: Decaimento Invisível, Efeito de Matéria, MINOS, MINOS+, Neutrino, Oscilação de Neutrinos, Oscilação com Decaimento.

Contents

List of Figures

List of Tables

List of Abbreviations

ACNET	**A**ccelerator **C**ontrol **NET**work
ADC	**A**nalog to **D**igital **C**onverter
AGS	**A**lternating **G**radient **S**ynchroton
BRP	**B**ranch **R**eadout **P**rocessor
CC	**C**harged **C**urrent
CL	**C**onfidence **L**evel
DAQ	**D**ata **AQ**uisition system
DCP	**D**ata **C**ollection **P**rocess
DDS	**D**ata **D**istribution **S**ystem
DONuT	**D**irect **O**bservatory of the **N**u **T**au
ESSnuSB	**E**uropean **S**pallation **S**ource **nu** (Neutrino) **S**uper **B**eam
ETC	**E**vent **T**ime **C**ontroller
FADC	**F**lash **A**nalog to **D**igital **C**onverter
FD	**F**ar **D**etector
FHC	**F**orward **H**orn **C**urrent
FIFO	**F**irst **I**n **F**irst **O**ut
GPS	**G**lobal **P**ositioning **S**ystem
LBL	**L**ong-**B**ase**L**ine
MASTER	**M**INOS **A**quisition **S**parsifier and **T**ime stamper for **E**vent **R**eadout
MENU	**M**INOS **E**lectronics for **NU**(neutrinos)
MINDER	**MI**NOS **N**ear **D**etector **E**lectronic **R**eadout
MINERνA	**M**ain **I**njector **N**eutrino **E**xpe**R**iment to study ν-**A** interactions
MiniBooNE	**Mini Boo**ster **N**eutrino **E**xperiment

MINOS	**M**ain **I**njector **N**eutrino **O**scillation **S**earch
MSW	**M**ikheyev **S**mirnov **W**olfestein
NC	**N**eutral **C**urrent
ND	**N**ear **D**etector
NOνA	**N**uMI **O**ff-axis ν_e **A**pperance
NuMI	ν (neutrinos) at the **M**ain **I**njector
PE	**P**hoton-**E**lectron
PMNS	**P**ontecorvo-**M**aki-**N**akagawa-**S**akata
PMT	**P**hoto **M**ultiplier **T**ube
POT	**P**rotons **O**n **T**arget
PVIC	**P**CI **V**ertical **I**nter**C**onnection
QIE	**Q**(charge) **I**ntegration **E**ncoder
RHC	**R**everse **H**orn **C**urrent
ROP	**R**ead**O**ut **P**rocessor
SK	**S**uper-**K**amiokande
SM	**S**tandard **M**odel
SNO	**S**udbury **N**eutrino **O**bservatory
SNU	**S**olar **N**eutrino **U**nit
T2K	**T**okai **2** (To) **K**amioka
TP	**T**rigger **P**rocessor
VA	Viking **VA** chip
VARC	**VA** **R**eadout **C**ard
VFB	**V**A **F**ront **B**oard
VME	**V**ersa **M**odule **E**uropa
VMM	**V**A **M**ezzanine **M**odule
WLS	**W**ave**L**ength-**S**hifting Fiber

Chapter 1

Introduction

Neutrinos are fundamental particles, a family of fermions described by the Standard Model (SM) of particle physics. These particles are the most abundant in nature, however, are also the ones we do not know as much. They are known to go through a phenomenon called flavor oscillation, first proposed in 1967, and that was used to solve the solar neutrino problem.

This first model became well established and goes beyond what the SM describes for neutrinos. The oscillation probability that arises from this model does add new physical parameters to be investigated: the mixing angles and the different quadratic masses.

Besides this model, other ones were proposed like the neutrino decay in 1998 to answer another open problem about the zenith angle. This model, however, has been rejected as a major phenomenon [1]. The presence of decay suggests that the eigenstates of the mass basis ν_1, ν_2 and ν_3 could all decay and a new parameter τ_i/m_i, for $i = 1,2,3$, is needed to confirm this hypothesis.

The first two eigenstates ν_1 and ν_2 have lifetimes already well restricted from the data obtained from the SN1987A supernova [2]. The combined data from the KamLAND reactor and the solar data shows that these physical parameters are in the order of $\tau_1/m_1 > 4 \times 10^{-3}\ s/eV$ and $\tau_2/m_2 > 7 \times 10^{-4}\ s/eV$ [3]. Meanwhile, the heavier state ν_3 has its best lower bound in $\tau_3/m_3 > 2.9 \times 10^{-10}\ s/eV$, being the one that is not as stricted as the others and, as such, the one with the biggest interest in investigating.

Many studies try to improve the lower bound, others predict how sensitive a experiment is, or will be, for studying the decay. Some studies on the lower bound of the parameter

can be found in the upper half of Table 1.1, using a phenomenological approach, while the sensitivity studies can be seen in the lower half of the table.

Table 1.1: In the upper half, values for the lower limit of the τ_3/m_3 parameter obtained with a phenomenological analysis with the data sets of the experiments: NOνA, T2K and NOνA + T2K [4]; MINOS (CC & NC) [5]; MINOS, T2K & MINOS + T2K [1] and MINOS (CC & NC), SK and K2K [6]. And, in the lower half, sensitivity for the limit of the τ_3/m_3 parameter for the experiments: KM3NeT/ORCA [7]; INO-ICAL [8]; JUNO [9]; DUNE [10]; ESSnuSB [11] and MOMENT [12].

	τ_3/m_3 (s/eV) 90%CL	Data Set	Data Type	Year of Pub.
Phenomenology	$\geq 1.5 \times 10^{-12}$	NOνA T2K NOνA + T2K	LBL	2018
	$\geq 2.1 \times 10^{-12}$	MINOS (CC & NC)	LBL	2010
	$\geq 2.8 \times 10^{-12}$	MINOS(ν_μ CC) MINOS($\bar{\nu}_\mu$ CC) MINOS (NC) MINOS + T2K	LBL	2015
	$\geq 2.9 \times 10^{-10}$	MINOS (CC & NC) SK K2K	LBL; Atmospheric Neutrino	2008
Sensitivity	$\geq 1.78 \times 10^{-10}$	KM3NeT/ORCA	Atmospheric Neutrino	2023
	$\geq 1.51 \times 10^{-10}$	INO-ICAL	Atmospheric Neutrino	2018
	$\geq 9.3 \times 10^{-11}$ (99% CL)	JUNO	Medium-Baseline	2015
	$\geq 5.1 \times 10^{-11}$	DUNE	LBL	2020
	$\geq 4.22 \times 10^{-11}$	ESSnuSB	LBL	2020
	$\geq 2.8 \times 10^{-11}$	MOMENT	Medium-Baseline	2019

However, all these experiments consider that the neutrino oscillation and decay happens in vacuum, recent studies, such as the one made by *Gröonros et al.* [3], tries to consider a more realistic scenario considering the matter effects that arrise when neutrinos are travelling

through a medium, such as the Earth, proposing numerical and analitycal approaches. In the case cited, an analitycal treatment using series expansions.

In this work, we propose to investigate how the limits obtained for the Main Injector Neutrino Oscillation Search (MINOS) experiment data are affected by adding a new data set, the one from the MINOS+ experiment. We consider all the three models proposed, standard oscillation, oscillation with decay in vacuum and oscillation with decay in matter. We also aim to obtain a best fit value and a lower bound for the τ_3/m_3 parameter.

In the second chapter, we provide a brief introduction to the history of neutrinos and the mathematical formalism for calculating the oscillation probabilities in different models. In the third chapter, we present the MINOS and MINOS+ experiments, the production of the neutrino beams, the detectors and the data selection. In the fourth chapter we will present a methodology of how we treated the data and the use of the χ^2 function to verifiy the agreement of our model with the real data. Finally, in the fifth chapter, we present the effects of the MINOS+ experiment on the MINOS data and a best fit value for the τ_3/m_3 parameter considering oscillation with decay in matter.

Chapter 2

Neutrino Physics

2.1 A brief history about neutrinos

2.1.1 The conjecture

The beta decay is a spontaneous process that happens in some radioactive nuclei such as:

$$n \rightarrow p + e^{-} + \bar{\nu}_e, \tag{2.1}$$

in which a neutron (n) decays into a proton (p) an electron (e^{-}) and an electron antineutrino ($\bar{\nu}_e$).

In the early 20th century, given that the neutrino/antineutrino were not even proposed, it was thought that the beta decay was a two body problem. This would imply that the emitted electron would have a fixed value for its energy. However, in 1914, J. Chadwick concluded that the energy of the emitted electron was not constant, but rather followed a continuous distribution [13].

W. Pauli, in 1930, proposed the ideia of a new particle called “neutron”, that has a spin of 1/2, and obeys the exclusion principle, having a mass in the same order of magnitude of the electron, not larger than 0.01 times the mass of a proton [14].

However, in 1932, J. Chadwick discovered a neutral particle with a similar mass, spin and other properties of the proton, the “neutron” [15]. The proposed particle given by Pauli was renamed by Enrico Fermi to “neutrino”, which could be though as a “lighter neutron”.

2.1.2 The detection

Frederick Reines and Clyde Cowan would detect the neutrino twenty six years after Pauli's proposition [16, 17]. The detection of the first neutrino, which was an electron antineutrino, was made with the inverse beta decay reaction with the production of a positron (e^+) on a nuclear reactor at the Savannah River Reactor:

$$\bar{\nu}_e + p \rightarrow e^+ + n. \tag{2.2}$$

The detection was made through the use of a liquid scintillator detector. Once the positron was emitted, it would annihilate upon interacting with electrons near the detector, emitting a pair of photons. After that, the neutron would be capture by cadmium (Cd) atoms, which when de-excited would release another pulse with a time delay from the first. This experiment would be an indirect confirmation of the neutrino. A schematic of the experiment can be seen on Figure 2.1 [18, 19].

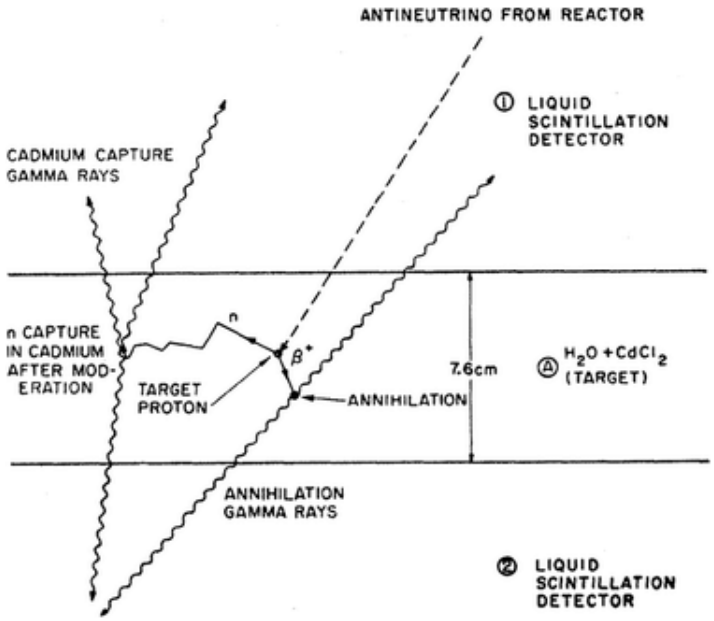

Figure 2.1: Savannah neutrino detection experiment schematic. An antineutrino can be seen being emitted from the reactor, interacting with a proton, leading to the production of the positron and neutron, which would lead to two delayed pulses [20].

2.2 Neutrino flavors

In 1962, *L. Lederman et al.* [21]. used an Alternating Gradiend Synchroton (AGS) to make a beam of charged pions that would decay as:

$$\pi^+ \to \mu^+ + \nu_\mu, \tag{2.3}$$

if there was only one kind of neutrino, the following equations would be detected at the same rate:

$$\nu_e + n \to p + e^-, \tag{2.4}$$

$$\nu_\mu + n \to p + \mu^-, \tag{2.5}$$

however, in place of the electron events, 29 muon events were detected. Which implies that there are at least two flavors of neutrinos, the ν_e and ν_μ [21].

Later, in 1975, *Perl et al.* [22]. reported that anomalous events had occured while conducting an experiment of the colission of electrons with positrons. A pair of $e^-\mu^+$ could be detected, but at least two new particles were required to explain a lack in the energy and momentum spectra. This research lead to the discovery of the tau (τ) particle. The decay of a negatively and positively charged tau would lead to the production of the detected particles, as described by Ref. [22]:

$$\begin{aligned} e^+ + e^- &\to \tau^+ + \tau^- \\ \tau^- &\to e^- + \bar{\nu}_e + \nu_\tau \\ \tau^+ &\to \mu^+ + \nu_\mu + \bar{\nu}_\tau. \end{aligned} \tag{2.6}$$

The discovery of the tau particle closed the third generation of leptons, and started the search for the tau neutrino, which was not detected and confirmed until the year 2000 by the DONuT collaboration [23]. With this confirmation, for all leptons there would be an assigned neutrino

with the respective flavor.

2.3 The solar neutrino problem

One of the greatest sources of neutrinos is the sun. By the proton-proton fusion chain the flux of electron neutrinos that reaches the Earth is of about 6×10^{10} per cm^2/s [24, 25]. In the late 1960s, the Homestake experiment would begin to measure this flux of solar neutrinos, by using a radiochamical technique based on the reverse beta reaction:

$$\nu_e + {}^{37}Cl \rightarrow {}^{37}Ar + e^-. \tag{2.7}$$

The detection of argon implies that a neutrino must have interacted. However, the experiment came to the conclusion that the observed neutrino flux was below 3 Solar Neutrino Units (SNU)[1], lower than the expected value of 9 SNU [26].

Other experiments, such as Kamiokande-II, a Cherenkov detector experiment, would also report [27] that the flux of neutrinos measured were 0.5 times the predicted value given in [24]. This means three different possibilities: the former being that there was discrepancies with the experiments, secondly that the calculations for the predicted flux had an error, lastly that some new physics was about to be discovered!

The Sudbury Neutrino Observatory (SNO) experiment gave an answer to the solar neutrino problem. The SNO measures neutral current (NC) events, making it also sensitive for ν_μ and ν_τ [28], two flavors of neutrinos that are not produced in the sun. Given that the proton-proton chain (the major process of nuclear fusion on the Sun) follows the equation:

$$4p \rightarrow {}^4He + 2e^+ + 2\nu_e + Q, \tag{2.8}$$

[1] 1 SNU is defined as one interaction per 10^{-36} of the atoms of the detector per second.

where $Q = 26.73\ MeV$ and the secondary processes that happen in the Sun also produces ν_e [29].

Nonetheless, the experiment would come to the conclusion that the total predicted flux was consistent if the other flavors of neutrino were taken into consideration [30]. This would mean that neutrinos were oscillating from one flavor to another, a phenomenon that is now known as neutrino oscillations.

2.4 Neutrino oscillations formalism

This phenomenon of oscillations was, nonetheless, not a new one. The neutral kaon-antikaon oscillations were already observed and were the inspiration for Pontecorvo to suggest the same mechanism for the neutrino-antineutrino oscillation in 1957 [31]. Later, the ideia of neutrino mixing was given by Maki, Nakagawa and Sakata [32] and the flavor oscillation was proposed by Pontecorvo in 1967 [33, 34].

Given that neutrinos oscillate, this implies that the mass eigenstate basis and flavor eigenstate basis are not the same. Therefore, we can express a relation between the flavor and the mass eigenstates with a unitary transformation matrix as follows [33, 34]:

$$\begin{pmatrix} \nu_e \\ \nu_\mu \\ \nu_\tau \end{pmatrix} = \begin{pmatrix} U_{e1} & U_{e2} & U_{e3} \\ U_{\mu 1} & U_{\mu 2} & U_{\mu 3} \\ U_{\tau 1} & U_{\tau 2} & U_{\tau 3} \end{pmatrix} \begin{pmatrix} \nu_1 \\ \nu_2 \\ \nu_3 \end{pmatrix}. \tag{2.9}$$

We can use the sum notation to arrive at:

$$|\nu_\alpha\rangle = \sum_k U^*_{\alpha k} |\nu_k\rangle\,, \tag{2.10}$$

where we have $\alpha = e, \mu, \tau$, which are the flavors, and $k = 1, 2, 3$, that are related to the mass states. And the $U^*_{\alpha k}$ represents a term in the 3x3 PMNS (Pontecorvo-Maki-Nakagawa-Sakata) matrix.

The PMNS matrix is a 3x3 unitary matrix that arises from a rotation in the complex plane. This way, we can write it as a parametrized Euler rotation matrix with phase shifts as follows (considering 3 mixing angles and 6 phases) [35]:

$$U = D^L \cdot R_{23} \cdot D^1(\eta_{13}) \cdot R_{13} \cdot D^{1\dagger}(\eta_{13}) \cdot R_{12} \cdot D^R, \tag{2.11}$$

the R_{ij} matrices are the Euler rotation ones, the D matrices represent a shift in the phases, and η_{13} is the phase that will give rise for the charge-parity violation parameter (δ_{CP}). We can define $W^{13} = D^1(\eta_{13}) \cdot R_{13} \cdot D^{1\dagger}(\eta_{13})$ and arrive in a more compact form:

$$U = D^L \cdot R_{23} \cdot W^{13} \cdot R_{12} \cdot D^R. \tag{2.12}$$

If we now open the left and right D matrices, we can factorize five phases as such:

$$D^L = \begin{pmatrix} e^{i\omega_1} & 0 & 0 \\ 0 & e^{i(\omega_2-\eta_{12})} & 0 \\ 0 & 0 & e^{i(\omega_3-\eta_{12}-\eta_{23})} \end{pmatrix}, \tag{2.13}$$

$$D^R = \begin{pmatrix} 1 & 0 & 0 \\ 0 & e^{i\eta_{12}} & 0 \\ 0 & 0 & e^{i(\eta_{12}+\eta_{23})} \end{pmatrix}, \tag{2.14}$$

the following phases: ω_1, $\omega_2 - \eta_{12}$ and $\omega_3 - \eta_{12} - \eta_{23}$ can be absorbed by the lepton fields with the following redefinition:

$$\ell_{\alpha L} \to e^{i\psi_\alpha} \ell_{\alpha L}, \tag{2.15}$$

with $\psi_e = \omega_1$, $\psi_\mu = \omega_2 - \eta_{12}$ and $\psi_\tau = \omega_3 - \eta_{12} - \eta_{23}$ [35].

If neutrinos are Dirac particles, we can absorve the other two phases remaining η_{12} and $\eta_{12}+\eta_{23}$. Which can be achieved by changing the neutrino fields such as [33]:

$$\nu_i(x) \rightarrow e^{i\phi_i}\nu_i(x), \tag{2.16}$$

with $\phi_1 = \eta_{12}$ and $\phi_2 = \eta_{12}+\eta_{23}$.

With this, we have reduced the 6 phases that comes with the 3x3 unitary matrix to only one (the δ_{CP} phase). For us to understand the meaning of this phase, we need to consider symmetries and their conservation. If a system conserves a symmetry, it means that the whole system is invariant to its application. We have three symmetries to consider: charge (C), parity (P) and time reversal (T).

The charge symmetry changes the particle quantum numbers and electrical charge, an example would be turning a negative particle into a positive one. The parity symmetry changes the spacial coordinates, that could be seen a particle propagating in the x axis and, after the application of the operator, would propagate to $-x$. For the time reveral symmetry, we can think of a particle propagating in time t and, after the transformation, propagating in a time $-t$ [36]. This is a resumed view of this topic, for a more in depth explanation Ref. [37] is recommended.

Given that neutrinos do not remain invariant for charge and parity symmetries, we say that they violate the CP symmetry. And this effect can be seen and measured by the δ_{CP} parameter.

We can now consider $D^R = P$ and write a general PMNS matrix (Dirac & Majorana) in terms of its mixing angles and the phases as follows [35]:

$$U = R_{23} \cdot W^{13} \cdot R_{12} \cdot P, \tag{2.17}$$

$$U = \begin{pmatrix} 1 & 0 & 0 \\ 0 & c_{23} & s_{23} \\ 0 & -s_{23} & c_{23} \end{pmatrix} \begin{pmatrix} c_{13} & 0 & s_{13}e^{-i\delta_{CP}} \\ 0 & 1 & 0 \\ -s_{13}e^{i\delta_{CP}} & 0 & c_{13} \end{pmatrix} \begin{pmatrix} c_{12} & s_{12} & 0 \\ -s_{12} & c_{12} & 0 \\ 0 & 0 & 1 \end{pmatrix} P, \tag{2.18}$$

$$U = \begin{pmatrix} c_{12}c_{13} & s_{12}c_{13} & s_{13}e^{-i\delta_{CP}} \\ -s_{12}c_{23} - c_{12}s_{23}s_{13}e^{i\delta_{CP}} & c_{12}c_{23} - s_{12}s_{23}s_{13}e^{i\delta_{CP}} & s_{23}c_{13} \\ s_{12}s_{23} - c_{12}c_{23}s_{13}e^{i\delta_{CP}} & -c_{12}s_{23} - s_{12}c_{23}s_{13}e^{i\delta_{CP}} & c_{23}c_{13} \end{pmatrix} P, \tag{2.19}$$

where $c_{ij} = \cos\left(\theta_{ij}\right)$, $s_{ij} = \sin\left(\theta_{ij}\right)$ and the δ_{CP} is the phase which allows for the Charge-Parity (CP) violation.

As commented prior, if neutrinos are Dirac particles, the two extra phases can be absorbed by the neutrino fields, which will make the P matrix to be the identity. But, if the neutrinos are Majorana particles, we need to consider this extra matrix, however, it does not interfere with the oscillations and, as such, will be ignored [33].

Given Eq. (2.10) and the PMNS matrix, we can derive the probability of a transition $\nu_\alpha \to \nu_\beta$.

2.5 Three flavor standard oscillation

The following deduction will assume the plane wave approach for the neutrino oscillation. That is to say we are using a simple model and approximations that are not cohesive with all of the conditions of the system, but that will arrive at the correct probability.

For an arbitrary neutrino ν_α, if we sigh to understand the probability of it oscillating to another flavor, we need to first find its energy in the mass basis and, afterwards, apply the

time evolution operator. The Hamiltonian in the mass basis, can be written as:

$$\mathscr{H} = \begin{pmatrix} E_1 & \cdots & 0 \\ \vdots & \ddots & \vdots \\ 0 & \cdots & E_i \end{pmatrix}, \tag{2.20}$$

where E_i is the energy eigenvalue of the ν_i neutrino. Applying the time operator, we arrive at:

$$|\nu_k(t)\rangle = \exp(-iE_k t)\,|\nu_k\rangle\,. \tag{2.21}$$

It is important to say that Eq. (2.21) is in natural units, as well as all the others to come, therefore $\hbar = c = 1$. Since we have now an expression for the time evolution of the mass state, we can use it on Eq. (2.10) to arrive on how the flavor basis evolves [19]:

$$|\nu_\alpha(t)\rangle = \sum_k U^*_{\alpha k} \exp(-iE_k t)\,|\nu_k\rangle\,. \tag{2.22}$$

Eq. (2.22) give us the time evolution of an arbitraty neutrino flavor, now we need its amplitude with another flavor ν_β:

$$\langle \nu_\beta | \nu_\alpha(t)\rangle = \left(\sum_j U_{bj} \langle \nu_j|\right)\left(\sum_k U^*_{\alpha k} \exp(-iE_k t)\,|\nu_k\rangle\right), \tag{2.23a}$$

$$= \sum_j \sum_k U_{\beta j} U^*_{\alpha k} \exp(-iE_k t)\,\langle \nu_j|\nu_k\rangle\,, \tag{2.23b}$$

the $\langle \nu_j|\nu_k\rangle$ will give us a Kronecker delta, hence only if $j = k$ we will have non-zero terms:

$$\langle \nu_\beta | \nu_\alpha(t)\rangle = \sum_k U_{\beta k} U^*_{\alpha k} \exp(-iE_k t)\,. \tag{2.24}$$

Taking the modulus square, we obtain the probability:

$$P_{\nu_\alpha \to \nu_\beta} = \left\langle \nu_\beta \middle| \nu_\alpha(t) \right\rangle^* \left\langle \nu_\beta \middle| \nu_\alpha(t) \right\rangle, \tag{2.25a}$$

$$= \left(\sum_j U^*_{\beta j} U_{\alpha j} \exp\left(iE_j t\right) \right) \left(\sum_k U_{\beta k} U^*_{\alpha k} \exp(-iE_k t) \right), \tag{2.25b}$$

$$= \sum_j \sum_k U^*_{\beta j} U_{\alpha j} U_{\beta k} U^*_{\alpha k} \exp\left[-i\left(E_k - E_j\right)t\right]. \tag{2.25c}$$

The new sum obtained can be broken in three different parts, one if $k = j$, and the other ones being for $k > j$ and $j > k$.

$$\begin{aligned} P_{\nu_\alpha \to \nu_\beta} = \sum_k |U_{\alpha k} U_{\beta k}|^2 &+ \sum_{k>j} U^*_{\beta j} U_{\alpha j} U_{\beta k} U^*_{\alpha k} \exp\left[-i\left(E_k - E_j\right)t\right] \\ &+ \sum_{j>k} U^*_{\beta j} U_{\alpha j} U_{\beta k} U^*_{\alpha k} \exp\left[-i\left(E_k - E_j\right)t\right], \end{aligned} \tag{2.26}$$

now we can alter the index of the third sum (given that they are dummy variables) such that it becomes $k > j$, given that we correct the argument of the sum:

$$\begin{aligned} P_{\nu_\alpha \to \nu_\beta} = \sum_k |U_{\alpha k} U_{\beta k}|^2 &+ \sum_{k>j} U^*_{\beta j} U_{\alpha j} U_{\beta k} U^*_{\alpha k} \exp\left[-i\left(E_k - E_j\right)t\right] \\ &+ \sum_{k>j} U^*_{\beta k} U_{\alpha k} U_{\beta j} U^*_{\alpha j} \exp\left[-i\left(E_j - E_k\right)t\right], \end{aligned} \tag{2.27}$$

now rearranging the terms of the third sum:

$$\begin{aligned} P_{\nu_\alpha \to \nu_\beta} = \sum_k |U_{\alpha k} U_{\beta k}|^2 &+ \sum_{k>j} U^*_{\beta j} U_{\alpha j} U_{\beta k} U^*_{\alpha k} \exp\left[-i\left(E_k - E_j\right)t\right] \\ &+ \sum_{k>j} U_{\beta j} U^*_{\alpha j} U^*_{\beta k} U_{\alpha k} \exp\left[i\left(E_k - E_j\right)t\right], \end{aligned} \tag{2.28}$$

we can see that the third sum is nothing more than the complex conjugate of the second. Given this, we can use the following property $z+z^* = 2\mathscr{R}(z)$, we then arrive at:

$$P_{\nu_\alpha \to \nu_\beta} = \sum_k |U_{\alpha k} U_{\beta k}|^2 + 2 \sum_{k>j} \mathscr{R}\left(U^*_{\beta j} U_{\alpha j} U_{\beta k} U^*_{\alpha k} \exp\left[-i\left(E_k - E_j\right)t\right]\right). \tag{2.29}$$

Rearranging the energy, since neutrinos are relativistic particles, we can write it as:

$$E_i = \sqrt{p_i^2 + m_i^2}, \tag{2.30}$$

which leads to:

$$E_i = p_i \sqrt{1 + \left(\frac{m_i^2}{p_i^2}\right)}, \tag{2.31}$$

applying the Taylor expansion[2] (at $x = 0$) for $\sqrt{1+x^2} = 1 + x^2/2 + \mathscr{O}(x^3)$, to the second term and defining $x = m_i/p_i$, we have:

$$E_i \approx p_i \left(1 + \frac{m_i^2}{2p_i^2}\right), \tag{2.32}$$

given that neutrinos have really small rest masses, most of the energy is derived from its kinetic energy, hence we can say $p_i \approx E$:

$$E_i \approx E + \frac{m_i^2}{2E}, \tag{2.33}$$

with E being the neutrino total energy. This approximation is not rigorous, but leads to an excellent approximation [39]. It will lead to some implications on neutrino behaviour (such as all the different neutrinos momentum being approximately equal) or even contradictions that go beyond the scope of this work. For a better clarification, it is recommended Ref. [40].

[2]The mass of a neutrino is in the order of magnitude of eV [38], while their momentum is in GeV, given that most of the energy is kinetic. Therefore, we can see that $\frac{m_i}{p_i} \ll 1$, allowing for the use of this approximation.

We can now consider the difference in the energy of two different neutrinos as:

$$\left(E+\frac{m_k^2}{2E}\right)-\left(E+\frac{m_j^2}{2E}\right)=\frac{m_k^2-m_j^2}{2E}, \tag{2.34}$$

defining $\Delta m_{kj}^2 = m_k^2 - m_j^2$ we get:

$$E_k - E_j = \frac{\Delta m_{kj}^2}{2E}, \tag{2.35}$$

with Eq. (2.35) we can rewrite Eq. (2.29) as:

$$P_{\nu_\alpha\to\nu_\beta} = \sum_k |U_{\alpha k}U_{\beta k}|^2 + 2\sum_{k>j}\mathscr{R}\left(U_{\beta j}^* U_{\alpha j} U_{\beta k} U_{\alpha k}^* \exp\left[-i\left(\frac{\Delta m_{kj}^2}{2E}\right)t\right]\right). \tag{2.36}$$

The next step is to rewrite the time in terms of the distance, since $t = L/c$, but in the natural units system we have that $c = 1$, therefore $t \approx L$:

$$P_{\nu_\alpha\to\nu_\beta} = \sum_k |U_{\alpha k}U_{\beta k}|^2 + 2\sum_{k>j}\mathscr{R}\left(U_{\beta j}^* U_{\alpha j} U_{\beta k} U_{\alpha k}^* \exp\left[-i\left(\frac{\Delta m_{kj}^2 L}{2E}\right)\right]\right). \tag{2.37}$$

Applying another relation of complex numbers to Eq. (2.37):

$$\mathscr{R}(z_1 z_2) = \mathscr{R}(z_1)\mathscr{R}(z_2) - \mathscr{I}(z_1)\mathscr{I}(z_2), \tag{2.38}$$

allowing for the substitution[3]:

$$z_1 = U_{\beta j}^* U_{\alpha j} U_{\beta k} U_{\alpha k}^*, \tag{2.39a}$$

$$z_2 = \cos\left(\frac{\Delta m_{kj}^2 L}{2E}\right) - i\sin\left(\frac{\Delta m_{kj}^2 L}{2E}\right), \tag{2.39b}$$

[3]The z_2 term chosen is actually $z_2 = \exp\left[-i\left(\frac{\Delta m_{kj}^2 L}{2E}\right)\right]$, we can then use the Euler relation: $e^{\pm ix} = \cos(x) \pm i\sin(x)$, allowing us to write it as Eq. (2.39b).

$$P_{\nu_\alpha \to \nu_\beta} = \sum_k |U_{\alpha k} U_{\beta k}|^2 + 2 \sum_{k>j} \mathscr{R}\left(U^*_{\beta j} U_{\alpha j} U_{\beta k} U^*_{\alpha k}\right) \cos\left(\frac{\Delta m^2_{kj} L}{2E}\right) + 2 \sum_{k>j} \mathscr{I}\left(U^*_{\beta j} U_{\alpha j} U_{\beta k} U^*_{\alpha k}\right) \sin\left(\frac{\Delta m^2_{kj} L}{2E}\right). \tag{2.40}$$

We can now leave the natural units system to make the term inside the cosine and sine with no dimensions, we then have:

$$\frac{\Delta m^2_{kj} L}{2E} \frac{[eV]^2 [Km]}{[GeV]} = \frac{1}{2\hbar} \frac{\Delta m^2_{kj} L}{E} \frac{[eV][Km]}{[GeV][s]} = \frac{1}{2c\hbar} \frac{\Delta m^2_{kj} L}{E} \frac{[eV]}{[GeV]} = \frac{1}{2 \times 10^9 c\hbar} \frac{\Delta m^2_{kj} L}{E} \approx 2.54 \frac{\Delta m^2_{kj} L}{E}, \tag{2.41}$$

Eq. (2.40) then becomes:

$$P_{\nu_\alpha \to \nu_\beta} = \sum_k |U_{\alpha k} U_{\beta k}|^2 + 2 \sum_{k>j} \mathscr{R}\left(U^*_{\beta j} U_{\alpha j} U_{\beta k} U^*_{\alpha k}\right) \cos\left(2.54 \frac{\Delta m^2_{kj} L}{E}\right) + 2 \sum_{k>j} \mathscr{I}\left(U^*_{\beta j} U_{\alpha j} U_{\beta k} U^*_{\alpha k}\right) \sin\left(2.54 \frac{\Delta m^2_{kj} L}{E}\right). \tag{2.42}$$

We can now manipulate the first term of Eq. (2.42). Considering that the PMNS matrix is unitary, the following relation can be used: $UU^\dagger = \hat{\mathbb{1}}$ and, by extension, it is also true that:

$$UU^\dagger UU^\dagger = \hat{\mathbb{1}}, \tag{2.43}$$

we can write the same equation considering the components in sum notation, therefore, we will have:

$$\sum_{k,j} U^*_{\beta j} U_{\alpha j} U_{\beta k} U^*_{\alpha k} = \delta_{\alpha\beta}, \tag{2.44}$$

where $\delta_{\alpha\beta}$ is a Kronecker delta, therefore, only the diagonal terms will be equal to 1, returning to us the identity. However, we can break the summation in Eq. (2.44) as we have done prior, for $k = j$, $k > j$ and $k < j$. Already taking into consideration that the third term will be

the conjugate of the second, we have:

$$\sum_k |U_{\alpha k}U_{\beta k}|^2 + 2\sum_{k>j} \mathscr{R}\left(U^*_{\beta j}U_{\alpha j}U_{\beta k}U^*_{\alpha k}\right) = \delta_{\alpha\beta}. \tag{2.45}$$

Therefore, the first term of Eq. (2.42) can be rewritten as:

$$\sum_k |U_{\alpha k}U_{\beta k}|^2 = \delta_{\alpha\beta} - 2\sum_{k>j} \mathscr{R}\left(U^*_{\beta j}U_{\alpha j}U_{\beta k}U^*_{\alpha k}\right), \tag{2.46}$$

allowing for the the probability to be written as:

$$\begin{aligned} P_{\nu_\alpha\to\nu_\beta} = \delta_{\alpha\beta} - 2\sum_{k>j}\left\{\mathscr{R}\left(U^*_{\beta j}U_{\alpha j}U_{\beta k}U^*_{\alpha k}\right)\left[1-\cos\left(2.54\frac{\Delta m^2_{kj}L}{E}\right)\right]\right\} \\ + 2\sum_{k>j}\mathscr{I}\left(U^*_{\beta j}U_{\alpha j}U_{\beta k}U^*_{\alpha k}\right)\sin\left(2.54\frac{\Delta m^2_{kj}L}{E}\right), \end{aligned} \tag{2.47}$$

applying the identity $\sin^2 x = \frac{1-\cos(2x)}{2}$ we obtain:

$$\begin{aligned} P_{\nu_\alpha\to\nu_\beta} = \delta_{\alpha\beta} - 4\sum_{k>j}\mathscr{R}\left(U^*_{\beta j}U_{\alpha j}U_{\beta k}U^*_{\alpha k}\right)\sin^2\left(1.27\frac{\Delta m^2_{kj}L}{E}\right) \\ + 2\sum_{k>j}\mathscr{I}\left(U^*_{\beta j}U_{\alpha j}U_{\beta k}U^*_{\alpha k}\right)\sin\left(2.54\frac{\Delta m^2_{kj}L}{E}\right). \end{aligned} \tag{2.48}$$

We can now take Eq. (2.48) and calculate the oscillation from $\nu_\mu \to \nu_\tau$. Given that we are considering a two flavor scenario, there cannot be CP violation, for the mechanism for this violation needs at least three generations of fermions [41]. Hence, we can consider just the real part of the probability.

$$P_{\nu_\mu\to\nu_\tau} = -4\sum_{k>j} U_{\tau j}U_{\mu j}U_{\tau k}U_{\mu k}\sin^2\left(1.27\frac{\Delta m^2_{kj}L}{E}\right), \tag{2.49}$$

$$
\begin{aligned}
P_{\nu_\mu \to \nu_\tau} = -4 \Bigg[& U_{\tau 1} U_{\mu 1} U_{\tau 2} U_{\mu 2} \sin^2 \left(1.27 \frac{\Delta m^2_{21} L}{E} \right) \\
& + U_{\tau 1} U_{\mu 1} U_{\tau 3} U_{\mu 3} \sin^2 \left(1.27 \frac{\Delta m^2_{31} L}{E} \right) \\
& + U_{\tau 2} U_{\mu 2} U_{\tau 3} U_{\mu 3} \sin^2 \left(1.27 \frac{\Delta m^2_{32} L}{E} \right) \Bigg] .
\end{aligned} \tag{2.50}
$$

If we now consider the limit case where $\sin\theta_{13} \to 0$, $\Delta m^2_{21} \to 0$ we can recover the oscillation probability of $\nu_\mu \to \nu_\tau$ in two flavors. The Δm^2_{21} condition will make the first term of the sum to go to zero, hence, we will have:

$$
\begin{aligned}
P_{\nu_\mu \to \nu_\tau} = -4 \Bigg[& U_{\tau 1} U_{\mu 1} U_{\tau 3} U_{\mu 3} \sin^2 \left(1.27 \frac{\Delta m^2_{31} L}{E} \right) \\
& + U_{\tau 2} U_{\mu 2} U_{\tau 3} U_{\mu 3} \sin^2 \left(1.27 \frac{\Delta m^2_{32} L}{E} \right) \Bigg] ,
\end{aligned} \tag{2.51}
$$

we can also show that, with this condition, $\Delta m^2_{31} = \Delta m^2_{32}$. Consider the following:

$$
\Delta m^2_{31} = m^2_3 - m^2_1 \tag{2.52}
$$

$$
= m^2_3 - m^2_2 + m^2_2 - m^2_1 \tag{2.53}
$$

$$
= \Delta m^2_{32} + \Delta m^2_{21} , \tag{2.54}
$$

taking our limiting case into account, we will have the equality proposed. Therefore, the sine terms within the probability are the same, hence:

$$
P_{\nu_\mu \to \nu_\tau} = -4 \left[\sin^2 \left(1.27 \frac{\Delta m^2_{32} L}{E} \right) \left(U_{\tau 1} U_{\mu 1} U_{\tau 3} U_{\mu 3} + U_{\tau 2} U_{\mu 2} U_{\tau 3} U_{\mu 3} \right) \right] . \tag{2.55}
$$

The sine condition will make the PMNS matrix, defined in Eq. (2.19) to be:

$$U_{PMNS} = \begin{pmatrix} c_{12} & s_{12} & 0 \\ -s_{12}c_{23} & c_{12}c_{23} & s_{23} \\ s_{12}s_{23} & -c_{12}s_{23} & c_{23} \end{pmatrix}, \tag{2.56}$$

we can read the PMNS matrix as:

$$U_{PMNS} = \begin{pmatrix} U_{e1} & U_{e2} & U_{e3} \\ U_{\mu 1} & U_{\mu 2} & U_{\mu 3} \\ U_{\tau 1} & U_{\tau 2} & U_{\tau 3} \end{pmatrix}, \tag{2.57}$$

therefore, we can manipulate the terms of the probability that have the elements of the PMNS matrix as:

$$U_{\tau 1}U_{\mu 1}U_{\tau 3}U_{\mu 3} + U_{\tau 2}U_{\mu 2}U_{\tau 3}U_{\mu 3} = \tag{2.58}$$

$$(s_{12}s_{23})(-s_{12}c_{23})(c_{23})(s_{23}) + (-c_{12}s_{23})(c_{12}c_{23})(c_{23})(s_{23}) = \tag{2.59}$$

$$-s_{12}^2c_{23}^2s_{23}^2 - c_{12}^2c_{23}^2s_{23}^2 = \tag{2.60}$$

$$-c_{23}^2s_{23}^2(s_{12}^2 + c_{12}^2) = \tag{2.61}$$

$$-c_{23}^2s_{23}^2. \tag{2.62}$$

Our probability can then be written as:

$$P_{\nu_\mu \to \nu_\tau} = 4\left[\cos^2(\theta_{23})\sin^2(\theta_{23})\sin^2\left(1.27\frac{\Delta m_{32}^2 L}{E}\right)\right], \tag{2.63}$$

applying the trigonometric identity $\sin(x)\cos(x) = \frac{\sin(2x)}{2}$ we get the final probability of this transition:

$$P_{\nu_\mu \to \nu_\tau} = \sin^2(2\theta_{23})\sin^2\left(1.27\frac{\Delta m_{32}^2 L}{E}\right), \tag{2.64}$$

given that $P_{\nu_\alpha \to \nu_\alpha} + P_{\nu_\alpha \to \nu_\beta} = 1$, the survival probability is:

$$P_{\nu_\mu \to \nu_\mu} = 1 - \sin^2(2\theta_{23}) \sin^2\left(1.27 \frac{\Delta m^2_{32} L}{E}\right). \tag{2.65}$$

2.6 Three flavor oscillation with decay in vacuum

The neutrino decay was an alternative solution given to describe the zenith angle dependence[4] in the early Super-Kamiokande data [3]. This hypothesis was proposed by Barger, Learned, Pakvasa and Weiler in 1998, suggesting that the data could be explained by a decay channel [43].

This model was already rejected as a major phenomenon [4] but can still be a secondary one when considering the oscillation as the primarily effect present.

To consider its presence, we need to change the formalism of the standard oscillation, now adding a new matrix to the Hamiltonian in the mass basis to consider the effects of decay, as given as [44]:

$$H_0 = \begin{pmatrix} E_1 & 0 & 0 \\ 0 & E_2 & 0 \\ 0 & 0 & E_3 \end{pmatrix} - \frac{i}{2E} \begin{pmatrix} \alpha_1 & 0 & 0 \\ 0 & \alpha_2 & 0 \\ 0 & 0 & \alpha_3 \end{pmatrix}, \tag{2.66}$$

the complex matrix being added is the $i\Lambda$ matrix. It will be the one responsible for adding an exponential for the decay. The α parameters are the phases on the exponential being responsible for the physics of the decay phenomenon.

It will be in our interest to, later, consider only α_3 not to be 0. This is because both the α_1 and α_2 are already well restrained from the solar neutrino data [2, 3, 45].

[4] If we consider the two flavor oscillation of $\nu_\mu \to \nu_\tau$, the surival probability becomes $P_{\mu\mu} = 1 - \sin^2(2\theta_{23}) \sin\left(\frac{\Delta m^2_{32} L}{4E}\right)$ which was the one used to describe the zenith angle with standard oscillation. However, the decay proposal shows that the same data for the zenith angle can be explained using the following approximated model $P_{\mu\mu} = \sin^4\theta_{23} + \cos^4\theta_{23} \exp(-\alpha_2 L/E)$, creating a dependence of the zenith angle and the decay parameter α_2 [42].

Substituing $\lambda_i = -\frac{\alpha_i}{2E}$ we can rewrite it as:

$$H_0 = \begin{pmatrix} E_1 + i\lambda_1 & 0 & 0 \\ 0 & E_2 + i\lambda_2 & 0 \\ 0 & 0 & E_3 + i\lambda_3 \end{pmatrix}. \tag{2.67}$$

Since this matrix is on the mass space, we can arrive at its evolution with respect to time:

$$|\nu_k(t)\rangle = \exp\left[-i\left(E_k + i\lambda_k\right)t\right]|\nu_k\rangle\,, \tag{2.68}$$

the remaining deduction is analogous with the prior, therefore the flavor evolution can be written using Eq. (2.10):

$$|\nu_\alpha(t)\rangle = \sum_k U^*_{\alpha k} \exp\left[-i\left(E_k + i\lambda_k\right)t\right]|\nu_k\rangle\,, \tag{2.69}$$

taking the amplitude of the transition $\nu_\alpha \to \nu_\beta$ and making the same simplifications as prior, we have:

$$\langle \nu_\beta | \nu_\alpha(t)\rangle = \left(\sum_j U_{\beta j}\langle \nu_j|\right)\left(\sum_k U^*_{\alpha k}\exp\left[-i\left(E_k + i\lambda_k\right)t\right]|\nu_k\rangle\right), \tag{2.70a}$$

$$= \sum_k U_{\beta k}U^*_{\alpha k}\exp\left[-i\left(E_k + i\lambda_k\right)t\right], \tag{2.70b}$$

then, we can write the probability as the modulus squared of the transition, hence:

$$P_{\nu_\alpha\to\nu_\beta} = \left(\sum_j U^*_{\beta j}U_{\alpha j}\exp\left[i\left(E_j - i\lambda_j\right)t\right]\right)\left(\sum_k U_{\beta k}U^*_{\alpha k}\exp\left[-i\left(E_k + i\lambda_k\right)t\right]\right), \tag{2.71a}$$

$$= \sum_{k,j} U^*_{\beta j}U_{\alpha j}U_{\beta k}U^*_{\alpha k}\exp\left[-i(E_k - E_j)t\right]\exp\left[(\lambda_k + \lambda_j)t\right], \tag{2.71b}$$

separating the sums for $k = j$, $k > j$ and $k < j$ we can make the following transformation:

$$\begin{aligned} P_{\nu_\alpha \to \nu_\beta} &= \sum_k |U_{\alpha k} U_{\beta k}|^2 \exp(2\lambda_k t) \\ &\quad + 2 \sum_{k>j} \mathscr{R}\left(U^*_{\beta j} U_{\alpha j} U_{\beta k} U^*_{\alpha k} \exp\left[-i(E_k - E_j)t\right] \exp\left[(\lambda_k + \lambda_j)t\right] \right), \end{aligned} \tag{2.72}$$

we can now make the approximation of $t \approx L$ and use Eq. (2.35), giving us:

$$\begin{aligned} P_{\nu_\alpha \to \nu_\beta} &= \sum_k |U_{\alpha k} U_{\beta k}|^2 \exp(2\lambda_k L) \\ &\quad + 2 \sum_{k>j} \mathscr{R}\left(U^*_{\beta j} U_{\alpha j} U_{\beta k} U^*_{\alpha k} \exp\left[-i\frac{\Delta m^2_{kj} L}{2E}\right] \exp\left[(\lambda_k + \lambda_j)L\right] \right), \end{aligned} \tag{2.73}$$

expanding in terms of the cosine and sine for the second exponential we get:

$$\begin{aligned} P_{\nu_\alpha \to \nu_\beta} &= \sum_k |U_{\alpha k} U_{\beta k}|^2 \exp(2\lambda_k L) \\ &\quad + 2 \sum_{k>j} \mathscr{R}\left(U^*_{\beta j} U_{\alpha j} U_{\beta k} U^*_{\alpha k} \right) \exp\left[(\lambda_k + \lambda_j)L\right] \cos\left(\frac{\Delta m^2_{kj} L}{2E}\right) \\ &\quad + 2 \sum_{k>j} \mathscr{I}\left(U^*_{\beta j} U_{\alpha j} U_{\beta k} U^*_{\alpha k} \right) \exp\left[(\lambda_k + \lambda_j)L\right] \sin\left(\frac{\Delta m^2_{kj} L}{2E}\right), \end{aligned} \tag{2.74}$$

we can now substitute the value of λ in terms of α:

$$\begin{aligned} P_{\nu_\alpha \to \nu_\beta} &= \sum_k |U_{\alpha k} U_{\beta k}|^2 \exp\left(-\alpha_k \frac{L}{E}\right) \\ &\quad + 2 \sum_{k>j} \mathscr{R}\left(U^*_{\beta j} U_{\alpha j} U_{\beta k} U^*_{\alpha k} \right) \exp\left[-(\alpha_k + \alpha_j)\frac{L}{2E}\right] \cos\left(\frac{\Delta m^2_{kj} L}{2E}\right) \\ &\quad + 2 \sum_{k>j} \mathscr{I}\left(U^*_{\beta j} U_{\alpha j} U_{\beta k} U^*_{\alpha k} \right) \exp\left[-(\alpha_k + \alpha_j)\frac{L}{2E}\right] \sin\left(\frac{\Delta m^2_{kj} L}{2E}\right). \end{aligned} \tag{2.75}$$

We now have to consider the constants c and $\hbar$. For the arguments inside the sine and cosine we already know from Eq. (2.41). For the exponentials, we simply define the units of α to be $[GeV]/[km]$. Applying the convertions into Eq. (2.75) we arrive at the probability of

the neutrino oscillation with decay in vacuum for the α parameter:

$$\begin{aligned} P_{\nu_\alpha \to \nu_\beta} = & \sum_k |U_{\alpha k} U_{\beta k}|^2 \exp\left(-\alpha_k \frac{L}{E}\right) \\ & + 2 \sum_{k>j} \mathscr{R}\left(U^*_{\beta j} U_{\alpha j} U_{\beta k} U^*_{\alpha k}\right) \exp\left[-(\alpha_k + \alpha_j)\frac{L}{2E}\right] \cos\left(2.54 \frac{\Delta m^2_{kj} L}{E}\right) \\ & + 2 \sum_{k>j} \mathscr{I}\left(U^*_{\beta j} U_{\alpha j} U_{\beta k} U^*_{\alpha k}\right) \exp\left[-(\alpha_k + \alpha_j)\frac{L}{2E}\right] \sin\left(2.54 \frac{\Delta m^2_{kj} L}{E}\right). \end{aligned} \tag{2.76}$$

It is important to enunciate that, in Eq. (2.66), the units of α_i are in $[eV]^2$, however, we defined them now to be in $[GeV]/[km]$. This does not create any problems, given that we can use the following relation to change from one set of units to the other:

$$[eV]^2 = \frac{1}{\hbar}\frac{[eV]^2}{[eV][s]} = \frac{1}{c\hbar}\frac{[eV][s]}{[s][km]} = \frac{1}{10^9 c\hbar}\frac{[GeV]}{[km]} \approx 5.068 \frac{[GeV]}{[km]}. \tag{2.77}$$

Considering a simpler case of the transition $\nu_\mu \to \nu_\tau$ we can now obtain the oscillation probability with decay in vacuum. Given that we are with only two flavors, we can consider just the real part of Eq. (2.76). Expanding the terms, and already considering $\alpha_1 \to 0$ and $\alpha_2 \to 0$, we will have:

$$\begin{aligned} P_{\nu_\mu \to \nu_\tau} = & |U_{\mu 1} U_{\tau 1}|^2 + |U_{\mu 2} U_{\tau 2}|^2 + |U_{\mu 3} U_{\tau 3}|^2 \exp\left(-\alpha_3 \frac{L}{E}\right) \\ & + 2 \left\{ U_{\tau 1} U_{\mu 1} U_{\tau 2} U_{\mu 2} \cos\left(2.54 \frac{\Delta m^2_{21} L}{E}\right) \right. \\ & + U_{\tau 1} U_{\mu 1} U_{\tau 3} U_{\mu 3} \exp\left(-\alpha_3 \frac{L}{2E}\right) \cos\left(2.54 \frac{\Delta m^2_{31} L}{E}\right) \\ & \left. + U_{\tau 2} U_{\mu 2} U_{\tau 3} U_{\mu 3} \exp\left(-\alpha_3 \frac{L}{2E}\right) \cos\left(2.54 \frac{\Delta m^2_{32} L}{E}\right) \right\}. \end{aligned} \tag{2.78}$$

We can now consider that $\Delta m^2_{21} \to 0$, which also implies that $\Delta m^2_{31} = \Delta m^2_{32}$ as we showed in the previous section, therefore, our probability becomes:

$$\begin{aligned} P_{\nu_\mu \to \nu_\tau} = & |U_{\mu 1} U_{\tau 1}|^2 + |U_{\mu 2} U_{\tau 2}|^2 + |U_{\mu 3} U_{\tau 3}|^2 \exp\left(-\alpha_3 \frac{L}{E}\right) \\ & + 2 \left\{ U_{\tau 1} U_{\mu 1} U_{\tau 2} U_{\mu 2} + \exp\left(-\alpha_3 \frac{L}{2E}\right) \cos\left(2.54 \frac{\Delta m^2_{32} L}{E}\right) \right. \\ & \left. \times \left(U_{\tau 1} U_{\mu 1} U_{\tau 3} U_{\mu 3} + U_{\tau 2} U_{\mu 2} U_{\tau 3} U_{\mu 3}\right) \right\}. \end{aligned} \tag{2.79}$$

Considering now that $\sin\theta_{13} \to 0$ our PMNS matrix can be again written as Eq. (2.56):

$$U_{PMNS} = \begin{pmatrix} c_{12} & s_{12} & 0 \\ -s_{12} c_{23} & c_{12} c_{23} & s_{23} \\ s_{12} s_{23} & -c_{12} s_{23} & c_{23} \end{pmatrix},$$

therefore, we already now that:

$$U_{\tau 1} U_{\mu 1} U_{\tau 3} U_{\mu 3} + U_{\tau 2} U_{\mu 2} U_{\tau 3} U_{\mu 3} = -c^2_{23} s^2_{23},$$

our probability can then be written as:

$$\begin{aligned} P_{\nu_\mu \to \nu_\tau} = & |U_{\mu 1} U_{\tau 1}|^2 + |U_{\mu 2} U_{\tau 2}|^2 + |U_{\mu 3} U_{\tau 3}|^2 \exp\left(-\alpha_3 \frac{L}{E}\right) \\ & + 2 \left\{ U_{\tau 1} U_{\mu 1} U_{\tau 2} U_{\mu 2} - c^2_{23} s^2_{23} \exp\left(-\alpha_3 \frac{L}{2E}\right) \cos\left(2.54 \frac{\Delta m^2_{32} L}{E}\right) \right\}, \end{aligned} \tag{2.80}$$

opening the other terms of the PMNS matrix, we have:

$$\begin{aligned} P_{\nu_\mu \to \nu_\tau} = & s^4_{12} c^2_{23} s^2_{23} + c^4_{12} c^2_{23} s^2_{23} + c^2_{23} s^2_{23} \exp\left(-\alpha_3 \frac{L}{E}\right) \\ & + 2 \left\{ s^2_{12} s^2_{23} c^2_{23} c^2_{12} - c^2_{23} s^2_{23} \exp\left(-\alpha_3 \frac{L}{2E}\right) \cos\left(2.54 \frac{\Delta m^2_{32} L}{E}\right) \right\}, \end{aligned} \tag{2.81}$$

we can rearrange so we have the terms that have the decay parameter and the ones that do not have:

$$\begin{aligned} P_{\nu_\mu \to \nu_\tau} &= s_{12}^4 c_{23}^2 s_{23}^2 + c_{12}^4 c_{23}^2 s_{23}^2 + 2 s_{12}^2 s_{23}^2 c_{23}^2 c_{12}^2 \\ &+ \left\{ c_{23}^2 s_{23}^2 \exp\left(-\alpha_3 \frac{L}{E}\right) - 2 c_{23}^2 s_{23}^2 \exp\left(-\alpha_3 \frac{L}{2E}\right) \cos\left(2.54 \frac{\Delta m_{32}^2 L}{E}\right) \right\}, \end{aligned} \tag{2.82}$$

$$\begin{aligned} P_{\nu_\mu \to \nu_\tau} &= c_{23}^2 s_{23}^2 \left(s_{12}^4 + 2 s_{12}^2 c_{12}^2 + c_{12}^4\right) \\ &+ \left\{ c_{23}^2 s_{23}^2 \exp\left(-\alpha_3 \frac{L}{E}\right) - 2 c_{23}^2 s_{23}^2 \exp\left(-\alpha_3 \frac{L}{2E}\right) \cos\left(2.54 \frac{\Delta m_{32}^2 L}{E}\right) \right\}, \end{aligned} \tag{2.83}$$

the $\left(s_{12}^4 + 2 s_{12}^2 c_{12}^2 + c_{12}^4\right)$ term, is the same as $(s_{12}^2 + c_{12}^2)^2$ and, therefore, equal to 1:

$$\begin{aligned} P_{\nu_\mu \to \nu_\tau} &= c_{23}^2 s_{23}^2 + c_{23}^2 s_{23}^2 \exp\left(-\alpha_3 \frac{L}{E}\right) \\ &- 2 c_{23}^2 s_{23}^2 \exp\left(-\alpha_3 \frac{L}{2E}\right) \cos\left(2.54 \frac{\Delta m_{32}^2 L}{E}\right), \end{aligned} \tag{2.84}$$

we can factorize the $c_{23}^2 s_{23}^2$ term and also apply the following trigonometric identity $\cos^2(x)\sin^2(x) = \sin^2(2x)/4$:

$$P_{\nu_\mu \to \nu_\tau} = \frac{\sin^2(2\theta_{23})}{4} \left[1 + \exp\left(-\alpha_3 \frac{L}{E}\right) - 2 \exp\left(-\alpha_3 \frac{L}{2E}\right) \cos\left(2.54 \frac{\Delta m_{32}^2 L}{E}\right)\right], \tag{2.85}$$

finally, we can distribute a factor of $1/2$ and arrive at the final expression:

$$P_{\nu_\mu \to \nu_\tau} = \frac{\sin^2(2\theta_{23})}{2} \left[\frac{1}{2} + \frac{1}{2} \exp\left(-\alpha_3 \frac{L}{E}\right) - \exp\left(-\alpha_3 \frac{L}{2E}\right) \cos\left(2.54 \frac{\Delta m_{32}^2 L}{E}\right)\right]. \tag{2.86}$$

If we consider that there is no decay, that is $\alpha_3 \to 0$, we have:

$$P_{\nu_\mu \to \nu_\tau} = \frac{\sin^2(2\theta_{23})}{2} \left[1 - \cos\left(2.54 \frac{\Delta m_{32}^2 L}{E}\right)\right], \tag{2.87}$$

$$P_{\nu_\mu \to \nu_\tau} = \sin^2(2\theta_{23}) \sin^2\left(1.27 \frac{\Delta m^2_{32} L}{E}\right), \tag{2.88}$$

recovering the standard oscillation probability.

2.7 Three flavor oscillation with decay in matter

Finally, we want to have a way to calculate the probability of neutrino oscillations with decay in matter. However, this is not a trivial calculation, normally being made using a numerical approach.

Besides, until now we have considered just the mass basis for the Hamiltonian and, for matter effect, we will need to use the flavor basis. So, as a first approach, to show that both basis will yield the same result, let us consider a simple case of the oscillation probability of $\nu_\mu \to \nu_\tau$ considering a two flavor scenario in vacuum.

2.7.1 Two flavor standard oscillation in the flavor basis

In the flavor basis, we can define the effective Hamiltonian as such:

$$\mathscr{H}_f = U H_0 U^\dagger, \tag{2.89}$$

where H_0 is our Hamiltonian in the mass basis and the U term are the PMNS matrix.

Firstly, we need to manipulate the mass matrix (H_0) to a more convinent way such that the Δm^2_{kj} term appears. Since the transition being analysed is $\nu_\mu \to \nu_\tau$ with two flavors, the matrix becomes:

$$H_0 = \begin{pmatrix} E_2 & 0 \\ 0 & E_3 \end{pmatrix}, \tag{2.90}$$

we can manipulate this equation by subtracting or adding a term which is proportional to the identity matrix, since it only changes a phase [19], that does not alter the physics of

oscillations:

$$H_0 = \begin{pmatrix} E_2 & 0 \\ 0 & E_3 \end{pmatrix} - E_2\hat{\mathbb{1}}, \tag{2.91a}$$

$$= \begin{pmatrix} 0 & 0 \\ 0 & E_3 - E_2 \end{pmatrix}, \tag{2.91b}$$

applying (2.35)

$$H_0 = \frac{1}{2E}\begin{pmatrix} 0 & 0 \\ 0 & \Delta m^2_{32} \end{pmatrix}, \tag{2.92}$$

with this new equation we can now rewrite the $\mathscr{H}_f$ matrix, given that for the transition being used we can use the U_{23} matrix:

$$U_{23} = \begin{pmatrix} \cos(\theta_{23}) & \sin(\theta_{23}) \\ -\sin(\theta_{23}) & \cos(\theta_{23}) \end{pmatrix}, \tag{2.93}$$

therefore,

$$\mathscr{H}_f = \frac{1}{2E}\begin{pmatrix} \cos(\theta_{23}) & \sin(\theta_{23}) \\ -\sin(\theta_{23}) & \cos(\theta_{23}) \end{pmatrix}\begin{pmatrix} 0 & 0 \\ 0 & \Delta m^2_{32} \end{pmatrix}\begin{pmatrix} \cos(\theta_{23}) & -\sin(\theta_{23}) \\ \sin(\theta_{23}) & \cos(\theta_{23}) \end{pmatrix}, \tag{2.94a}$$

$$= \frac{\Delta m^2_{32}}{2E}\begin{pmatrix} \sin^2(\theta_{23}) & \cos(\theta_{23})\sin(\theta_{23}) \\ \cos(\theta_{23})\sin(\theta_{23}) & \cos^2(\theta_{23}) \end{pmatrix}, \tag{2.94b}$$

we can again subtract a constant value from the matrix to apply some trigonometric transformations on the arguments of $\mathscr{H}_f$, in this case, subtracting $1/2$:

$$\mathscr{H}_f = \frac{\Delta m^2_{32}}{2E}\begin{pmatrix} \sin^2(\theta_{23}) - 1/2 & \cos(\theta_{23})\sin(\theta_{23}) \\ \cos(\theta_{23})\sin(\theta_{23}) & \cos^2(\theta_{23}) - 1/2 \end{pmatrix}, \tag{2.95}$$

the following trigonometric identities can be applied:

$$\cos(x)\sin(x) = \frac{\sin(2x)}{2}, \tag{2.96a}$$

$$\cos^2(x) - \frac{1}{2} = \frac{\cos(2x)}{2}, \tag{2.96b}$$

$$\sin^2(x) - \frac{1}{2} = \frac{-\cos(2x)}{2}, \tag{2.96c}$$

giving us the following result:

$$\mathscr{H}_f = \frac{\Delta m^2_{32}}{4E}\begin{pmatrix} -\cos(2\theta_{23}) & \sin(2\theta_{23}) \\ \sin(2\theta_{23}) & \cos(2\theta_{23}) \end{pmatrix}. \tag{2.97}$$

Diagonalizing this matrix we will arrive at the eigenvalues of this Hamiltonian, being them:

$$\lambda_+ = \frac{\Delta m^2_{32}}{4E} \qquad\qquad \lambda_- = \frac{-\Delta m^2_{32}}{4E}, \tag{2.98}$$

we can now obtain the normalized eigenvectors for both these values:

$$|\psi_+\rangle = \begin{pmatrix} \sin(\theta_{23}) \\ \cos(\theta_{23}) \end{pmatrix} \qquad\qquad |\psi_-\rangle = \begin{pmatrix} -\cos(\theta_{23}) \\ \sin(\theta_{23}) \end{pmatrix}, \tag{2.99}$$

the following eigenvectors can be identified as $|\psi_+\rangle = |\nu_2\rangle$ and $|\psi_-\rangle = |\nu_3\rangle$. Given this information, and that we have the eigenvalues, we arreange to their time evolution.

Since we have the eigenvalues for the mass states, we can write their time evolution as applying that $t \approx L$:

$$|\nu_2(t)\rangle = \exp\left(\frac{-i\Delta m^2_{32}L}{4E}\right)|\nu_2\rangle\,, \tag{2.100a}$$

$$|\nu_3(t)\rangle = \exp\left(\frac{i\Delta m^2_{32}L}{4E}\right)|\nu_3\rangle\,, \tag{2.100b}$$

the flavors states are connected to the mass ones by the U_{23} matrix:

$$\begin{pmatrix} \nu_\mu \\ \nu_\tau \end{pmatrix} = \begin{pmatrix} \cos(\theta_{23}) & \sin(\theta_{23}) \\ -\sin(\theta_{23}) & \cos(\theta_{23}) \end{pmatrix} \begin{pmatrix} \nu_2 \\ \nu_3 \end{pmatrix}, \tag{2.101}$$

and therefore we arrive at the following equations:

$$\left|\nu_\mu\right\rangle = \cos(\theta_{23})\left|\nu_2\right\rangle + \sin(\theta_{23})\left|\nu_3\right\rangle, \tag{2.102a}$$

$$\left|\nu_\tau\right\rangle = -\sin(\theta_{23})\left|\nu_2\right\rangle + \cos(\theta_{23})\left|\nu_3\right\rangle. \tag{2.102b}$$

We want to see the transition $\nu_\mu \to \nu_\tau$ so, applying Eqs. (2.100a) in (2.102a), we obtain the time evolution of the ν_μ flavor state:

$$\left|\nu_\mu(t)\right\rangle = \cos(\theta_{23})\left[\exp\left(\frac{-i\Delta m^2_{32}L}{4E}\right)\right]\left|\nu_2\right\rangle + \sin(\theta_{23})\left[\exp\left(\frac{i\Delta m^2_{32}L}{4E}\right)\right]\left|\nu_3\right\rangle, \tag{2.103}$$

taking the projection onto the ν_τ, given that the mass states are orthonormal, the cross terms vanishes, hence we have:

$$\begin{aligned} \left\langle\nu_\tau\middle|\nu_\mu(t)\right\rangle &= -\sin(\theta_{23})\cos(\theta_{23})\exp\left(\frac{-i\Delta m^2_{32}L}{4E}\right) \\ &\quad + \sin(\theta_{23})\cos(\theta_{23})\exp\left(\frac{i\Delta m^2_{32}L}{4E}\right), \end{aligned} \tag{2.104a}$$

$$= \frac{\sin(2\theta_{23})}{2}\left[\exp\left(\frac{i\Delta m^2_{32}L}{4E}\right) - \exp\left(\frac{-i\Delta m^2_{32}L}{4E}\right)\right], \tag{2.104b}$$

taking the modulus square we arrive, once again, at the probability:

$$P_{\nu_\mu\to\nu_\tau} = \frac{\sin^2(2\theta_{23})}{4}\left\{2 - \left[\exp\left(\frac{i\Delta m^2_{32}L}{2E}\right) + \exp\left(\frac{-i\Delta m^2_{32}L}{2E}\right)\right]\right\}, \tag{2.105a}$$

$$= \frac{\sin^2(2\theta_{23})}{2}\left\{1 - \frac{1}{2}\left[\exp\left(\frac{i\Delta m^2_{32}L}{2E}\right) + \exp\left(\frac{-i\Delta m^2_{32}L}{2E}\right)\right]\right\}, \tag{2.105b}$$

using the complex identity $\cos(z) = \frac{e^{iz}+e^{-iz}}{2}$:

$$P_{\nu_\mu \to \nu_\tau} = \frac{\sin^2(2\theta_{23})}{2}\left[1 - \cos\left(\frac{\Delta m^2_{32} L}{2E}\right)\right], \tag{2.106}$$

taking the double angle property for the cosine we finally arrive at:

$$P_{\nu_\mu \to \nu_\tau} = \sin^2(2\theta_{23})\sin^2\left(\frac{\Delta m^2_{32} L}{4E}\right). \tag{2.107}$$

Leaving the natural units, using the conversion on Eq. (2.41), we obtain the transition probability as before:

$$P_{\nu_\mu \to \nu_\tau} = \sin^2(2\theta_{23})\sin^2\left(1.27\frac{\Delta m^2_{32} L}{E}\right), \tag{2.108}$$

which is what we obtained with the other formalism, the survival probability then becomes:

$$P_{\nu_\mu \to \nu_\mu} = 1 - \sin^2(2\theta_{23})\sin^2\left(1.27\frac{\Delta m^2_{32} L}{E}\right). \tag{2.109}$$

As said prior, this formalism of using the flavor basis will yield the same result as using the mass basis. However, for more complex models, as the one we are going to approach, it can be interesting to use a numerical model instead of an analytic formula (that not all models do have).

In Section 2.6 we have considered a new matrix to add the decay effect. Now, we wish to the same for matter effects.

2.7.2 Matter effects

Although neutrinos have a small cross section ($10^{-42} - 10^{-43}\ m^2/GeV$) [36], they can still interact with particles in Earth's medium, such as neutrons (n), protons (p) and electrons

(e) [19]. This effect was firstly propossed by Mikheyev, Smirnov and Wolfestein, the MSW matter effect [36, 46, 47].

One of the first interactions to consider is if a neutrino in matter does exchange a Z boson with one of the particles cited above. However, given that the Earth's density of electrons is equal to the one of protons (that is to say, it is electrically neutral) there will be no contribution. This happens because the Z coupling to electrons is the same of the one with protons, but with a changed sign [48].

The interaction of all three flavor of neutrinos with the neutron can also be ignored. This is due the interactions that arise from NC do not change the phases of the neutrino flavors and, therefore, do not add any mixing effects [49].

Another interaction that may happen is the one with ν_e with e; ν_μ with μ and ν_τ with the τ particles. The presence of muon and tau particles in Earth is negligible [36]. We just need to consider the interactions of ν_e with e via the W boson, which give arise to the following extra potential [48, 49]:

$$V_{CC} = \pm\sqrt{2}G_F N_e, \tag{2.110}$$

where G_F is Fermi coupling constant and N_e is the number of electrons per unit volume. If the beam is of neutrinos, we take the positive sign and the negative for antineutrinos [50].

The MSW effect happens with the flavor basis, and hence, we can change its Hamiltonian to the following form:

$$\mathscr{H}_f = UH_0U^\dagger + V_{CC}\begin{pmatrix} 1 & 0 & 0 \\ 0 & 0 & 0 \\ 0 & 0 & 0 \end{pmatrix}. \tag{2.111}$$

2.7.3 Decay in matter

Now that we have seen the decay phenomenon and the matter effects, we can easily built the Hamiltonian, in flavor basis, that describe the decay in matter:

$$\mathscr{H}_f = U\left[\begin{pmatrix} E_1 & 0 & 0 \\ 0 & E_2 & 0 \\ 0 & 0 & E_3 \end{pmatrix} - \frac{i}{2E}\begin{pmatrix} \alpha_1 & 0 & 0 \\ 0 & \alpha_2 & 0 \\ 0 & 0 & \alpha_3 \end{pmatrix}\right] U^\dagger + V_{CC}\begin{pmatrix} 1 & 0 & 0 \\ 0 & 0 & 0 \\ 0 & 0 & 0 \end{pmatrix}, \tag{2.112}$$

we can subtract $E_1\hat{\mathbb{1}}$ from the E_i matrix (again, this shift a phase that does not alter the physics of oscillation) and using Eq. (2.35) to write in terms of the masses as follows:

$$\mathscr{H}_f = U\left[\begin{pmatrix} 0 & 0 & 0 \\ 0 & \Delta m^2_{21} & 0 \\ 0 & 0 & \Delta m^2_{31} \end{pmatrix} - \frac{i}{2E}\begin{pmatrix} \alpha_1 & 0 & 0 \\ 0 & \alpha_2 & 0 \\ 0 & 0 & \alpha_3 \end{pmatrix}\right] U^\dagger + V_{CC}\begin{pmatrix} 1 & 0 & 0 \\ 0 & 0 & 0 \\ 0 & 0 & 0 \end{pmatrix}, \tag{2.113}$$

finally, we can consider $\alpha_1 = \alpha_2 = 0$ given their constrains and only consider α_3 [3, 51]:

$$\mathscr{H}_f = U\left[\begin{pmatrix} 0 & 0 & 0 \\ 0 & \Delta m^2_{21} & 0 \\ 0 & 0 & \Delta m^2_{31} \end{pmatrix} - \frac{i}{2E}\begin{pmatrix} 0 & 0 & 0 \\ 0 & 0 & 0 \\ 0 & 0 & \alpha_3 \end{pmatrix}\right] U^\dagger + V_{CC}\begin{pmatrix} 1 & 0 & 0 \\ 0 & 0 & 0 \\ 0 & 0 & 0 \end{pmatrix}. \tag{2.114}$$

For this work, we will be also using the series expansions given by *Grönroos et al.* [3] for the $P_{\nu_\mu \to \nu_\mu}$ oscillation.

The series expansion being used goes as follows (still in natural units)[5]:

$$P^{(0)}_{\mu\mu} = 1 - s^2_{23}\left(1 - e^{-4\gamma\Delta}\right) - c^2_{23}s^2_{23}\left[1 - 2\cos(2\Delta)e^{-2\gamma\Delta} + e^{-4\gamma\Delta}\right], \tag{2.115}$$

[5]The upscript index in the $P_{\mu\mu}$ terms represent the respective expansion term, therefore, $P^{(0)}_{\mu\mu}$ refers to the term of order 0.

$$
\begin{aligned}
P^{(2)}_{\mu\mu} = \frac{2s^2_{13}s^2_{23}}{D^2} \Big\{ & \left[(B^2-C^2)\cos(2A\Delta) - 2BC\sin(2A\Delta)\right] c^2_{23} \\
& + \left[(B^2-C^2)\cos[2(A-1)\Delta] - 2BC\sin[2(A-1)\Delta]\right] s^2_{23} e^{-2\gamma\Delta} \\
& - [\cos(2\Delta)c^2_{23} + s^2_{23}e^{-2\gamma\Delta}](B^2-C^2-2ACD\Delta)e^{-2\gamma\Delta} \\
& + 2AB(\gamma + D\Delta)\sin(2\Delta)c^2_{23}e^{-2\gamma\Delta}\Big\} + 4\alpha c^2_{12}c^2_{23}s^2_{23}\Delta\sin(2\Delta)e^{-2\gamma\Delta},
\end{aligned}
\tag{2.116}
$$

$$
\begin{aligned}
P^{(3)}_{\mu\mu} = \frac{4\alpha s_{13}c_{12}s_{12}c_{23}s_{23}\cos\delta_{CP}}{AD} & \Big\{ A(1-A)s^2_{23}e^{-4\gamma\Delta} + D\left[c^2_{23} - \cos(2\theta_{23})\cos(2\Delta)e^{-2\gamma\Delta}\right] \\
& + B\left[\cos(2A\Delta)c^2_{23} - \left(\cos(2\Delta)c^2_{23} - \cos[2(A-1)\Delta]s^2_{23}\right)e^{-2\gamma\Delta}\right] \\
& - C\left[\sin(2A\Delta)c^2_{23} - \left(\sin(2\Delta)c^2_{23} + \sin[2(A-1)\Delta]s^2_{23}\right)e^{-2\gamma\Delta}\right]\Big\},
\end{aligned}
\tag{2.117}
$$

where the total probability is:

$$
P_{\mu\mu} = P^{(0)}_{\mu\mu} + P^{(2)}_{\mu\mu} + P^{(3)}_{\mu\mu}, \tag{2.118}
$$

the first term $P^{(1)}_{\mu\mu} = 0$ and its the reason for not showing up. In this equation, we also have the following definitions:

$$
\begin{aligned}
\Delta &= \Delta m^2_{31}\frac{L}{4E}, \\
\alpha &= \frac{\Delta m^2_{21}}{\Delta m^2_{31}}, \\
\gamma &= \frac{\alpha_3}{\Delta m^2_{31}}, \\
A &= \frac{2V_{CC}E}{\Delta m^2_{31}}, \\
B &= A - 1 - \gamma^2, \\
C &= A\gamma, \\
D &= (A-1)^2 + \gamma^2.
\end{aligned}
\tag{2.119}
$$

With this expansion, we are able to compare it with the Hamiltonian formalism in the flavor basis and also probe the effects of using this approach for the MINOS and MINOS+ data.

Chapter 3

MINOS/MINOS+ experimental apparatus

3.1 A brief introduction to MINOS and MINOS+

The Main Injector Neutrino Oscillation Search (MINOS) and MINOS+ are both long-baseline (LBL) experiments designed for the study of neutrino oscillations. They use the NuMI beamline and a 735 *km* baseline for obtaining data with an on-axis configuration [52]. They both use two identical detectors. One being the Near Detector (ND) located at Fermilab 1.04 *km* from the NuMI beam target and 90 *m* under the surface, weighing 980 tons [44, 53, 54]. The other being the Far Detector (FD) 735 *km* downstream in the Soudan Underground Laboratory, located in Minnesota, weighing 5400 tons [44, 53].

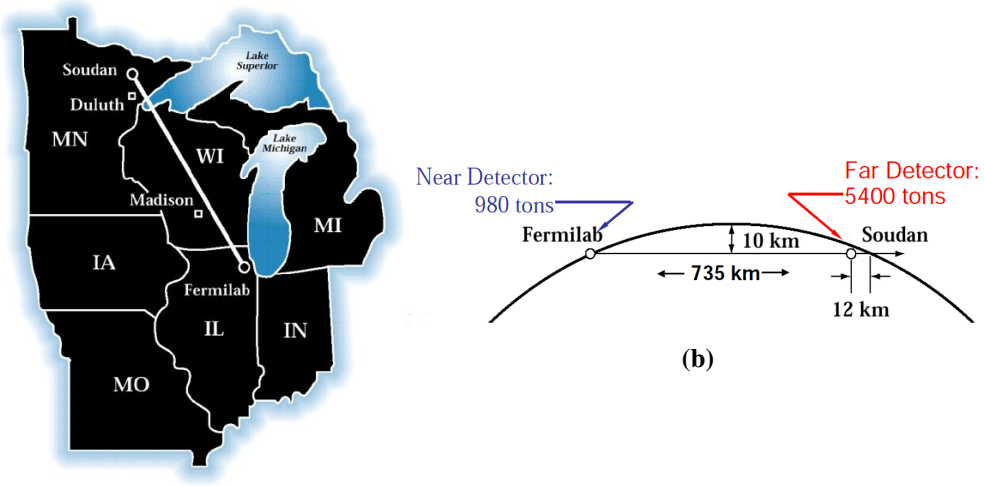

Figure 3.1: (a) Path of MINOS baseline, starting from the Fermilab, where the neutrinos are produced and the ND is located, going to Soudan, where the FD is located. (b) Representantion of the ND and FD distance, depth, location and information for both the detectors weight [44].

The MINOS experiment was firstly conceived in the late 1990s [55]. The construction

of the beam line and the experiment happened in 1999 and 2004 [44]. The experiment was designed for probing the parameter for atmospheric neutrinos and, because of that, it began taking data in 2003 [36, 55].

In 2005 the MINOS experiment started using the NuMI beamline in a low-energy and wide-band configuration with a mean energy peak at 3 GeV. This allowed the experiment to be sensitive for the following three flavor oscillation parameters: θ_{13}, θ_{23}, δ_{CP} and Δm^2_{32}. The experiment stopped collecting data in 2012 [52].

In 2012, the NuMI beam would have an upgrade for the new experiment being designed, the Neutrinos Off-axis ν_e Apperance (NOνA) [56]. Because of this, a proposal was made to still use the MINOS detectors but in a higher energy range (4-10 GeV, with a peak in 7 GeV) [57].

This new exposure began in September 2013 [58] and was expected to last for three years, being this the start of the MINOS+ experiment. The MINOS+ experiment, given the exposure for higher energies, was best suited for probing model beyond the Standard Model, such as the sterile neutrinos and extra dimensions [59].

In Figure 3.2 we can see the different energy spectras that the three cited experiments were exposed. The blue line representing the energy spectra for the NOνA, MINOS and MINOS+ experiments and their different peak of events as a function of the energy of the neutrino.

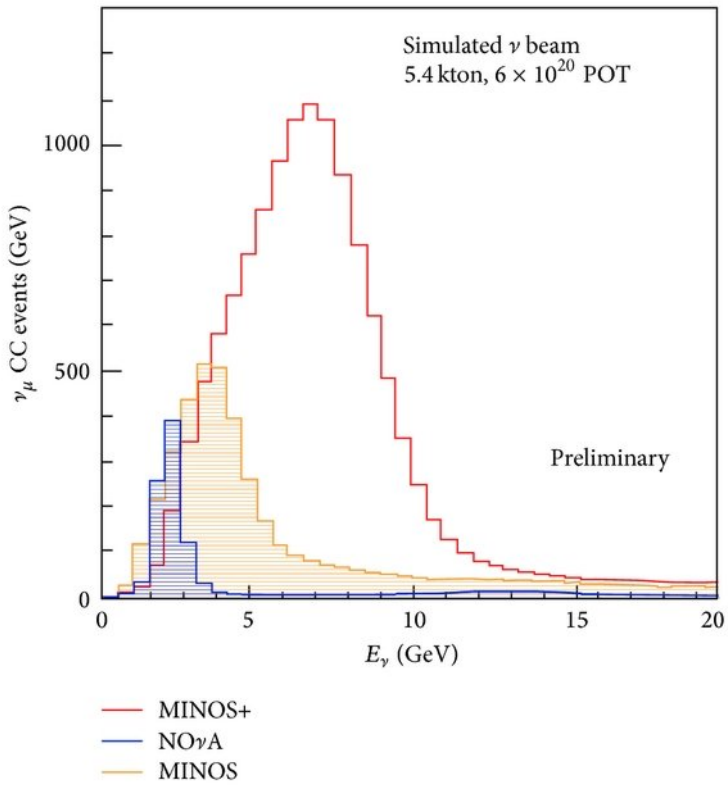

Figure 3.2: The different ν_μ energy spectra for the experiments: NOνA, MINOS and MINOS+ [59].

3.2 The NuMI beam

The NuMI beam was initially built to provide neutrinos to the MINOS and COSMOS experiments by hitting a 120 *GeV* proton beam against a graphite target. Still, the NuMI beam started to be used by some other experiments, like MINERνA, MiniBooNE, MINOS+ and NOνA [56]. After the beam started to be used by the latter its potency was upgraded to 700 *kW* [60].

3.2.1 Beam production

For guidance, Figure 3.3 shall be consulted for better understanding as the path the beam is following in the complex.

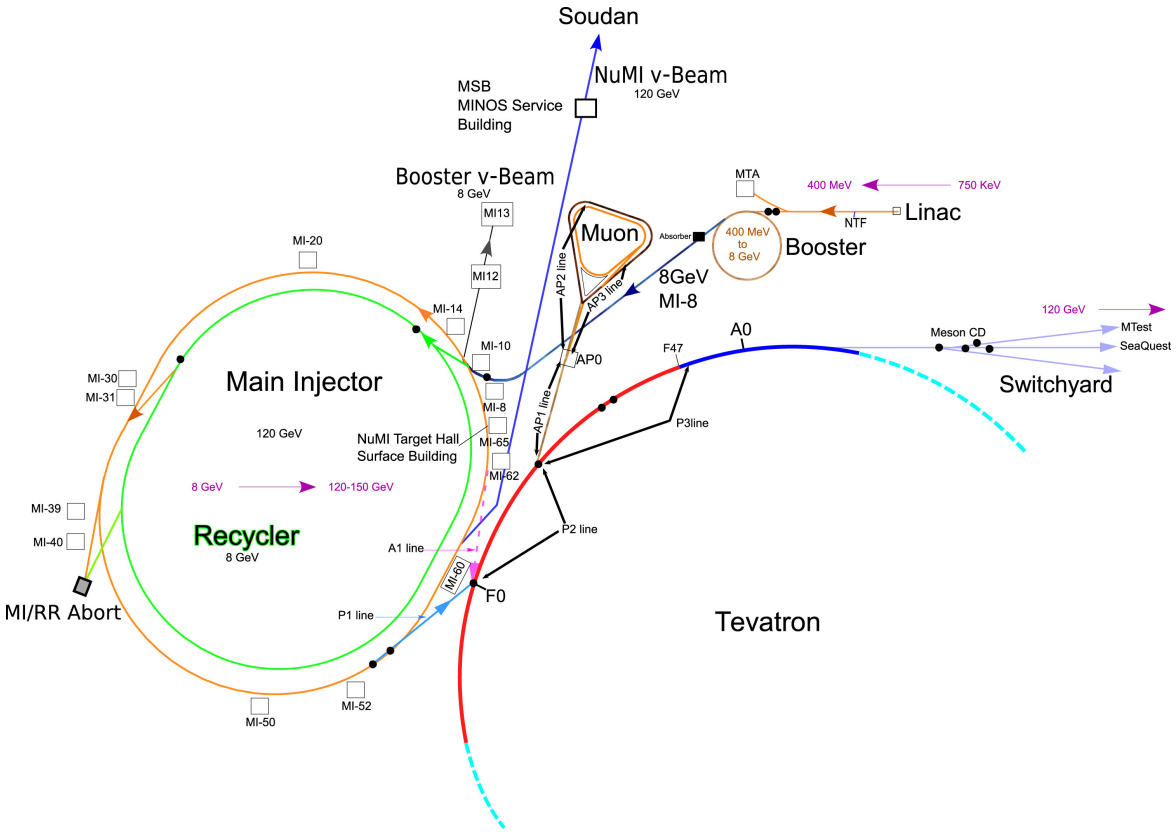

Figure 3.3: The Fermilab accelerator complex, showing at the top right corner the Linac Line, that follows to the Booster and goes to the Main Injector. The neutrino beam can be seen in the blue line called "Soudan" which is where the MINOS FD was located [56].

Before the MINOS experiment was completed, the process began in a Cockcroft-Walton accelerator, but nowadays it operates with a RF quadrupole [56], where negative hydrogen ions (H^-) are extracted from a plasma inside the dome of the accelerator and then travel through an evacuated cylinder to energies of 750 keV. Afterwards, they are led into the linear accelerator (Linac) where they accelerate until energies of 400 MeV are reached, the beam is then guided towards the Booster, a 150-meter diameter synchrotron. The hydrogen ions pass through a thin carbon foil, removing their electrons and converting them into protons [61] and being accelerated to energies of 8 GeV as 1.6 μs long batches with a bunch spacing of 53 MHz [56]. Finally, the beam follows to the Main Injector where it goes to energies of 120 GeV, delivering 5×10^{13} protons to the target at 10 μs pulses [19].

3.2.2 The target hall

Once the protons are produced, the next step is for the beam to hit a target located at the target hall. It is a cavern prepared to withstand heat, radiation and other hazards that may damage equipment and that has the modules that will be used for the baffle, target and the horns.

The first factor to take into account is the mis-steering of the beam, a few batches of these high energy particles could be enough to damage the sensitive components found on the target or the horns. For the protection of these, a large structure is made to degrade the particles from the mis-steered pulse, protect the components and, by a short time, not be damaged by the particles until the beam is shut off [56]. Such structure is called the baffle, being 150 *cm* long, with a 11 *mm* diameter hole, a 57 *mm* diameter graphite core on its inside and a 61 *mm* diameter aluminum casing as can be seen in Figure 3.4 [62].

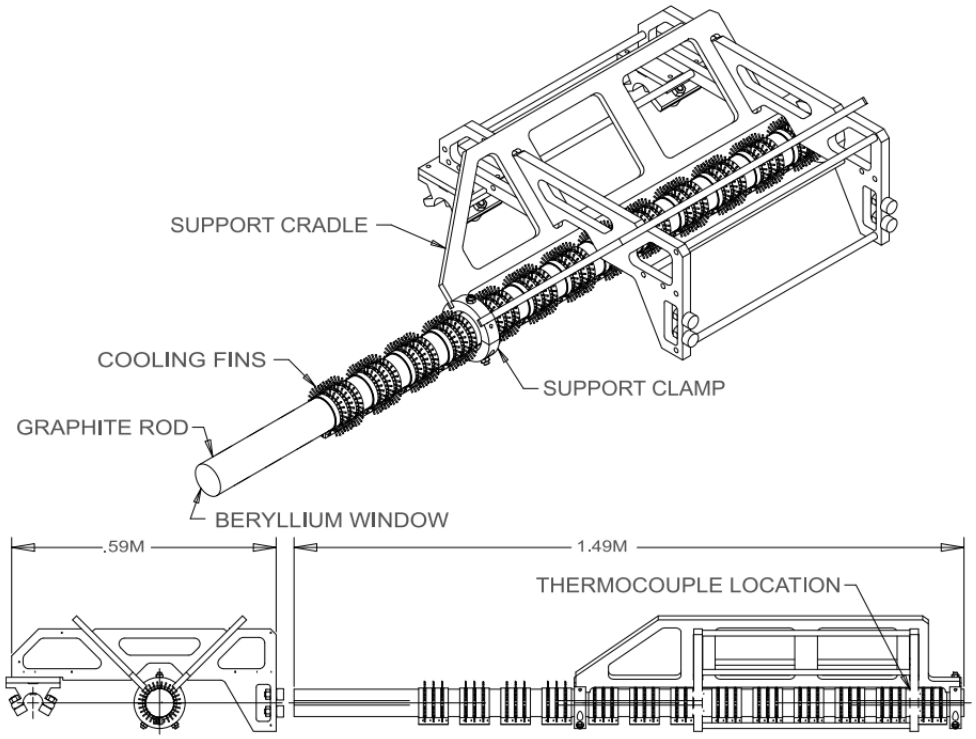

Figure 3.4: A schematic of the NuMI baffle, showing the graphite rod, beryllium window, cooling fins, support crandle and thermocouble location [56].

The beam of protons, once past the baffle, hits the target to produce pions, which will decay leading to the production of neutrinos and a charged particle such as a muon. The target material is a ZXF-5Q (POCO) graphite with a density equal to 1.78 g/cm^3.

The segments are machined and mounted to stainless steel water-cooling pipes. The main target is 47 vertical target segments, each one with 20.0 *mm* long, and with 0.3 *mm* spacing between them, giving a total length of 95.38 *cm*, which can be seen at Figure 3.5 [62].

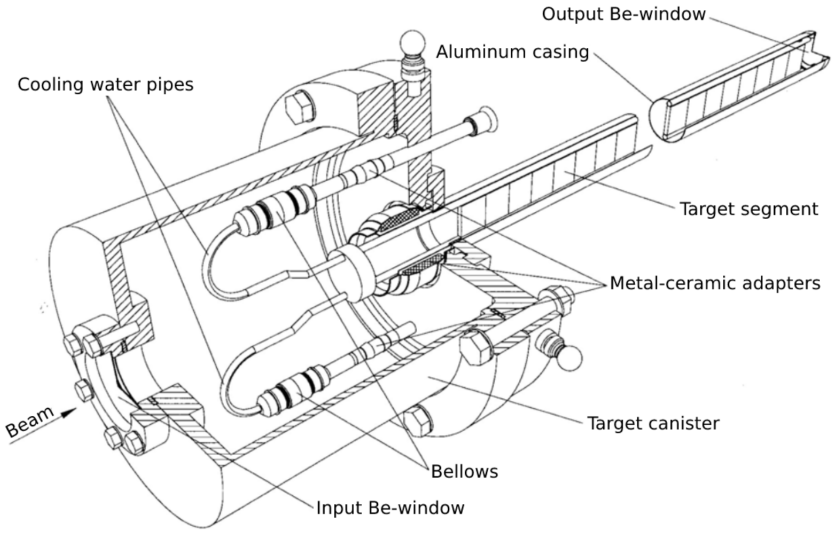

Figure 3.5: A schematic of the NuMI graphite target [62].

Once the protons hit the graphite target, mesons will be produced, mainly charged pions (π^+/π^-) with 84.5% of the composition and charged kaons (K^+) with 12.53% [63, 64]. The produced beam of meson particles is then focused by structures called horns, which will apply a magnetic field to the beam and, afterwards, they will pass through a decay pipe for the production of the neutrinos, as shown in Figure 3.6.

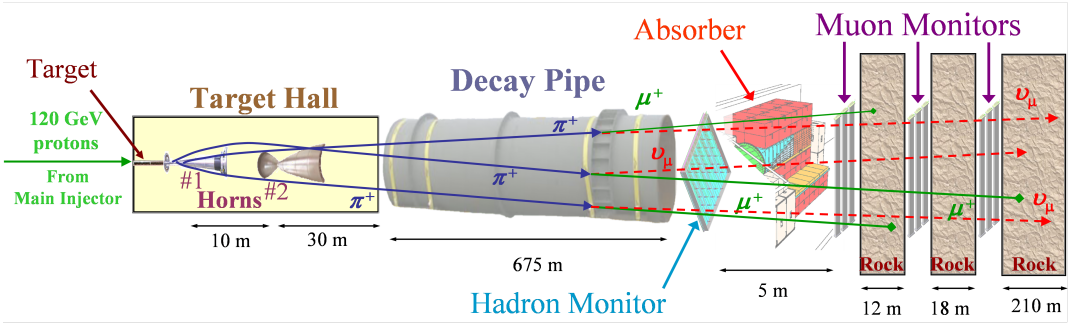

Figure 3.6: An illustration showing the path after the protons are made from the Main Injector, hitting the target that leads to the horns, afterwards going to the decay pipe, absorber and muon monitors [64].

3.2.3 Horns and decay

After the mesons are made from the protons hitting the target, they must be focused by a pair of horns, this process allows to calibrate for the desired energy range of the particles. That can be achieved by changing their position as Figure 3.7 shows:

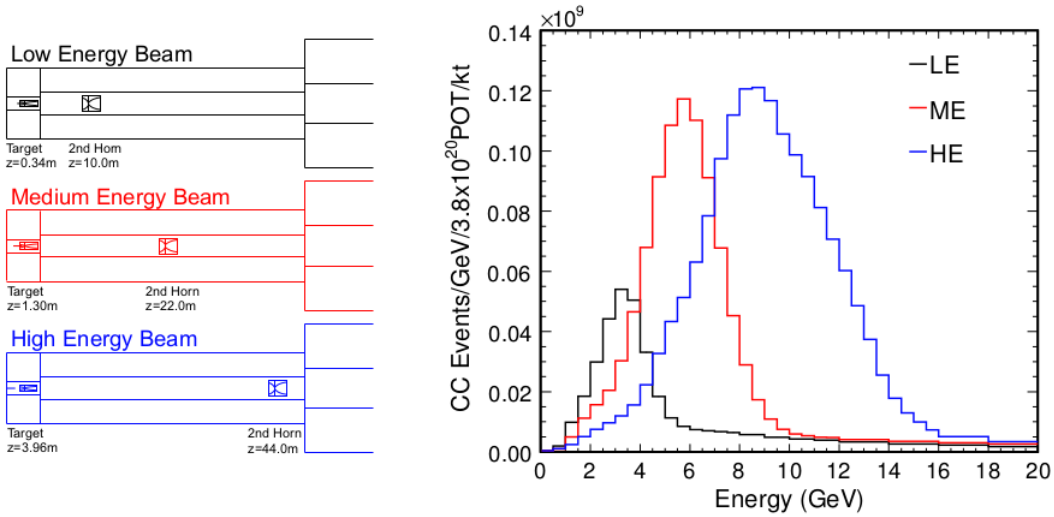

Figure 3.7: The distance of the horns can be seen in the left, and its impact on the ν_μ energy spectra on the right [65].

For instance, the Lower Energy is more interesting for the MINOS experiment, given that its energy range is close to the peak of the events. Meanwhile, the High Energy can be used for MINOS+ [36].

Both horns work with a pulsed half-sine wave that lasts 2.3 *ms*, this produces a magnetic field that can go up to 3 T. The maximum current can go to 205 kA with a repetition rate of 1.87 s. The current that flows through the horns can be reversed by reversing the power supply, this can select which meson will be focused, that is, deciding if it is preferable to have an antineutrino-enhanced beam (RHC) or a neutrino-enhanced beam (FHC). This can be seen in detail in Figures 3.8a and 3.8b [19, 56].

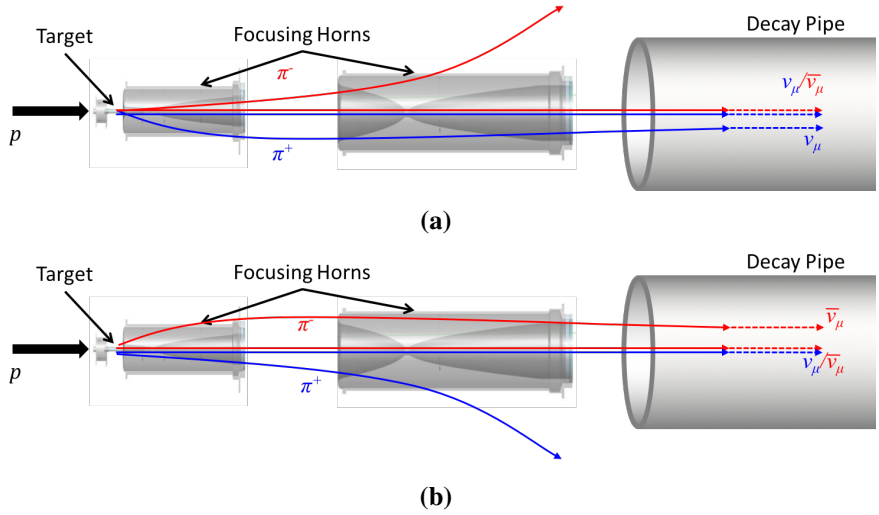

Figure 3.8: (a) The focusing horns being on the FHC mode, which focus the π^+ meson leading to the production of ν_μ. (b) The focusing horns on the RHC mode, focusing the π^- and enhancing the production of $\bar{\nu}_\mu$ [66]. The same process is analogous for the Kaons.

However, as it can be seen by Figure 3.8, the RHC and FHC modes do have some contamination that arises from the decay of other particles (such as μ^-). The neutrino enhanced beam will be constituted by 91.7% of ν_μ and 7.0% of $\bar{\nu}_\mu$ and 1.3% of $\nu_e + \bar{\nu}_e$. If the beam is enhanced for antineutrinos, than it is expected a presence of 40% $\bar{\nu}_\mu$, 58% ν_μ and 2% of $\nu_e + \bar{\nu}_e$ [36].

The mesons are then focused and will follow to the decay pipe where they decay into a charged muon and a respective neutrino or antineutrino, as shown by Eqs. (3.1), (3.2) and

(3.3) for the most contributing particles [63]:

$$\pi^+ \rightarrow \mu^+ + \nu_\mu, \tag{3.1}$$

$$\pi^- \rightarrow \mu^- + \bar{\nu}_\mu, \tag{3.2}$$

$$K^+ \rightarrow \mu^+ + \nu_\mu, \tag{3.3}$$

3.2.4 Absorber and monitors

Finally, after the decay pipe, there is a hadron detector for any remaining protons, kaons and pions that may still be present [36]. According to the NuMI beam simulations, about 80% of the particles that will interact are protons from the beam that has not interacted with the remainder composed of majorly mesons [56].

Afterwards, there is an absorber, composed of aluminium, steel and concrete for all the remaining hadrons [65]. The presence of the absorber is not just to remove the hadrons, some of the other functions goes as follows: the energy of the hadrons is converted into heat, by ionization, and it is used to circulate water in the thermal conduction. The absorber also limits the amount of radiation present in the tunnels, this allow for personnel to enter some acessible regions. Another reason for its presence is to limit the residual radiation for those who will acess its hall under beam-off conditions [56].

After the beam pass through the absorber, it will encounter the muon shielding, which is the 240 m of solid dolomite rock. Without their presence, MINOS would suffer from interactions of the products of particle decay near the ND electronics, overloading the pattern recognition [56]. Between the shielding, there are the muon monitors, which signals the presence of muons and hadrons to verify the NuMI beam condition and the efficiency of the horns [36].

3.3 The MINOS/MINOS+ detectors

The MINOS and MINOS+ experiments uses the same detectors composed of steel-scintillator sampling calorimeters which are capable of making measurements of the energy and topology of neutrinos [67]. Both the ND and FD are designed as similar as possible to minimize the systematic errors that will result from the comparison of neutrino spectra, they are both separated by a baseline of 735 *km*, the ND being located at Fermilab, while the FD is located in Soudan [54, 68].

Both detectors work by having a layer of steel that acts as the neutrino target and calorimeter, also serving as the material with the best magnetic permeability and good tensile strength. The neutrinos can interact with the steel plates generating secondary particles. These new particles follow to a layer of plastic scintillator which generate light that are detected by the electronic part and, afterwards, processed for reconstruction of events. Both detectors are also magnetized, allowing for charge discrimination and momentum determination [36, 54].

3.3.1 The Near Detector

The Near Detector has a primarily function of serving as a reference for the Far Detector [69]. Being located 1.04 *km* from the target and about 90 *m* under the surface, weighing a total of 980 *tons* and having a length of 16.6 *m* [44, 53]. In Figure 3.9 we can see a schematic and a picture of the detector.

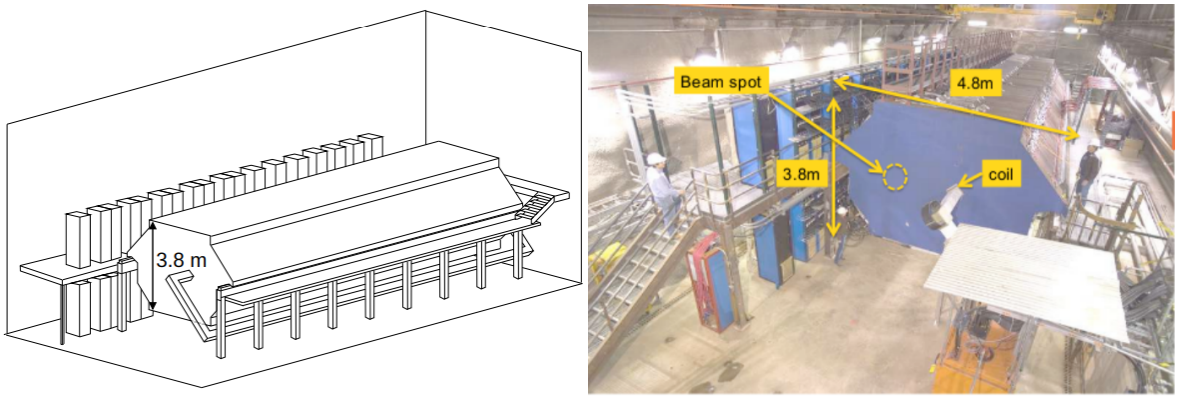

(a) **(b)**

Figure 3.9: (a) Schematic of the MINOS Near Detector [70]. (b) Picture taken from the MINOS ND [36].

It has 282 planes, from which 153 are instrumental and is divided in two regions. The upstream region has 120 planes and all are instrumented. While the downstream region (the spectometer section) has 162 planes with only one being instrumented every 5 planes, this is so the detector can show the presence of trajectories and interactions off the region of the beam [36, 54].

The ND has a geometry of 3.8 *m* high and 4.8 *m* wide with an octogon cross section, this geometry was choosen to minimize the amount of steel used while providing enough plane area with a magnetic field for the neutrino interaction region. The detector is also positioned so that the neutrino beam is 1 *m* away from the coil hole [54, 69].

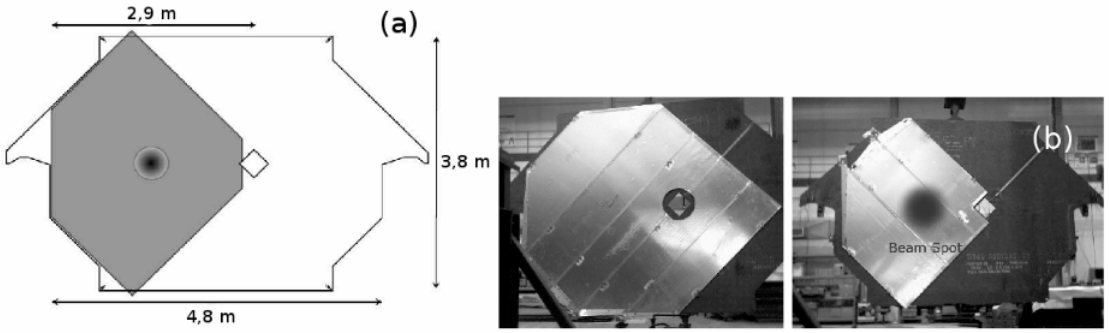

Figure 3.10: (a) A front view (XY plane) of the ND. The grey area shows the extent of the scintillator modules, while the black line that makes the area around it is the extent of the steel planes. The dark circle represents the diameter beam spot, and the diamond shape the magnetic coil hole. (b) In the left it is showed a fully instrumentalized section and in the right a parcial one [36, 71].

In its longitudinal dimension, the detector has four other regions with functionally different components. They are as follow:

Veto Part: The upstream part of the detector, the neutrino interactions here are not used because of the need to assure that there is no background and no end effect. It assures no anomalous effects in the target region [36, 69];

Target Part: The interactions of neutrinos that happens in this part are the one used in the comparison with the FD. It uses the plane section 21 to 60;

Hadron Shower Part: Using the 61 to 120 planes sections it has the function of detecting any electromagnetic or hadronic showers;

Muons Spectrometer Part: Located in the region of the 161 remaining planes, it is used to range out muons and/or measure their momentum by curvature.

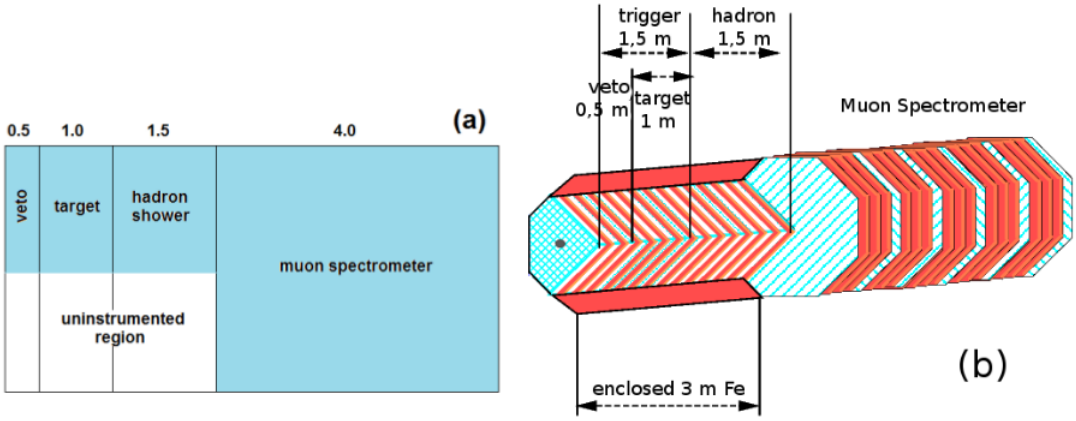

Figure 3.11: (a) The four regions of the Near Detector, the uninstrumented region has scintillator at each 5 planes. (b) Instrumented regions of the ND being seen in terms of the steel plates, it does not represent the whole width of the detector [71].

3.3.2 The Far Detector

The Far Detector is a structure located in the Soudan Underground Laboratory in the northern of Minnesota in the seventh floor of the Soudan inactive iron mine. It is 713 *m* underground, being 30 *m* long, 8 *m* wide and 8 *m* high, having a total mass of 5400 *tons* [36, 72].

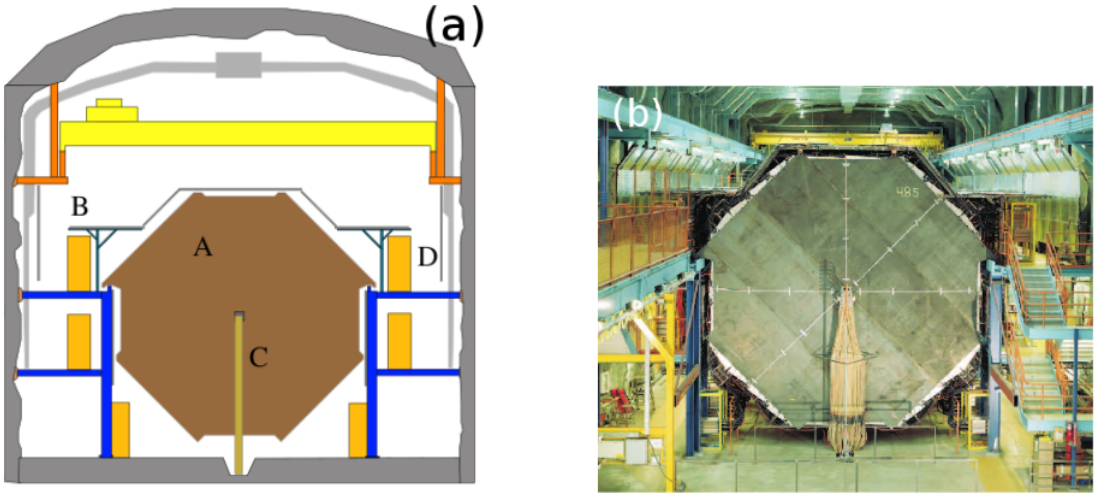

Figure 3.12: (a) Schematic of the Far Detector and its regions, denoted as (A):The frontal view of the octagon plane structure; (B): the veto shielding; (C): The magnetic coil in the center; (D): The electronical devices. (b) A picture of the FD [36, 72].

Its structure is composed of 486 planes, the planes, or basic modules, have 8 *m* in diameter and 2.54 *cm* of a thick steel plane that has, afterwards, the scintillator plate. The detector has two supermodules [69] to minimize the effect of thermal expansion. One of the supermodules is comprised of 249 basic modules while the other has 237 planes with an air gap of 1.1 *m* between them both where the magnetic coil is installed [73].

The major function of the FD is to collect neutrino events from the NuMI beam. It is expected that each day the cosmic event rate is of approximately 0.5 Hz [74]. The detector planes in the supermodules are separeted by 5.95 *cm* and vertically aligned to maximize the data from the interaction of the neutrino beam.

Both the detectors are comprised of the steel and the 4 *cm* wide scintillator strips. The planes are oriented at a 90° between themselves and 45° angle with respect to the vertical axis [63], defining a coordinate system referred as the U and V directions, that have the following relation with cartesian coordinates:

$$U = \frac{\sqrt{2}}{2}(y+x), \tag{3.4}$$

$$V = \frac{\sqrt{2}}{2}(y - x), \tag{3.5}$$

meanwhile, the scintillator plates follow the same orientation, but sucessive plates are orthogonal alternated. If a particle hits at least two planes, one U and one V plane, it is possible to determine its vertical and horizontal position, while its depth is known by how many planes it penetrated. With these informations, it is possible to reconstruct the events in 3D space [72].

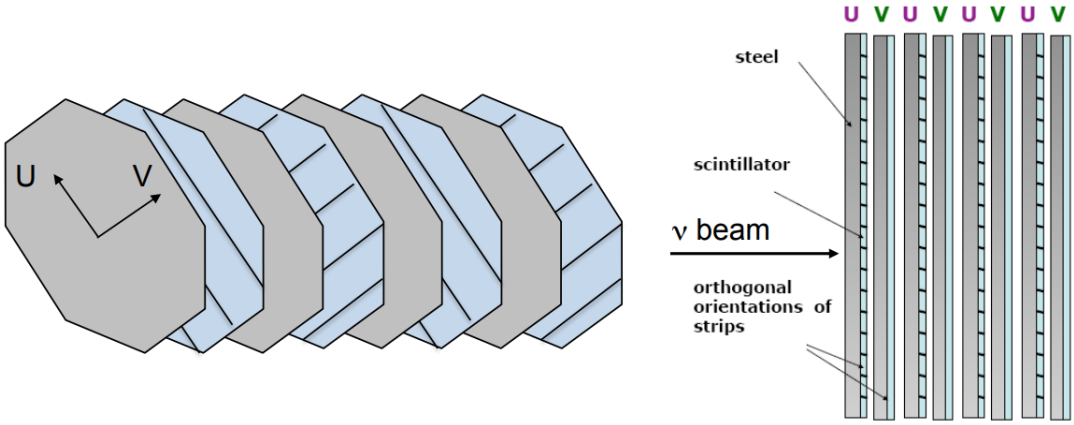

Figure 3.13: Arrangement of the MINOS planes in the detectors. As cited prior, the sucessive planes have orthogonal alternating scintillator strips [63].

The FD also can detect a cosmic muon event, which can be useful as data for atmospheric neutrinos, or can be a background for the NuMI beam events. The way the FD makes this detection is through the *veto shield* which is placed in four overlapping sections in the Z-axis. The first two sections are located above the first supermodule and the third and fourth above the second one. The shieldind is made out of the same scintillator modules that compose the planes of the detectors [72].

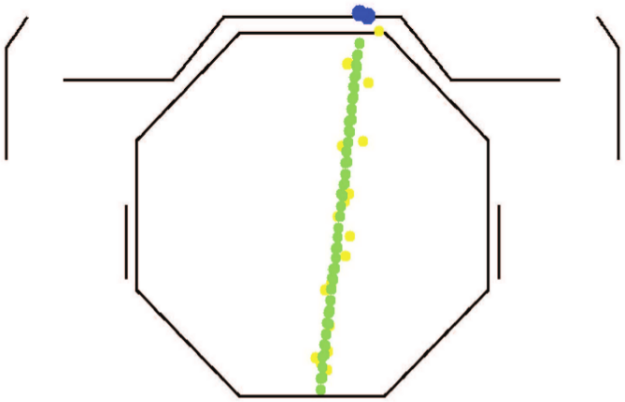

Figure 3.14: Example of a cosmic ray event being detected by the *veto shield* in the FD. The blue points indicate activity in the *veto shield*, the yellow poins represent hits with a deposition of charge lower the two photo-electrons and the green points are hits with a depoisition of charge higher than two photo-electrons [72].

3.3.3 The magnetic field

Both detectors have a magnet system, the ideia of such is for allowing to measure the muon momenta in a resolution of $\sigma_p/p \approx 12\%$ if the energy exceeds 2 GeV. If the experiment is in the ν_μ mode, the muons that will be produced by the interaction of the neutrino can have their trajectorie changed towards the center of the detector and, in the case of the $\bar{\nu}_\mu$ mode, the field can be switched so that the antimuons have the same behaviour, allowing for a more precise measurment of the momentum [36, 63].

However, the magnetic coil in each detector have different designs given the different requirement that the geometry apply on them.

The Near Detector coil, for instance, is in an offset of 55.8 cm from the center of the plane. Given the squashed-octagon geometry, it consists of 48 aluminum conductors arranged as Figure 3.15 shows:

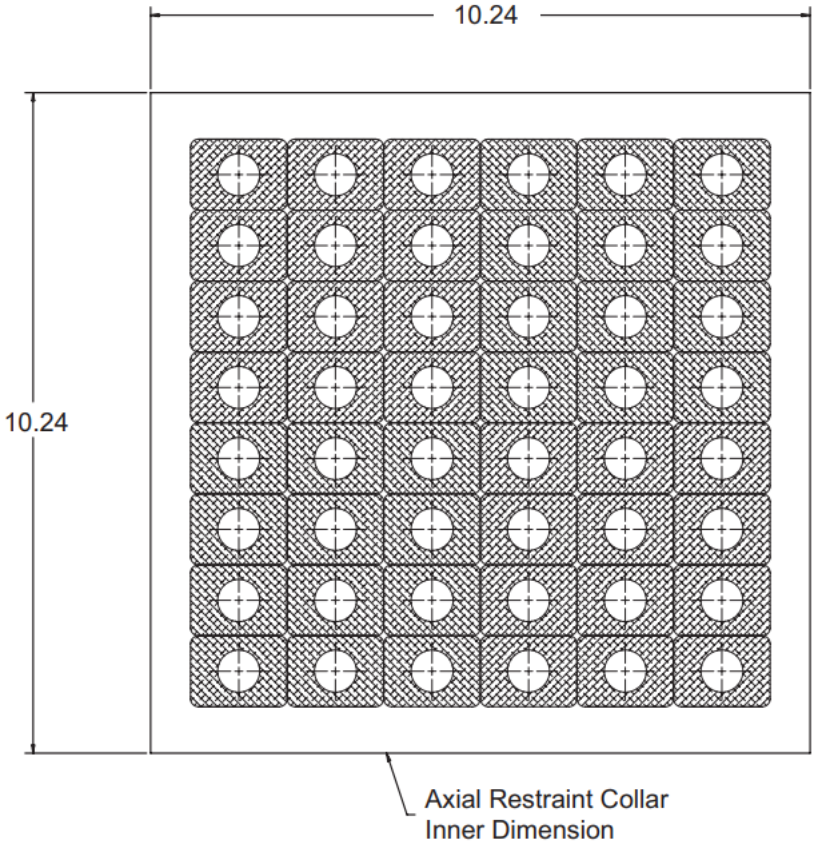

Figure 3.15: Cross section of the ND coil, the dimensions are in inches [68].

For each row of six conductors, there is a current of 5 *kA*, making up for a total of 40 *kA*-turn. The coil dissipates about 47 *kW* and it is cooled by a closed-loop low-conductivity water (LCW) [63, 68].

The coil of the ND goes through the detector and returns close to the uninstrumented region, this way, the magnetic field wont cause interference with the electronical devices [36].

Meanwhile, the Far Detector uses two coils, one for each supermodule. Each one have 190 turns of copper wire that carries a current of 80 *A* for a total of 15.2 *kA*. It dissipates 20 *kW* and it is water-cooled by 15 copper tubes, being distributed in the cross section, as can be seen in Figure 3.16:

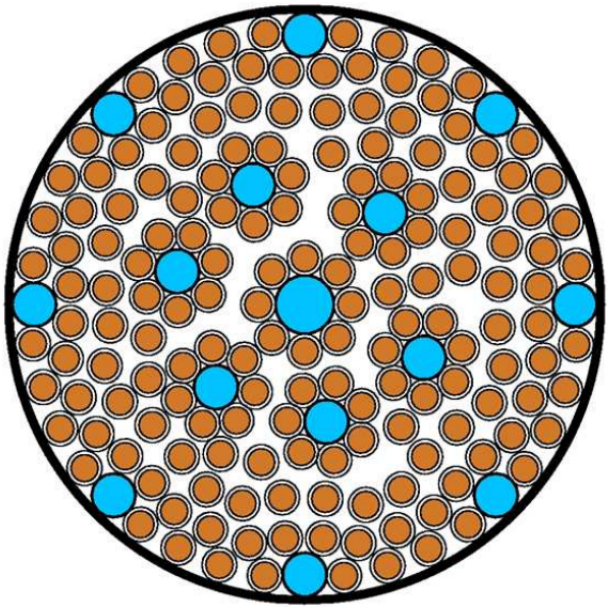

Figure 3.16: Cross section of the FD coil [63].

The magnetic fields are determined using finite element analysis (FEA) for both detectors; this analysis is performed using the ANSYS program. In Figure 3.17 we can see the different field maps generated in the ND and FD [68] and its direction (in the FD) can be seen in Figure 3.18:

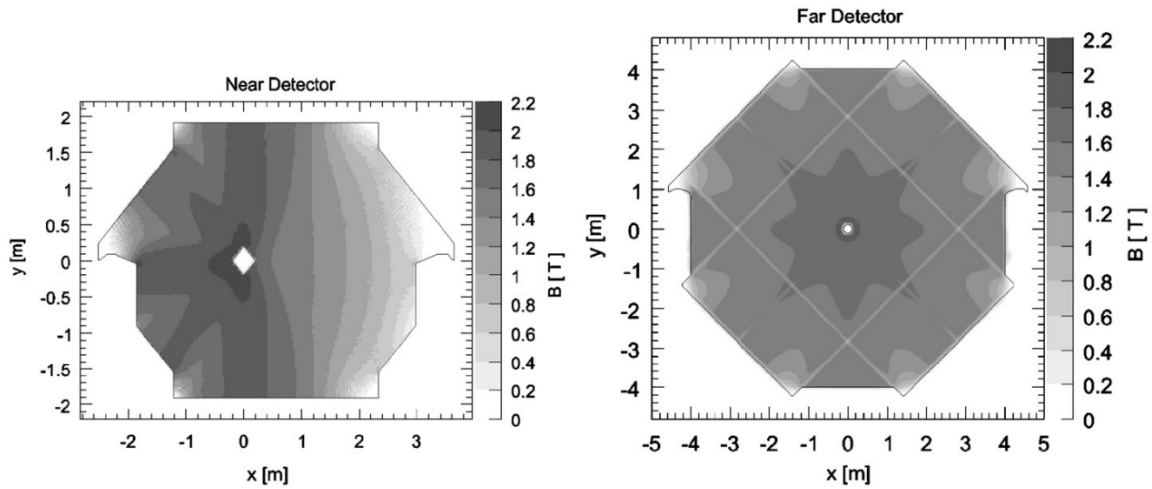

Figure 3.17: Magnetic field maps for the ND and FD detector plane. The greyscale indicates the field strength B [68].

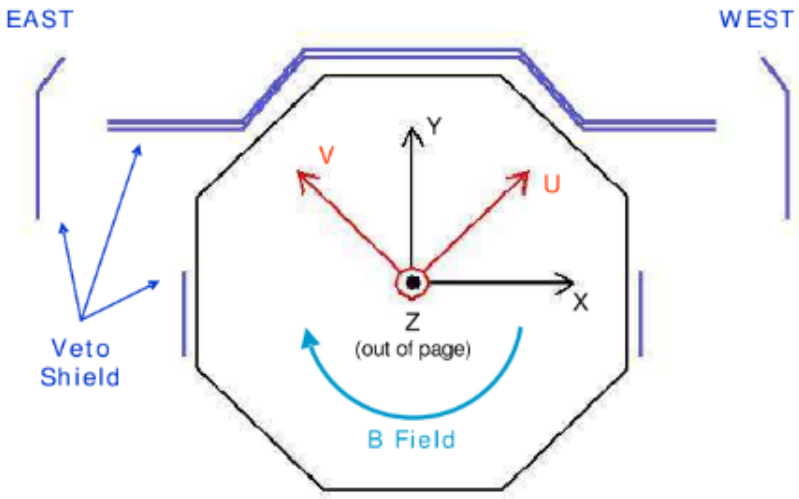

Figure 3.18: Representation of the FD coordinate system with the orientation of the *B* field [71].

3.3.4 The scintillator strips

The scintillator strips are one of the components and the core of the MINOS detectors particle detection system. They are 1 *cm* thick, 4.1 *cm* wide and between 2.5 - 8 *m* long.

The strips consists of a clear extrused polystyrene core and a polystyrene cap that is coextruded. The cap has a 0.25 *mm* thick layer of TiO_2 (titanium oxide), this enrichment is made with 15% by weight. The presence of the oxide works as a diffuse reflector for the scintillation light. The cap is also opaque for ultraviolet light, optically isolating each strip from the others.

The plastic is also doped with 1.03% scintillating fluors (this measure is by weight), 1% of PPO (2, 5 - diphenyloxazole) and 0.03% of POPOP (1,4-bis(5-phenyloxazol-2-yl)benzene) fluors. Once a particle passes through the core, these molecules are excited and emit a photon [63, 68].

A groove is also cut in the top of the stip, being a 2.3 *mm* deep by a 2.0 *mm* wide. It is free of the TiO_2 and, glued to this groove, is the wavelenght shifting (WLS) fiber that is covered

with a refletvie strip of aluminized Mylar tape. The fiber is 1.20 *mm* diameter containing 175 *ppm* of Y-11.

The fiber absorbs light that is peaked in 420 *nm*, which is reimitted isotropically at 470 *nm*. This light is carried to the phototubes. The fibers are then putted into a module, a light-tight aluminium case [54, 63, 68]. A representation of the fiber can be seen in Figure 3.19 and the module manifold assembly in Figure 3.20.

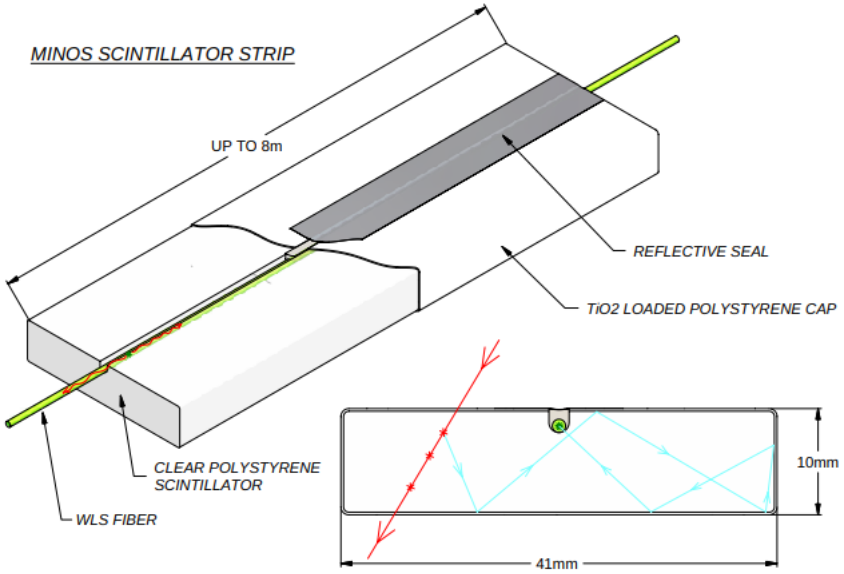

Figure 3.19: Representation of a scintillator strip. In the cross-sectional view, it can be seen an ionizing particle (red) produces light (blue) which is reflected by the TiO_2 cap until the WLS fiber absorbs it and the reemitted light is then transported to the edges of the detector [63].

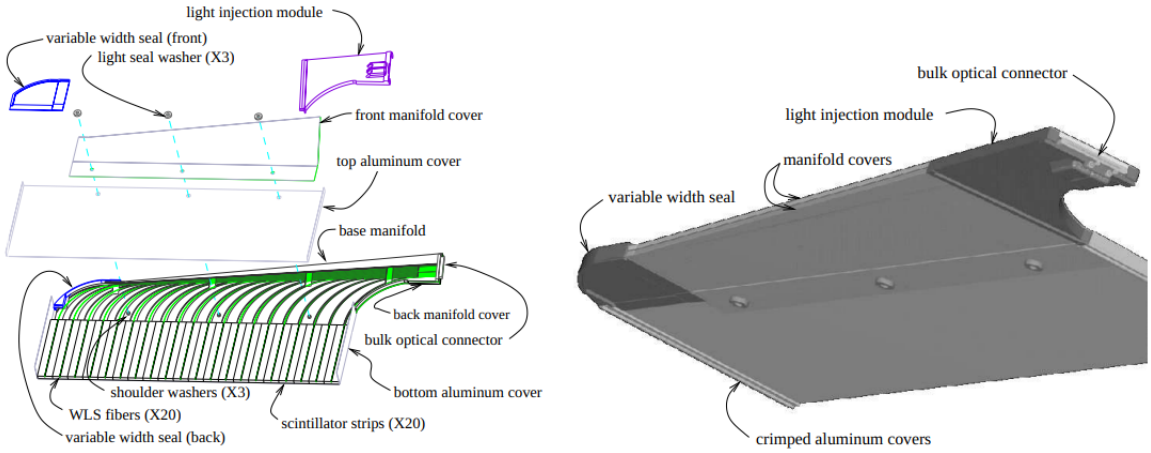

Figure 3.20: In the left: a MINOS module manifold assembly, where the WLS fibers are routed to bulk optical connectors. In the right: the same module, but enclosed with aluminium covers [68].

In the FD the boards of the scintillating strips are already connected to the photo multiplier tube (PMT). Meanwhile, in the ND, only one board is connected. When the signal is read they must be summed up so the global value of the strip can be found. The scintillating strips are organized in different batches of 16 to 24 strips called modules, being easier to be moved. There is a total of 22 different modules in both the ND and FD, as can be seen in Figures 3.21 and 3.22 [36].

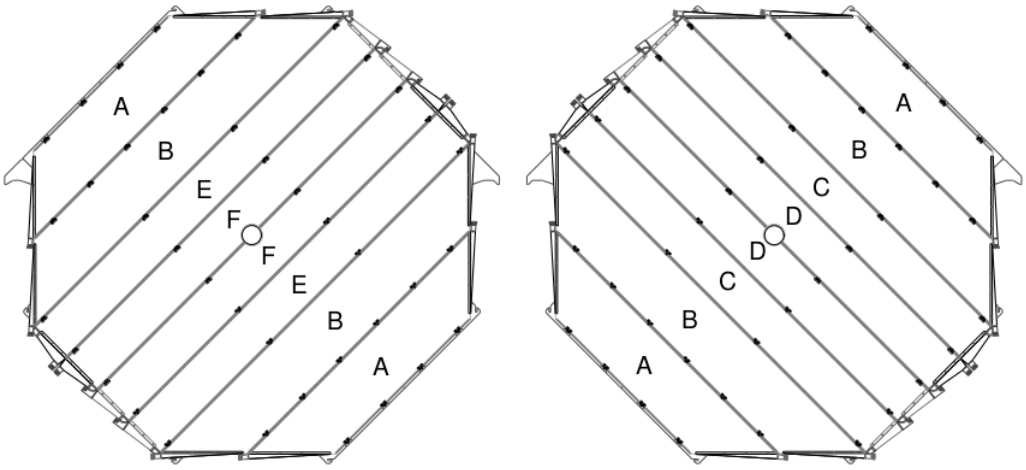

Figure 3.21: Layout of the modules in the FD, U planes in the left and V planes in the right. The modules with the letters A and B have 24 scintillating strips, while the others have only 20 [36].

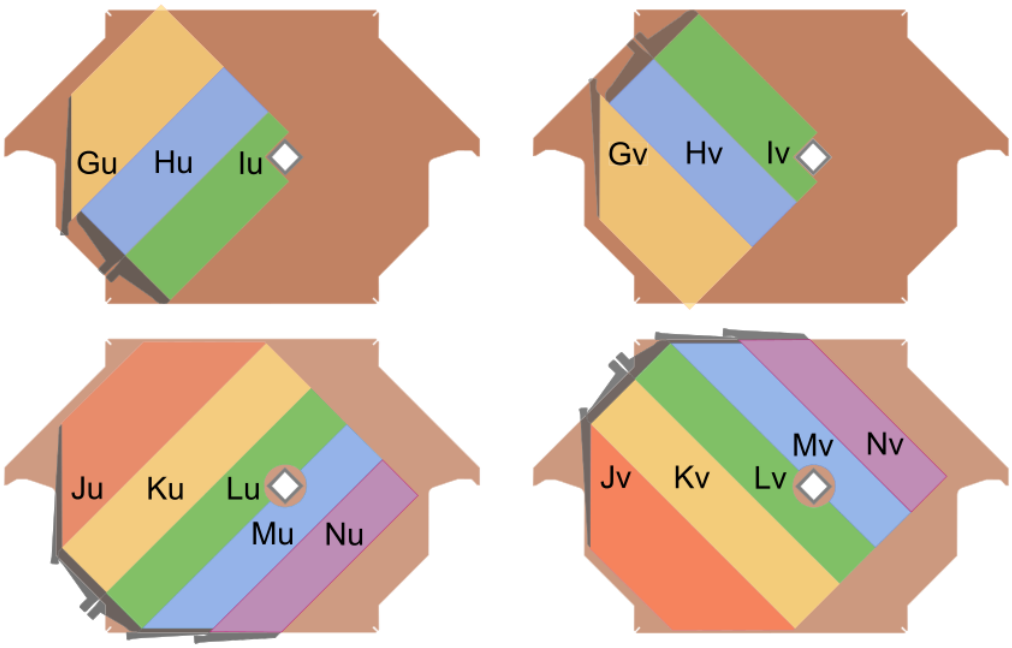

Figure 3.22: Layout of the modules in the ND. In the top left we have a U plane partially instrumentalized (PU) and in the top right a V plane partially instrumentalized (PV). In the bottom left we have a fully instrumentalized U plane (FU) and in the bottom right a fully instrumentalized V plane (FV). Planes in the calorimeter section follows the same repeating pattern: FU-PV-PU-PV-PU-FV-PU-PV-PU-PV. The spectometer part also follows this pattern, but only every 5 planes. The different modules indicate different quantities of scintillating strips [36].

3.4 Data acquisition and processing

3.4.1 The photodetectors

The light that is reemited by the WLS is then guided by a cable of optical fibers to a PMT. They are housed in a steel enclosure from where small segments of optical fibers are connected to the pixels of the PMTs, as can be seen in Figure 3.23.

In the ND each enclosure will have a PMT Hamamatsu 64-anode (M64), having a total of 194 PMTs in the detector. Each stripe is connected to one of the pixel of the PMT, using a plastic part with a diamond-bit fly-cutter named “cookie” (this can be best seen in Figure 3.24). In the calorimeter part of the ND, each PMT is connected to an electrical

device that does the output reading. While in the spectometer sector, four PMTs are conected in parallel to one device and their signal is summed.

In the FD the enclosures (named the MUX box) has three PMT Hamamatsu 16-anode (M16), having a total of 1452 PMTs in all the detector housed in 484 MUX boxes. The *veto shielding* also has another 64 PMTs. In the FD, the connection to the pixel is made with eight strips, instead of one, like in the ND.

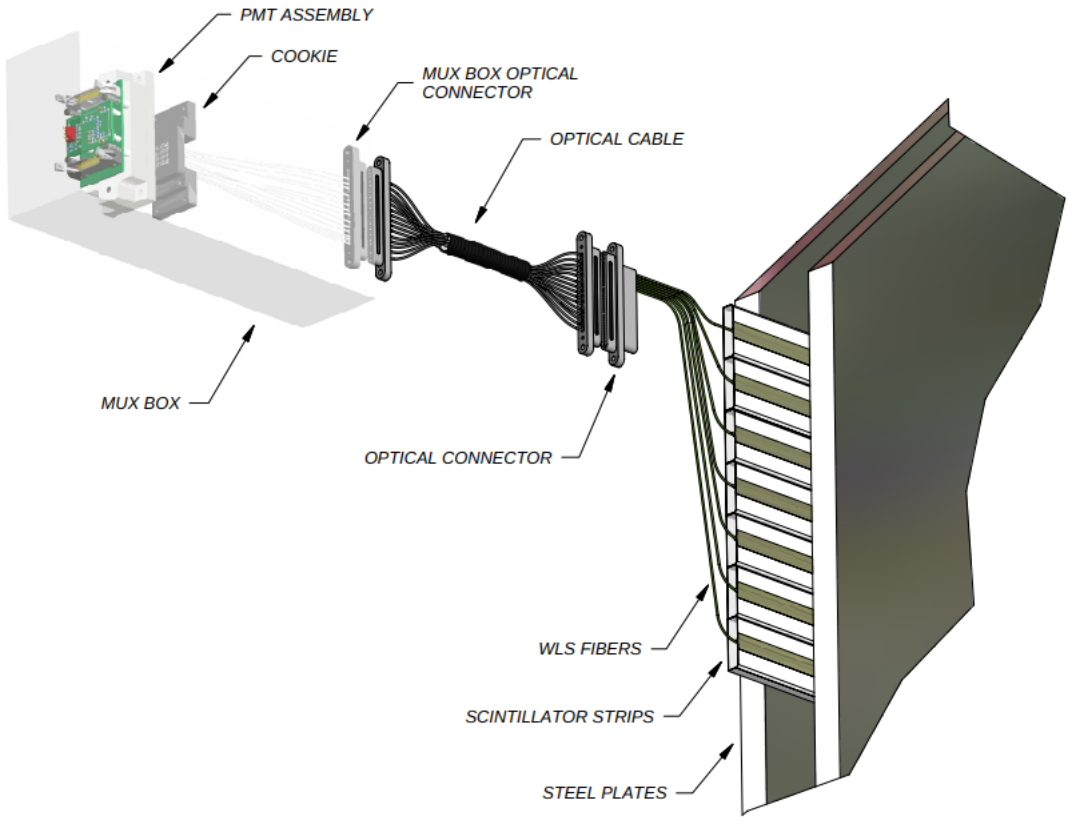

Figure 3.23: Schematic of the readout for the detectors. Once the scintillated light is made it is guided to the muti-anode photomultipliers via the optical fibers [63].

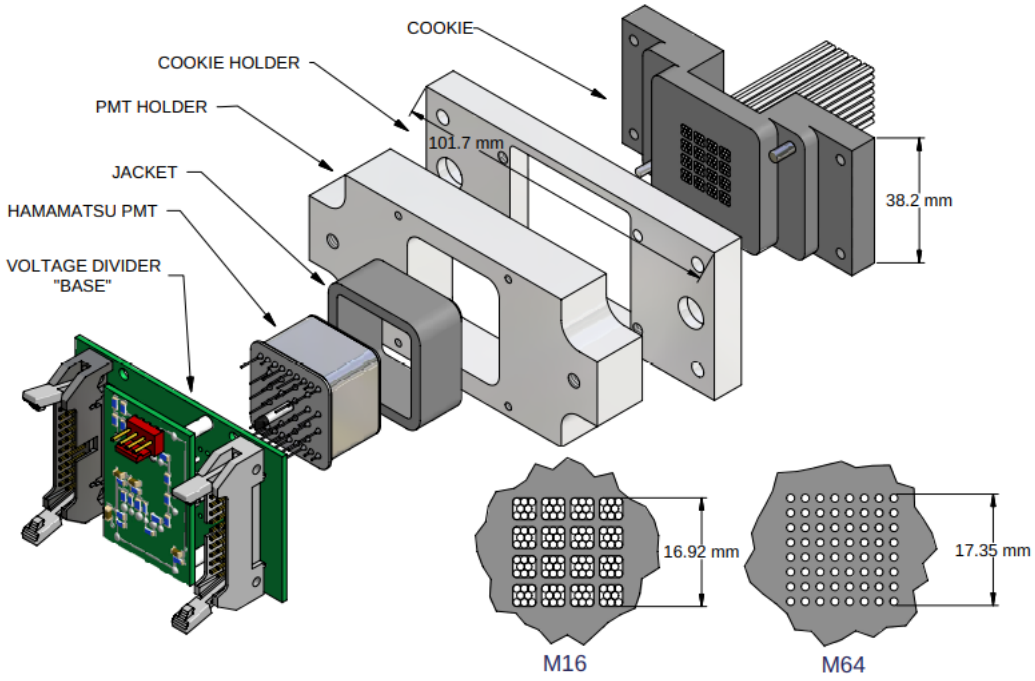

Figure 3.24: A schematic of the M16 PMT assembly. This is used to bring the fibers to the PMT pixel. In the FD eight strips are connected to one of the 16 pixels, while for ND one strip is connected to a 64 pixel [63].

The signals in the scintillating stripes are converted to photon-electrons (PE) in the PMT. A muon with a minimal energy to make ionization is capable of achieving a signal of 5 PE in a stripe. The minimum value to trigger the PMT is about $1/3$ of a PE [36, 63, 68].

3.4.2 The front-end electronics

After the signal reaches the PMT, it needs to be integrated, linearized, and digitized before being sent to the Data Acquisition System (DAQ). Who does all of this process is the front end electronics. However, the environment in which the detectors are impose a different set of requirements for the front end electronics [63]. Hence, lets begin by analysing the Far Detector.

In the FD each PMT is connected to a multi-channel integrated circuit, the Viking VA chip (VA chip). In the MUX box, there are three VA chips that are mounted into a front end board (VFB). These boards provide power, biasing controls and a ASDLite chip, which uses the PMT signal for triggering the digitalization if the signal is above 0.25 PE [74]. This setup can be seen in Figure 3.25.

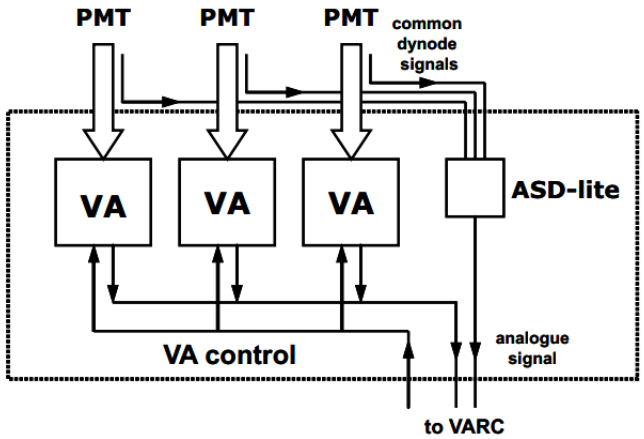

Figure 3.25: Schematic of the VA Front-End Boards [71].

The analogue signal of two VFBs are sent to a VA Readout Card (VARC) that is connected to a VME (Versa Module Europa) crate. The first step within the VARC is to convert the analogue signal to a digital one, this is done with a VMM (VA Mezzanine Module) and the one ADC (Analog-to-Digital Converter) inside the VARC. In the same chip, there is also a Event Time Controller (ETC) that direct the readout of the PMT to the VA chip. Each pair of VMM-ETC is connected to two VFBs (that have each 6 VA chips) [71]. This process can be seen in Figure 3.26.

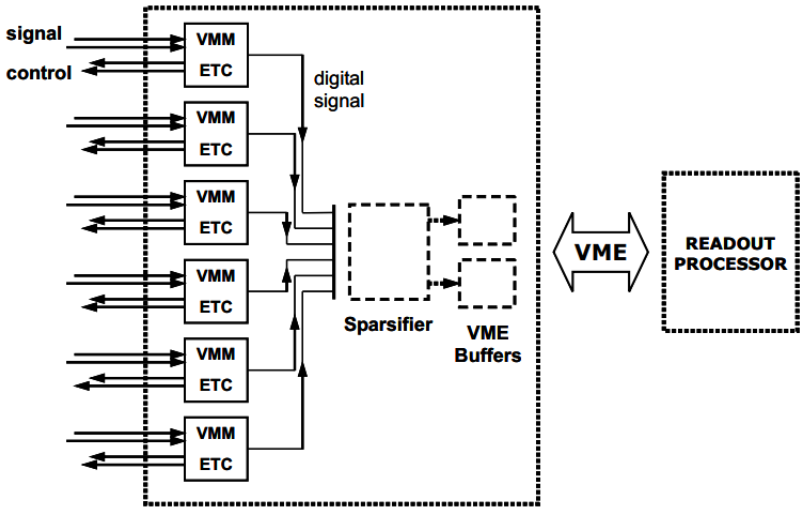

Figure 3.26: Schematic of the VA Readout Cards [71].

Each VARC handles 36 PMTs, however, it is needed a coincidence trigger for the readout to be actived. This trigger needs to happen in a window of 400 *ns* and requires 2 out of the 36 VA chips that are connected to the VARC. When this trigger is satisfied the ETC timestamps the trigger and directs the VA chips to read out the PMTs that have triggered. It is also important to say, that there is a dead time of 5 *ns* per VA chip in the FD [36, 71].

In the Near Detector the readout system must be different. The beam spill lasts up to 10 μs, being able to produce in the order of 10 neutrino events in the detector. Given the higher event rate in the ND the electronics needed to be fast and have no deadtime [65].

Each M64 pixel of the PMT in the ND is connected to a MENU (MINOS Electronics for Neutrinos) circuit board. It consists of a Charge Integration Enconder (QIE), a chip developed at Fermilab that allows for continuos dead time-less operation. The MENU board also has a commercial flash analog-to-digital converter (FADC) and a data buffer [63].

The signal from the PMT is fed into the QIE. The signal goes to a current splitter and the analogue signal is coverted to an eight bit signal by an ADC. The 8 bit is then increased to a 13 bit word given the addition of bits to encode the analysed range of the splitter and which ones were used. The word is then received by a 1000 word FIFO (First in, first out) buffer,

being large enough to all words in the 10 μs [65]. A picture and schematic of the MENU can be seen in Figure 3.27.

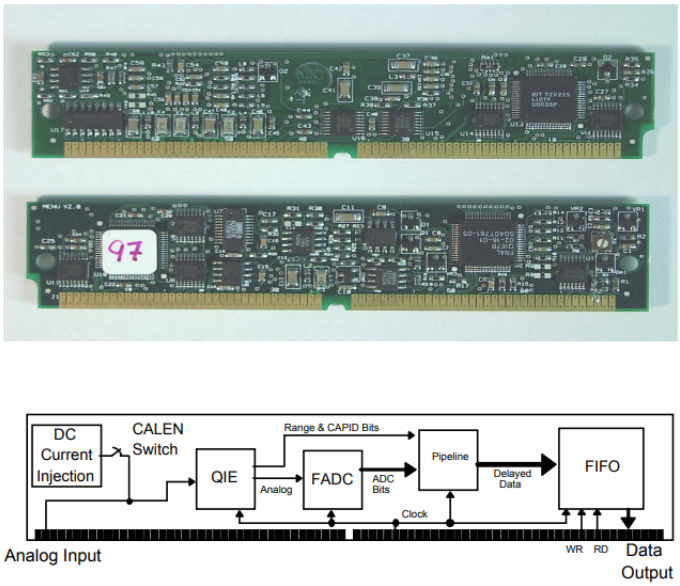

Figure 3.27: Schematic and picture of the MENU circuit board [75].

Sixteen of the MENU boards are then connected to another board called MINDER (MINOS Near Detector Electronic Readout) which can be seen in Figure 3.28. The MINDER time-stamps the signals and controls the modes of the MENUs. It also reads sequentially all the words from all its FIFOs sending it to a single FIFO that follows in the chain, the MASTER (MINOS Acquisition, Sparsifier and Time stamper for Event Redout) module. A picture of a MASTER can be seen in Figure 3.29.

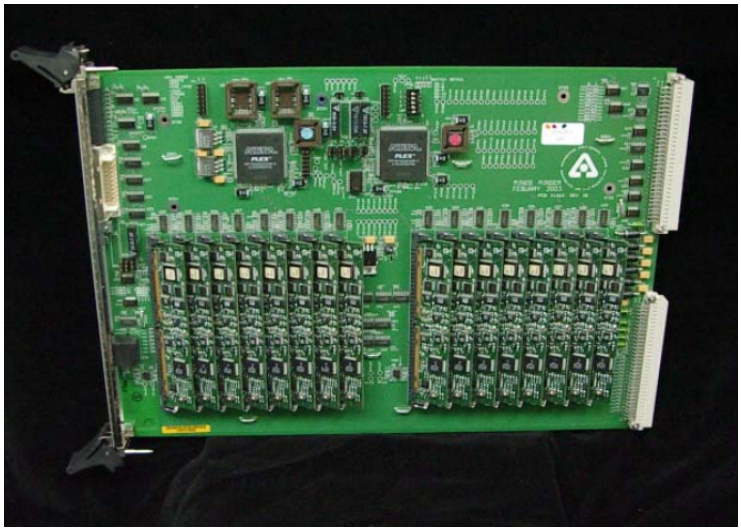

Figure 3.28: Picture of a MINDER board [75].

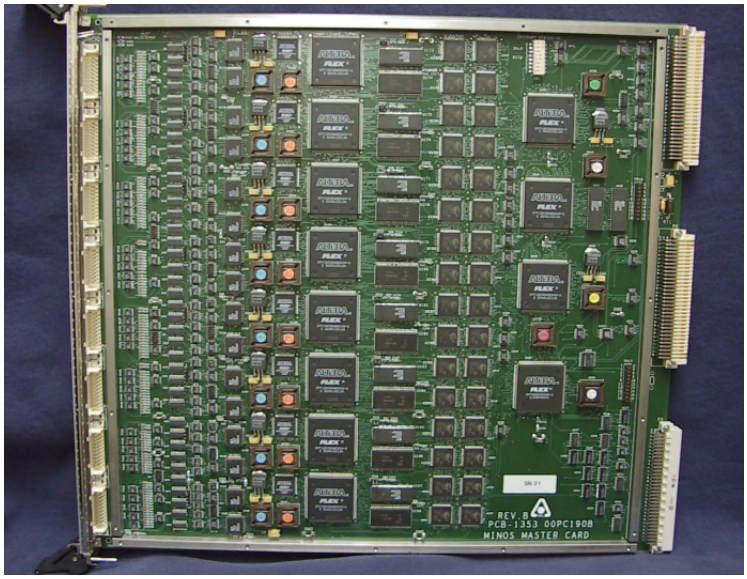

Figure 3.29: Picture of a MASTER board [75].

Eight of the MINDER boards are then connected to the a MASTER [36], it then reads the data from the MINDERs into two buffers that are read by a VME computer and, afterwards, is send to the DAQ [65]. An image of the whole readout system can be seen in Figure 3.30.

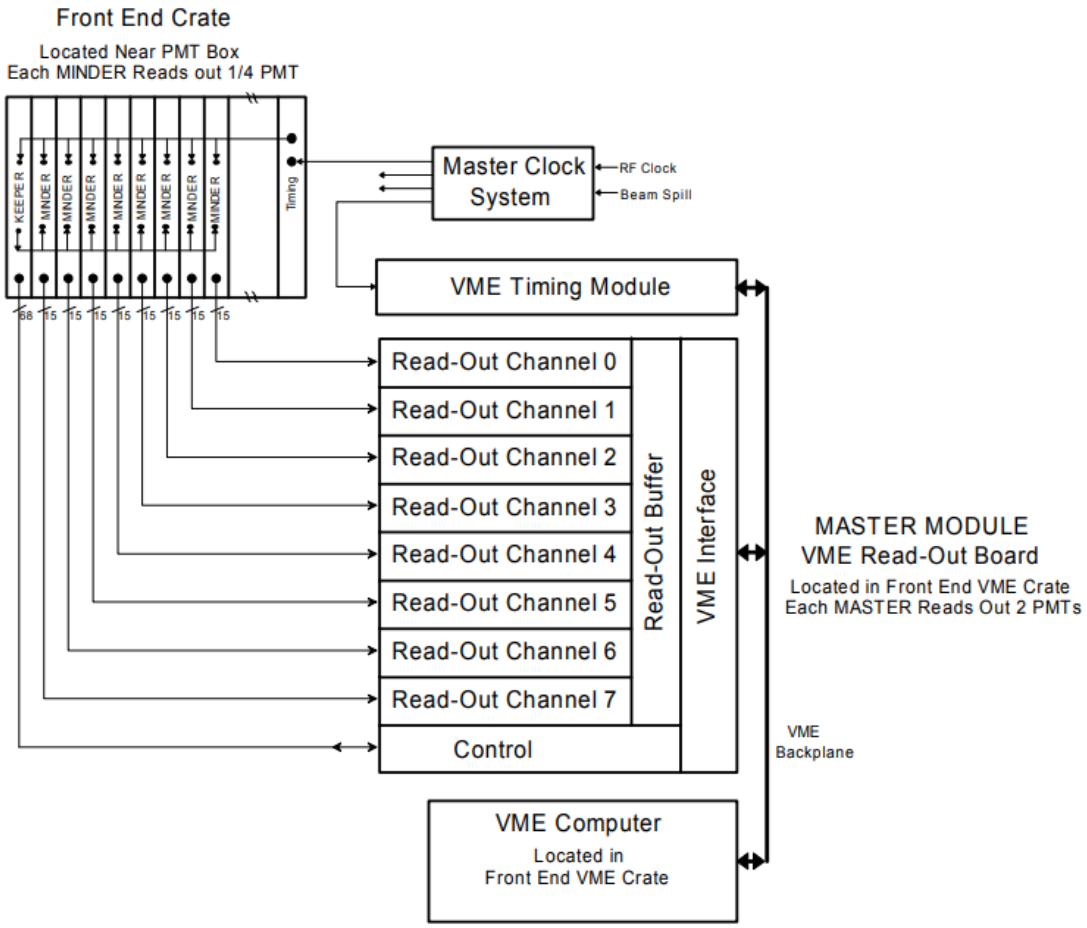

Figure 3.30: Block diagram of the readout system [75].

The data aquired from the beam do not experience any dead time, the cosmic rays do have a dead time in each PMT of about 0.5%. Which shows the effiency the reading process [36].

3.4.3 The DAQ

The DAQ or data aquisition system, both in the ND and FD are functionally identical. The only difference resides in the software to accommodate the different front end electronics in each detector. The objective of this system is to continuosly read out the electronics in a untriggered, dead-time manner and, also, to transfer this data do a farm of PCs that will select the events of interest and monitor calibration tasks. A schematic of the MINOS DAQ system can be seen in Figure 3.31.

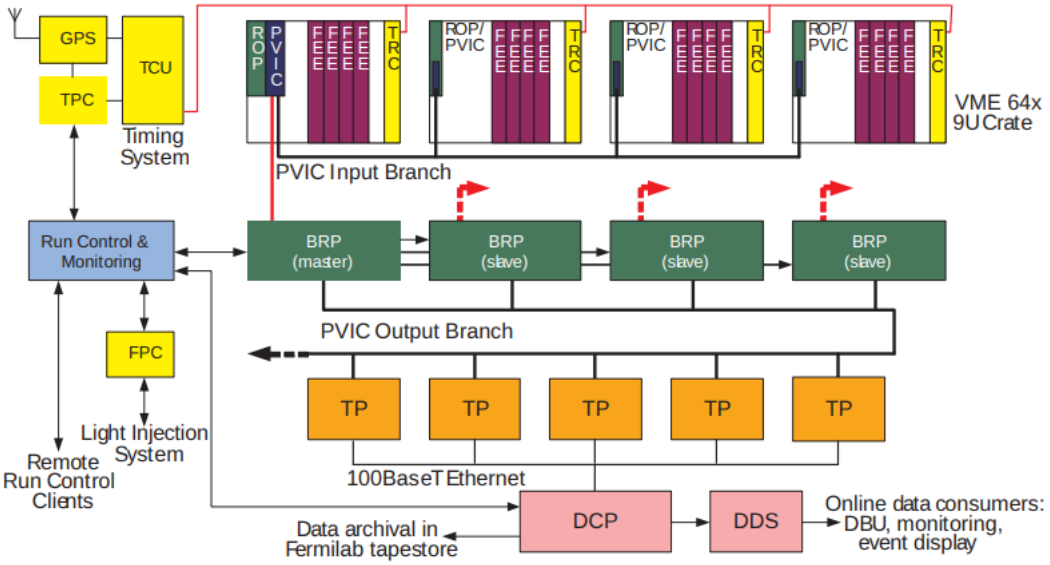

Figure 3.31: Schematic of the MINOS DAQ system. The front-end electronics of the FD and the clock system are shown as an example. Only one of six PVIC input branches is illustrated [68].

Before the data is stored to disk, a trigger condition must be met for the DAQ system. In the ND, when the beam spill gate trigger from the ACNET (Accelerator Control Network) happens, all data started to be recorded 1.5 μs prior to the arrival of the neutrino beam. This trigger is not present in the FD and, therefore, must be triggered in a remote way. This is given with a GPS (Global Positioning System) in the ND, generating a timestamp of the spill signals and then sending it to the FD through the internet [63].

The reading of the digitalized data from the front end electronics is made by computers named ROP (Readout Processor) in each electronics case. The FD has 16 ROPs and the ND has 8 ROPs. When the data is read, it is transfered via a PCI Vertical Interconnection (PVIC) to a computer that is off the detector called the BRP (Branch Readout Processor). One of these BRPs will be the master, it will select one of the Trigger Processors (TP) and then instructs the remaining BRPs to transfer their data to that TP via the PVIC output branches. The TPs will then apply algorithms to find the events that have physical interest [63]. All the data output from the TP is transmitted to the Data Collection Process (DCP) that collect and merges all the outputs from the TPs. Finally, the output stram is organized as a ROOT tree

and then written to disk. The active output file is shared with the DDS (Data Distribution System) that will serve as the data for online consumers such as the monitoring and event displays. A final data archival task transfers the files to the Fermilab storage facility over the internet [68].

3.4.4 Reconstruction

Once the data has been obtained from the DAQ its quality needs to be checked so it ensured that it was obtained under normal circumstances. Data, to be consider as "good" must include: that all detector systems must be working normally; there should be few malfunctioning readout components and the whole detector must be live [71].

All this process is supervised and other activities, such as the calibration of the detector, must be done in order to ensure that everything is working as normal. Given that some of these process are not going to be discussed here, it is recommended Refs. [68, 71] for a more in depth analysis of how these criteria are met.

For our purposes, we are interested in the reconstruction of the events and their topologies. The MINOS reconstruction is a framework in the C++ programing language that will take a simulated or digitalized snapshot from the detector readouts, called a "snarl". These snapshots must individually separate the neutrino interactions temporally and spatially so that events can be distingueshed. This can be seen in Figure 3.32.

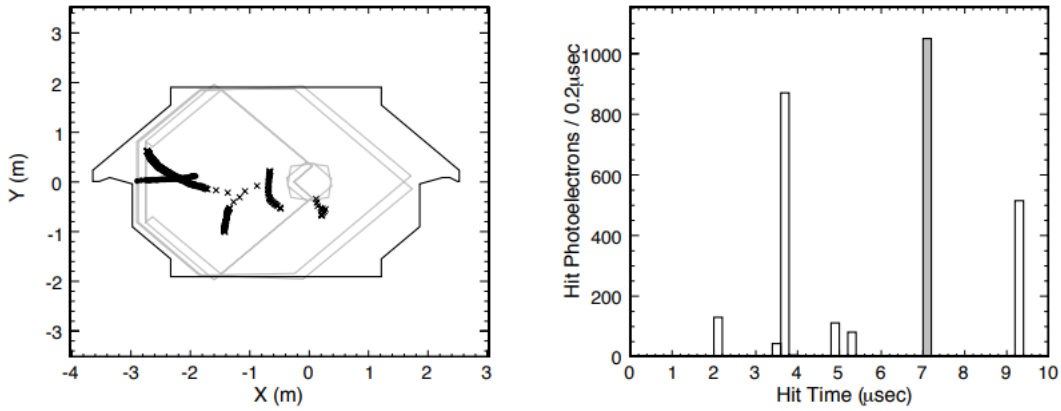

Figure 3.32: Example of a snarl in the ND, in the left we have neutrino interactions in space, while in the right we can see this distribution in time [74].

The MINOS experiment was optimized to study the disapperance of muonic neutrinos (ν_μ). Therefore, it is the interaction of principal interest, the charged current muon neutrinos (ν_μ CC). However, there are some other interactions that can be obtained and are useful for different studies. Some of those are: charged current muon antineutrinos ($\bar{\nu}_\mu$ CC), charged current electron neutrinos (ν_e CC), neutral current (NC) and charged current tauonic neutrinos (ν_τ CC) (this ones are very few and indistinguishable from NC events) [36, 74].

These interactions can be characterized. For the ν_μ CC and $\bar{\nu}_\mu$ CC events we expect to see a long, curbing muon track with a hadronic shower in the interaction vertex. To distinguished between the neutrino or antinuetrino we can look at the direction of the track curves in the magnetic field. The ν_e CC and NC events do not have muon tracks, but they can still be separated. The ν_e CC events are characterized by compact electromagnetic showers and the NC events have more diffuse hadronic showers. The interactions can be better seen in Figures 3.33 and 3.34 [74].

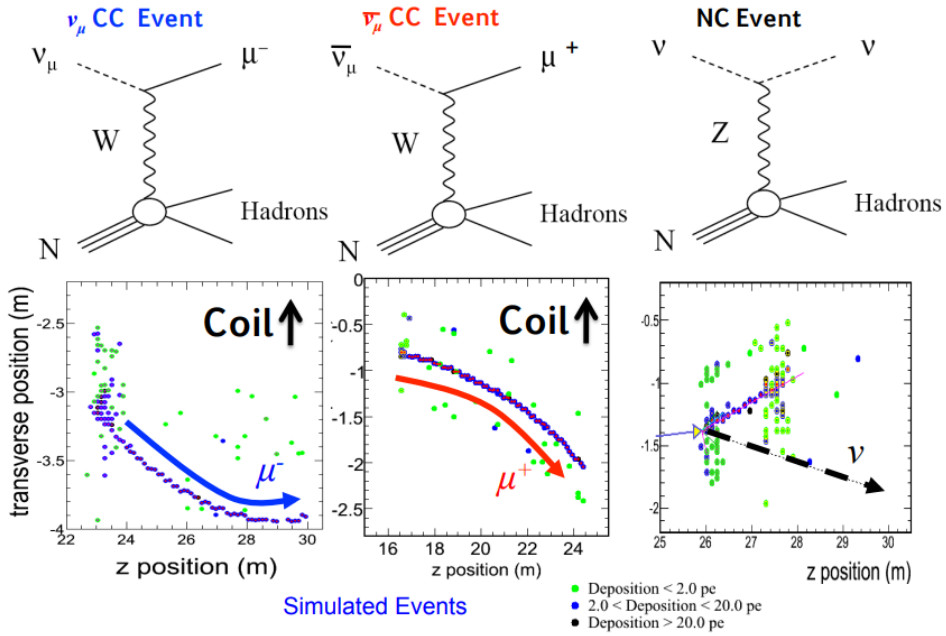

Figure 3.33: The event topologies of the following interactions: ν_μ CC, $\bar{\nu}_\mu$ CC and NC. The top three figures shows a Feynman diagram of the interactions and, the three images below, show the simulated event in one view (only the U plane). We can see the muon tracks for the CC events and the diffuse hadron shower of the NC [74].

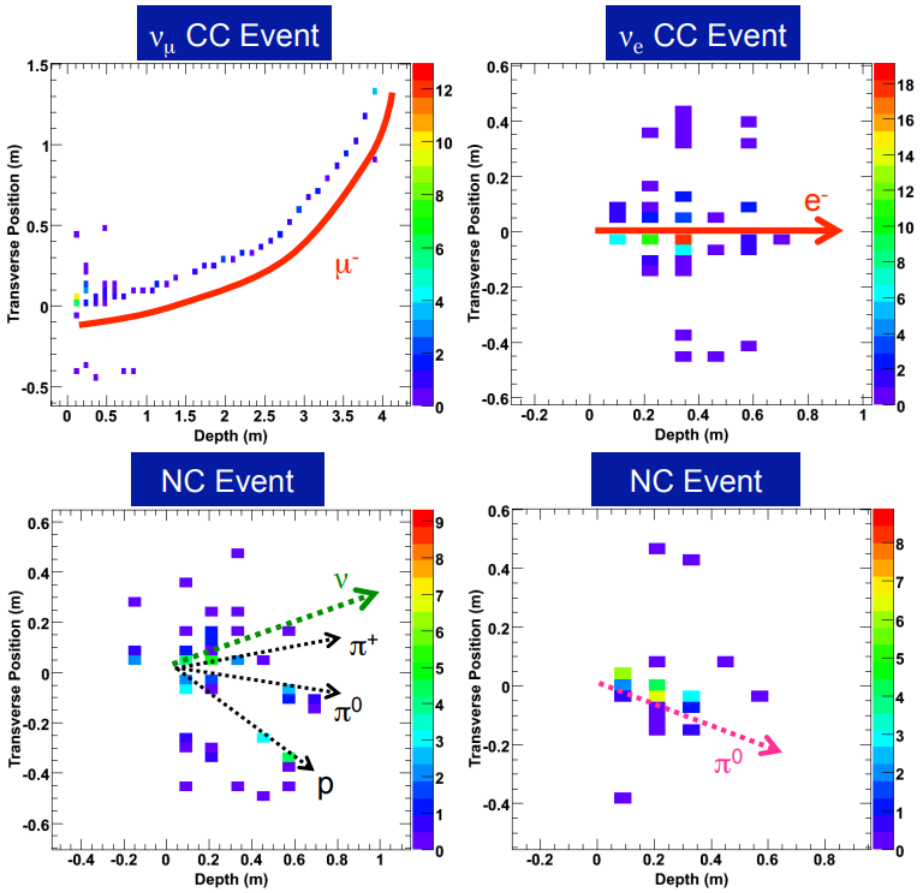

Figure 3.34: Display of simulated events in the MINOS detectors. The color scale shows the pulse heights. We again have the discription of a ν_μ CC event in the top left corner with the muon track. In the top right corner we see the ν_e CC event, with a more compact electromagnetic shower. In the bottom left we have a diffuse NC event and, in the bottom right, another NC event with a fraction of the shower being of electromagnetic nature [63].

With the events it is possible to create an histogram with the number of events and reconstructed energy of the neutrinos. These will be the object of study of our work. It is also important to say that, for our analysis, the only interaction we will be taking into consideration will be the ν_μ CC.

Chapter 4

Methodology

The objective of this work is to analyse the CC ν_μ data from the MINOS experiment and see how the addition of the MINOS+ data can influence the oscillation free parameters. We also aim to obtain a 90% limit for the τ_3/m_3 decay parameter for the model of neutrino oscillation with decay in vacuum and in matter using the MINOS experiment data, and also seeing the effects of the MINOS+ data when added to it.

In this chapter we will discuss the data extraction, the methods used for the calculations, the probability we have used and how we obtained the confidence regions of 90% CL (confidence level).

4.1 Data extraction

For this work we have used data from the histograms of the MINOS and MINOS+ experiments. In Appendix A, we show the tool used for the exctration, the calibration of the graphs and also the process of extraction of all the points.

In total we extract eight different data types. We will be using the following notation to reference the extracted data:

- N_{unosc}: Number of events without considering the effects of oscillation;
- N_{osc}: Number of events with oscillation best fit;
- N_{bg}: Number of background events;
- N_{data}: Number of data events of the analysis;
- N_{up}: Upper error with respect to number of the data events;

- N_{down}: Lower error with respect to number of the data events
- N_{right}: Upper error with respect to energy of the data events;
- N_{left}: Lower error with respect to energy of the data events.

4.1.1 Theoretical model

The theoretical model is what will allow us to compare the number of events we are getting with our probability function with the ones in the reconstructed histogram, but taking into consideration our oscillation probability model. With this, we can also get the values of our best fits and see how close they are with the results obtained with the experiment.

The first way to have a theoretical model, is to simply get the N_{unosc} and multiply it by a probability, in our case it could be (2.48), (2.76) or (2.118), this would allow us to write the following:

$$N_{theo} = N_{unosc} \times P_{\nu_\alpha \to \nu_\beta}. \tag{4.1}$$

However, we need to consider the presence of the background. The N_{unosc} data has the effects of the background noise considered when it is plotted. Hence, we need to remove them from the N_{unosc}, but, after we take the probability we need to add them back. This is because we want to compare our values with the data that does have the noise. Therefore, our final equation for the theoretical value is given as:

$$N_{theo} = \left(N_{unosc} - N_{bg}\right) \times P_{\nu_\alpha \to \nu_\beta} + N_{bg}. \tag{4.2}$$

This theoretical value is analogous to the N_{osc} in the sense that, we are using an oscillation probability model to account for its lack in the N_{unosc} data. Meanwhile, the N_{osc} comes from an internal analysis of the experiment.

4.1.2 Mean probability

One of the parameters that are fed into the probability is the energy of it. One of the approaches to calculate the theoretical value is to consider the mean energy of the bin in the probability. However, this methodology can be improved for it is a rough approximation.

As can be seen in Figures 4.1 and 4.2, the probability is not constant in the energy and, a bin of energy is contained within an interval. Therefore, a better way to calculate the probability is to compute it within the energy bins and take its average value.

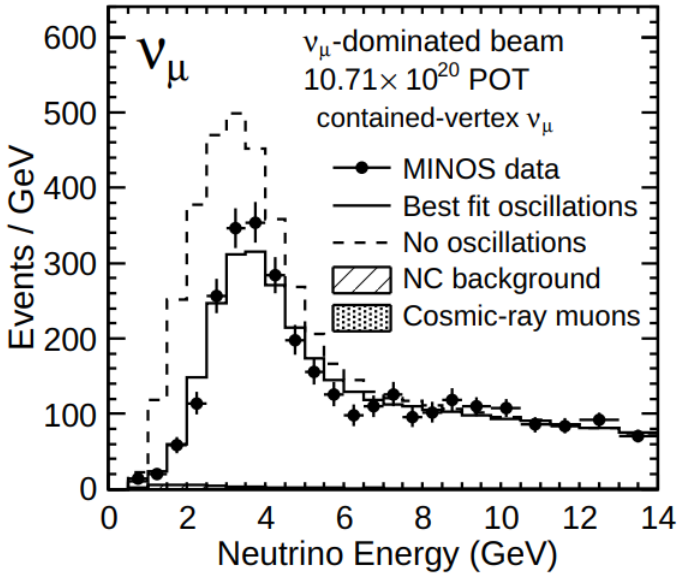

Figure 4.1: MINOS reconstructed events in function of the energy.

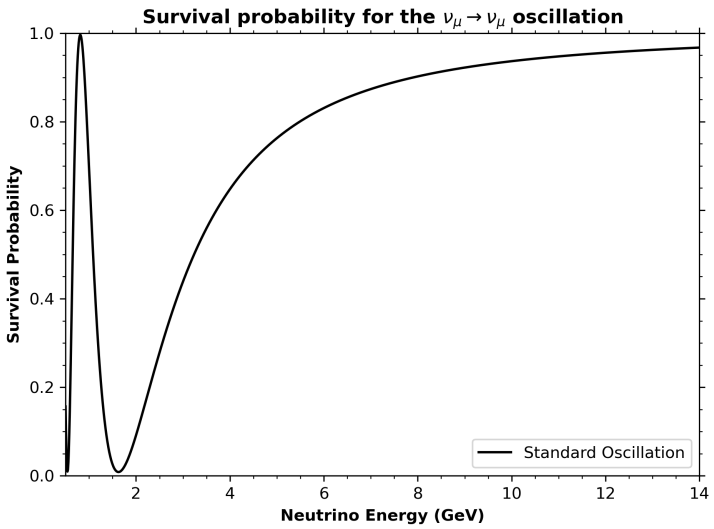

Figure 4.2: Three flavor oscillation survival probability of $\nu_\mu \to \nu_\mu$ in vacuum.

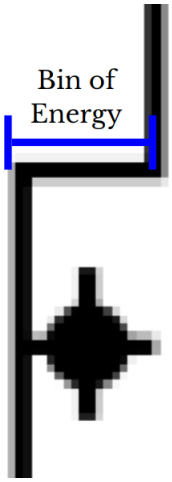

Figure 4.3: Representation of a bin of energy in a larger scale.

Consider the $i-nth$ bin of energy, as represented by Figure 4.3, has a width of δ_i and the average central energy of E_{ci}. We can consider that the mean value of the probability within this bin is given as:

$$\langle P \rangle = \frac{1}{\delta_i} \int_{(E_{ci}-\delta_i/2)}^{(E_{ci}+\delta_i/2)} f(E)P(E)dE, \tag{4.3}$$

where the $f(E)$ is a function defined to weight the probability, for our pourposes we will define that $f(E) = 1$. Hence, the mean probability is given as[6]:

$$\langle P \rangle = \frac{1}{\delta_i} \int_{(E_{ci}-\delta_i/2)}^{(E_{ci}+\delta_i/2)} P(E) dE. \tag{4.4}$$

If we wish to consider a function to weigh the probability that is not equal to one, we need to also reconsider the bin width with the more general equation:

$$\delta_i = \int_{(E_{ci}-\delta_i/2)}^{(E_{ci}+\delta_i/2)} f(E) dE. \tag{4.5}$$

For our computation, we need to convert Eq. (4.4) to a discrete form. That can be done in the following way:

$$\langle P \rangle = \frac{1}{N} \sum_{i=1}^{N} P(E_i), \tag{4.6}$$

considering that the energy interval of a bin is $(E_{ci} - \delta_i/2; E_{ci} + \delta_i/2)$ and with N being the number of partitions taken. Therefore, we can calculate the probability in each value of energy and take the average value. For our analysis we considered 250 partitions.

4.1.3 The errors

The last step in our extraction is to also consider the errors that will have an impact in our analysis. The first one is the data error (σ_{data}). When extracting the error bars from the data points, we must consider that part of the error is statistical and the other part is systematic. Because of this, the error bar can be asymmetric. Hence, we can define that our data error is given as:

$$\sigma_{data} = \sqrt{N_{up} \times N_{down}}. \tag{4.7}$$

[6]Given that $f(E)$ is a weight function, we want to consider that all the bins have the same contribution to the average probability. Meaning, that we need to take the value of $f(E) = 1$.

The second error that we must consider is the statistical error (σ_{stat}). For this error, we will consider the square root of our theoretical value:

$$\sigma_{stat} = \sqrt{N_{theo}}. \tag{4.8}$$

Finally, we have to consider the systematic error (σ_{sys}) that is obtained in the literature. Assuming a Poisson distribution the systematic uncertainty is of 4% [6]. We considered this value as the systematic error of the MINOS and MINOS+ experiment. Hence, our error will be this value multiplied by our theoretical model:

$$\sigma_{sys} = \text{Sys. Error} \times N_{theo}. \tag{4.9}$$

4.2 The χ^2 function

4.2.1 The distribution

For our analysis, we will be considering the χ^2 function which is defined as:

$$\chi^2(x_1, \cdots, x_N) = \sum_{i=1}^{n} \left[\frac{N_{theo,i} - N_{data,i}}{\sigma_{tot,i}} \right]^2, \tag{4.10}$$

we will use in this function in each bin and, in it, consider the value of the theoretical value, the real data and the total error, the latter being defined as:

$$\sigma_{tot,i} = \sqrt{\sigma_{data}^2 + \sigma_{stat}^2 + \sigma_{sys}^2}. \tag{4.11}$$

Once all the contributions are considered, we will have a resulting value for that scanning. For a more in depth explanation of the χ^2 function and its use in this work, Appendix B can be consulted.

We can use the value of the function to see how good our agreement is. If $\chi^2 = 0$ then we have a perfect agreement, which is highly unlikely to occur. However, if the total sum is

less or approximately equal to the number of terms in the sum, that is:

$$\chi^2 \lesssim n, \tag{4.12}$$

then the real data and the theoretical model are in good agreement. But, if the value is way grater than the number of bins:

$$\chi^2 \gg n, \tag{4.13}$$

we can suspect that something is not right with our model.

4.2.2 Degrees of freedom

The probability function takes many parameters that are free and may vary, at the same time, when we make a plot of our obtained results, we may be considering a 2D plot with two free parameters or a 1D plot with only one.

If we allow more parameters to be free to better fit our model, we can expect the χ^2 value to decrease. If we want to check the global value of our χ^2 function, taking into consideration this parameters, we need to divide its value by the number of degrees of freedom (D), that is:

$$\chi^2_{DF} = \frac{\chi^2}{D}, \tag{4.14}$$

where:

$$D = n - N, \tag{4.15}$$

the n value denotes the total number of measurments, in our case, the number of bins in the histogram. While the N is the total number of free parameters. If our χ^2_{DF} value is lower or close to 1, we have a good agreement of the model and the observed results.

However, if we want to plot our values in confidence intervals, the presence of the free parameters being ploted needs to also be taken into consideration. For the total value of the

χ^2 value will also change, Table 4.1 shows how the confidence intervals will change as we increase the degrees of freedom.

Table 4.1: Upper tail values for the chi-square distribution for N values of free parameters.

N	**90% CL**	**95% CL**	**97.5% CL**	**99% CL**	**99.9% CL**
1	2.706	3.841	5.024	6.635	10.828
2	4.605	5.991	7.378	9.210	13.816
3	6.251	7.815	9.348	11.345	16.266
4	7.779	9.488	11.143	13.277	18.467
5	9.236	11.070	12.833	15.086	20.515

When plotting a graph the number of free parameters of it does not need to be N (that is, the total number of free parameters), it will be the number of free variables being ploted. Normally being two for 2D plots and one for 1D plots.

4.2.3 Adding two data sets

Besides working with the MINOS experiment, we also want to combine both the MINOS and MINOS+ data to make compare the effects of it. For our statistical analysis, if we have two data sets, N_1 and N_2, we can define the combined analysis as their sum:

$$N = N_1 + N_2. \tag{4.16}$$

For the χ^2 function, the same can be said. The resulting value will be the sum of the χ^2 function applied in both data sets, therefore:

$$\chi^2(x_1, \cdots, x_n) = \sum_{i=1}^{N_1} \chi^2_{1,i} + \sum_{j=1}^{N_2} \chi^2_{1,j}, \tag{4.17}$$

the summation over i and j are to distinguish that both sets can have a different number of bins. However, we will consider that they both have the same amount of free parameters $(x_1, \cdots, x_n)$.

We can also calculate the function considering the degrees of freedom. In this case, the total number of measurements n takes the following form:

$$n = n_1 + n_2, \tag{4.18}$$

since the number of free parameters N is the same, equations (4.14) and (4.15) can still be used.

4.2.4 Minimum of the function

Our analysis consists in making a scan of the free parameters that we have interest with the χ^2 function. For each set of parameters that we use $(x_1, \cdots, x_n)$ we will have a χ^2 value for it. We will define that the best fit of our analysis is the one that has the lowest value for the chi distribution, hence, the one that minimizes it.

Since we do not use normalization in this work, all of the parameters have physical meaning. As discussed prior, we will be working with the models shown in Sections 2.5, 2.6 and 2.7.

The parameters for the oscillation with decay in vacuum are the same for the ones in matter. We can see Table 4.2 and 4.3 to see all the parameters and the granularity[7] of each set.

[7]The granularity is given by the step used. The step is the number of points used between the lower and upper bound, separated in a linear way.

Table 4.2: Parameters being scaned for the standard oscillation probability in the left. In the right we have the bounds of the interval of scanning and the step used.

Parameter	**Lower Bound**	**Upper Bound**	**Step**
$\mathbf{\Delta m^2_{32}}$	1×10^{-3}	7×10^{-3}	750
$\mathbf{\sin^2 \theta_{23}}$	0	1	750

Table 4.3: Parameters being scaned for the oscillation with decay in vacuum and oscillation with decay in matter in the left. In the right we have the bounds of the interval of scanning and the step used.

Parameter	**Lower Bound**	**Upper Bound**	**Step**
$\mathbf{\Delta m^2_{32}}$	1×10^{-3}	7×10^{-3}	500
$\mathbf{\sin^2 \theta_{23}}$	0	1	500
α_3	1×10^{-5}	1×10^{-2}	125

The intervals were left in a wide range, even though we knew what was the expected best fit. The choice to leave them wider was made for constructing the confidence regions, as well as to guarantee that, because of the addition of another data set, we would still be within a good range. It is also important to enunciate that, for this work, we will be considering $\delta_{CP} = 0$.

For the MINOS analysis in the standard oscillation, the value of the $\sin^2 \theta_{23}$ needed to be converted to $\sin^2 2\theta_{23}$ for the comparation with the literature.

4.3 Construction of the confidence intervals

4.3.1 Data selection

Once all the points have been scanned by using a Python script, we need to select them to construct the plots. Given that we have a set of parameters that minimize the chi function,

we can define a new quantity that will be used for defining the confidence intervals:

$$\Delta\chi^2(x_1,\cdots,x_n) = \chi^2(x_1,\cdots,x_n) - \chi^2_{best\,fit}, \tag{4.19}$$

Eq. (4.19) tell us that if we have a set of parameters that were scanned $(x_1,\cdots,x_n)$ we can calculate its $\Delta\chi^2$ value by subtracting from it the best fit value. This also imples that, for the best fit, the $\Delta\chi^2_{best\,fit} = 0$.

We can also recall Table 4.1 for the minimum value that the $\Delta\chi^2$ must have for the point to be considered within the confidence level range denoted in the table.

4.3.2 Marginalization

Another process that will be applied in the construction of the plots is the marginalization. Let us consider an example of an arbitratry set of points $(a_n, b_n, c_n, \cdots)$, each with a certain $\Delta\chi^2$ value.

If we want to plot the a value with respect to the $\Delta\chi^2$ and make a 1D plot, we firstly need to consider that the scan will produce many set of points that will have repeated values. As such:

$$\begin{aligned}
(a_1, b_1, c_1, \cdots) &\rightarrow \Delta\chi^2_1 \\
(a_1, b_2, c_1, \cdots) &\rightarrow \Delta\chi^2_2 \\
(a_1, b_1, c_2, \cdots) &\rightarrow \Delta\chi^2_3 \\
(a_1, b_2, c_2, \cdots) &\rightarrow \Delta\chi^2_4, \\
&\vdots
\end{aligned}$$

all of the above set of points do have the first a_1 point, but have different $\Delta\chi^2$ values and also have other points contained in the set. Therefore, we are going to choose the set of points that have the a_1 value and also has the minimum value for the $\Delta\chi^2$. The same process is then

repeated for all the other a_n points and, the selected ones, will be used to make the 1D plot. We then say that this plot is marginalized with respect with the $(b_n, c_n, \cdots)$ parameters.

In 2D the process is the same, with the change that we would be interested in the pair (a_n, b_n) that minimizes the $\Delta\chi^2$ value. And the same could be done to other any other set of points.

4.3.3 1D/2D Plots

Given the process of data selection and marginalization, the plots can be constructed. For the 2D plot, we do a marginalization of Δm^2_{32} and $\sin^2\theta_{23}$, in the standard oscillation they are the two free parameters, hence no marginalization is required in this case.

The result that we will have is a point with three coordinates $\left(\Delta\chi^2, \Delta m^2_{32}, \sin^2\theta_{23}\right)$. We will need to draw a contour plot, in which the axes are the mass and sine terms. The plot will not include a color scale but will instead display only the contour line. The line that will be presented describes the 90% CL interval. For the data being selected, given that there are 2 free parameters, this implies in the condition that:

$$\Delta\chi^2 \leq 4.605, \tag{4.20}$$

the presented value can be seen in Table 4.1, considering a 90% CL region with two degrees of freedom.

For the 1D plots the process described is the same. We will plot one of the free parameters $\left(\Delta m^2_{32}, \sin^2\theta_{23} \text{ or } \alpha_3\right)$ with respect to the $\Delta\chi^2$ value in the y-axis. After the marginalization is done, we select the data based on the following requirement, now considering a 90% CL region with just one degree of freedom:

$$\Delta\chi^2 \leq 2.706. \tag{4.21}$$

For the best fit errors to be presented, we use the 1D graph plots and see the intersection with the 68% line is met, which is the value $\Delta\chi^2 \approx 1$.

4.4 Numerical calculations

In Section 2.7 it is discussed that, for the calculation of neutrino oscillations with decay in matter, we will use the series expansion provided by *Grönroos et al.* [3], that can be seen in Eq. (2.118). However, we are also going to compare it to a numerical approach to validate it. We will be adopting the same numerical approach as done by *Denton & Parke* [76].

We will be considering the Hamiltonian in Eq. (2.114), using this we can write a expression for the probability amplitude as:

$$\mathscr{A} = \exp^{-iHL}, \tag{4.22}$$

and, therefore, write the whole probability in terms of the square module of the amplitude:

$$P_{\nu_\alpha \to \nu_\beta} = \left|\mathscr{A}_{\alpha\beta}\right|^2, \tag{4.23}$$

Eq. (4.22) requires us to diagonalize the Hamiltonian, giving us the eigenvectors and eigenvalues (λ_i).

We can then build a matrix V from the eigenvectors and use a diagonal matrix with the eigenvalues to calculate the amplitude, as such:

$$\mathscr{A} = V \begin{pmatrix} e^{-i\lambda_1 L/2E} & 0 & 0 \\ 0 & e^{-i\lambda_2 L/2E} & 0 \\ 0 & 0 & e^{-i\lambda_3 L/2E} \end{pmatrix} V^\dagger, \tag{4.24}$$

using Eq. (4.23) we can get a 3x3 matrix with the probabilities of oscillation. We will also write the MSW constant not as in Eq. (2.110), but as:

$$V_{CC} = 1.52 \times 10^{-4} \left(\frac{Y_e \rho}{g/cm^3} \right) \left(\frac{E}{GeV} \right) eV^2, \tag{4.25}$$

where Y_e is the electron fraction, being of about ~ 0.5 in the Earth and ρ the density of the matter.

Chapter 5

Results

The first part of our results will be using the MINOS histogram present in Ref. [77] and, for the MINOS+, see Ref. [36]. Our data is then consisted of 1.68×10^{20} *POT* from MINOS+ and 10.71×10^{20} *POT* from the MINOS experiment of ν_μ CC data. We will first reconstruct the MINOS experiment and compare it with the literature to then add the MINOS+ data.

In the second part of the results, we will be testing the numerical and analytical approach for the oscillation with decay in vacuum and in matter models and, afterwards, use it to achieve a limit for the τ_3/m_3 parameter.

5.1 Standard oscillation

5.1.1 MINOS validation

We wish to first see if our best fit and confidence intervals are close to the ones found in literature to validate the model, afterwards, our objetive will be to see the influence of the new data set. Making the extraction of the histogram we first reconstruct the data, as can be see in Figure 5.1.

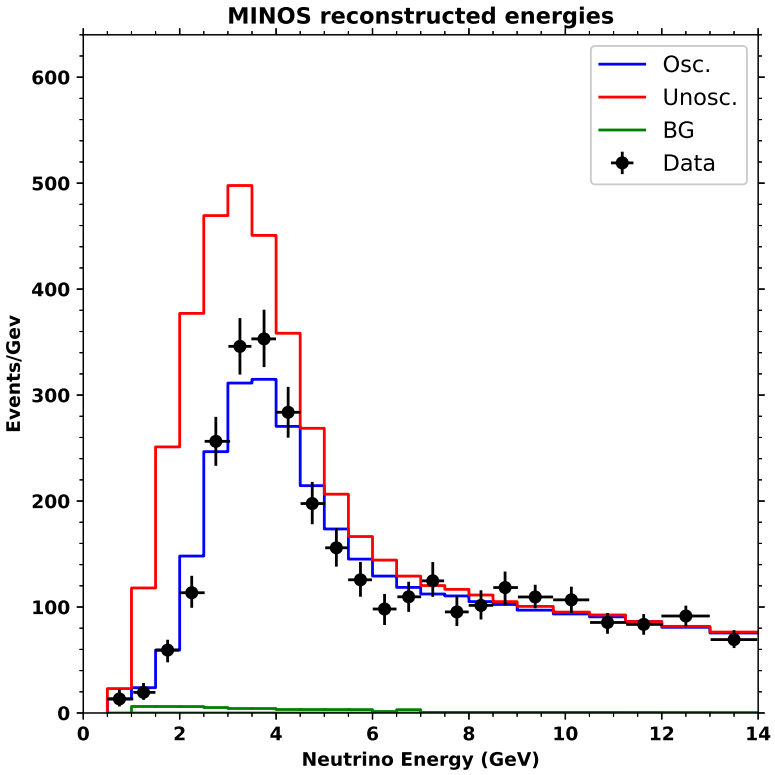

Figure 5.1: Reconstruction of the MINOS histogram for validation in the data extraction.

The reconstructed data shows that the extraction does not have any big discrepancies. We must take into account that the MINOS reference, see Ref. [77], uses $\bar{\nu}_\mu$ CC events and, even so, we were able to obtain results that do not diverge as much from the one in the reference. The best fit values of the original MINOS analysis is in the first line of Table 5.1 and our best fit results is in the second line of the same table.

Table 5.1: Best fit values for the Δm^2_{32} and $\sin^2(2\theta_{23})$ parameters. In the first line we have these values for the MINOS analysis made in Ref. [77] (taking into consideration $\bar{\nu}_\mu$ CC events). For the second line we have our analysis best fit values with the respective χ^2 and χ^2_{DF} values.

	Δm^2_{32} $(10^{-3} eV^2)$	$\sin^2(2\theta_{23})$	χ^2	χ^2_{DF}
MINOS Reference	$2.41^{+0.09}_{-0.10}$	$0.950^{+0.035}_{-0.036}$	—	—
Our Analysis	$2.298^{+0.152}_{-0.149}$	$0.935^{+0.049}_{-0.092}$	11.32	$11.32/21 \sim 0.54$

From the same table, we have our χ^2 value, and the reduced one. Both show us that the model is in agreement with the data exctracted.

Using our best fit we can plot it to see how big is the discrepancie with the MINOS best fit plot, represented in Figure 5.2. And, as it can be seen, there is only a small discrepancie in the low energy bins, which is reasonable and to be expected.

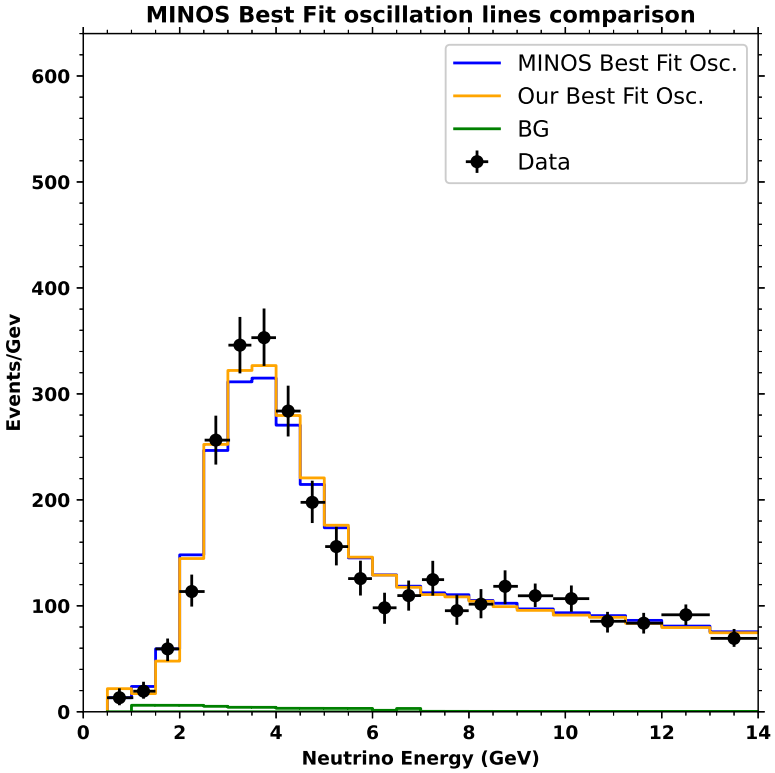

Figure 5.2: Comparison of the best fit oscillation lines obtained from the MINOS analysis in Ref. [77] (blue line) with our best fit value represented in the second line of Table 5.1 (yellow).

With these values we can also plot the 2D region with a confidence level of 90% as can be seen in Figure 5.3.

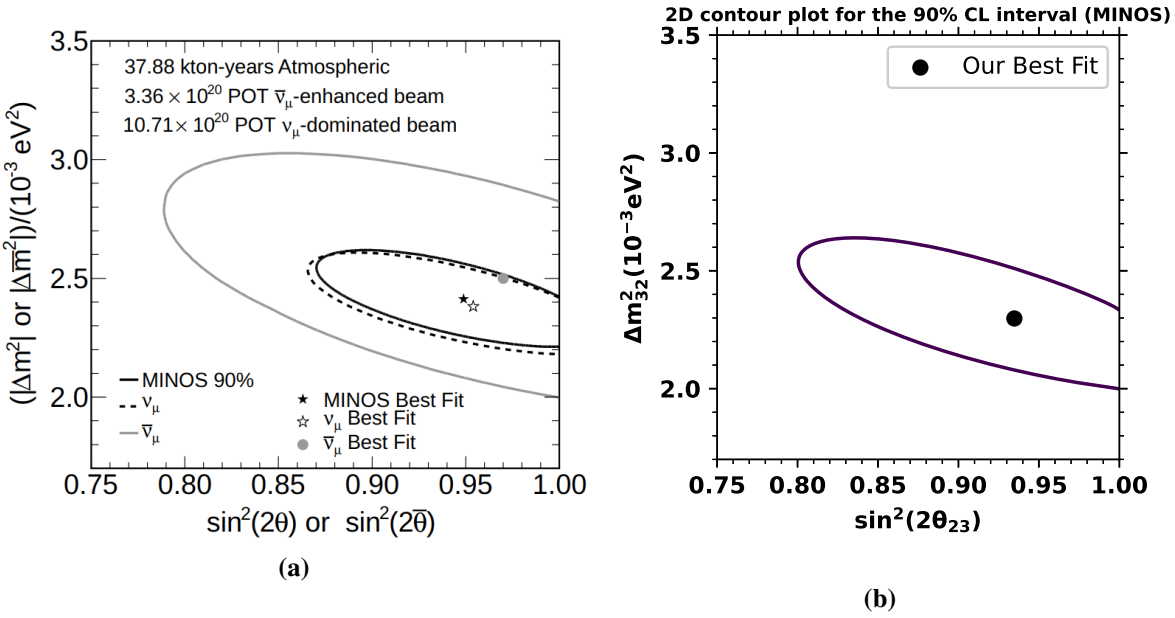

(a) **(b)**

Figure 5.3: (a) MINOS 90% CL region assuming identical neutrino and antineutrino oscillation compared with ν_μ and $\bar{\nu}_\mu$ regions [77]. (b) MINOS 90% CL region for our scan considering only the ν_μ oscillation scenario with 10.71×10^{20} POT.

If we compare both this images, we can see that our best fit value still is close to the ν_μ best fit found in Figure 5.3a. However, we can also see that our approach leads to a larger confidence interval, as can be seen in Figure 5.3b, for the $\sin^2(2\theta_{23})$ and for the Δm^2_{32} parameters, when compared with the dashed line of Figure 5.3a.

This result probably emerges from the methodology used, a normalization factor could be applied in the analysis for a better result as it was done in Ref. [44]. However, our main objective is to see the influence of the MINOS+ into the MINOS data, the use of an extra factor could result in better confidence intervals, at the expense of also changing the influence of the merged data sets from two different experiments. Therefore, this model will give different intervals from the ones in the literature (that aims in restraining even further the physical parameters), but this does not impact our analysis. Given that our objective is not to restrain them, but to have a confidence interval similar to the ones in literature for validation.

Figures 5.4 and 5.5 allow us to compare the 90% CL regions of our analysis with the ones in Ref. [44]. Again, our objective is to validate that our plots and regions are in agreement with the literature.

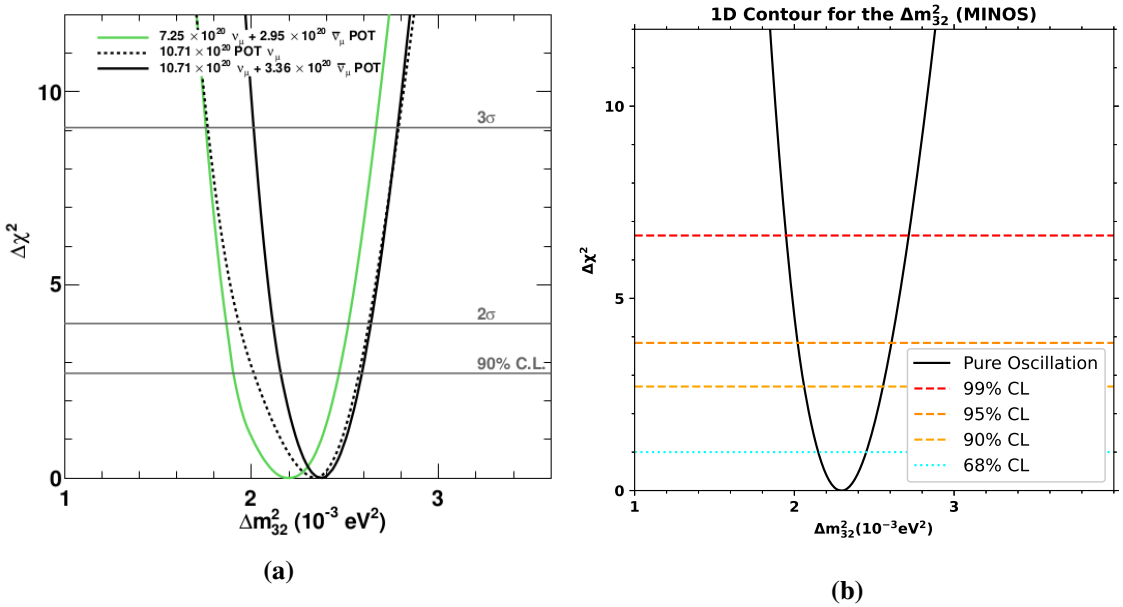

Figure 5.4: (a) MINOS 90% CL for different POTs for the Δm^2_{32} parameter. The dashed line represents the ν_μ CC events and, therefore, are the one we will be comparing [44]. (b) The 1D region obtained with our scanning, the dashed lines represent different confidence levels and the points represent the confidence intervals, while the black line represents our contour.

We can compare the dashed line presented in Figure 5.4a with the line from 5.4b. Taking our intervals of 90% CL we can arive at the following (the square mass terms are in $10^{-3}eV^2$):

$$2.061 < \Delta m^2_{32} < 2.555, \tag{5.1}$$

while the one presented in Ref. [44] is:

$$2.09 < \Delta m^2_{32} < 2.67, \tag{5.2}$$

We can observe that our interval is narrower than the one presented in the reconstruction made from [44] in 0.086 eV^2.

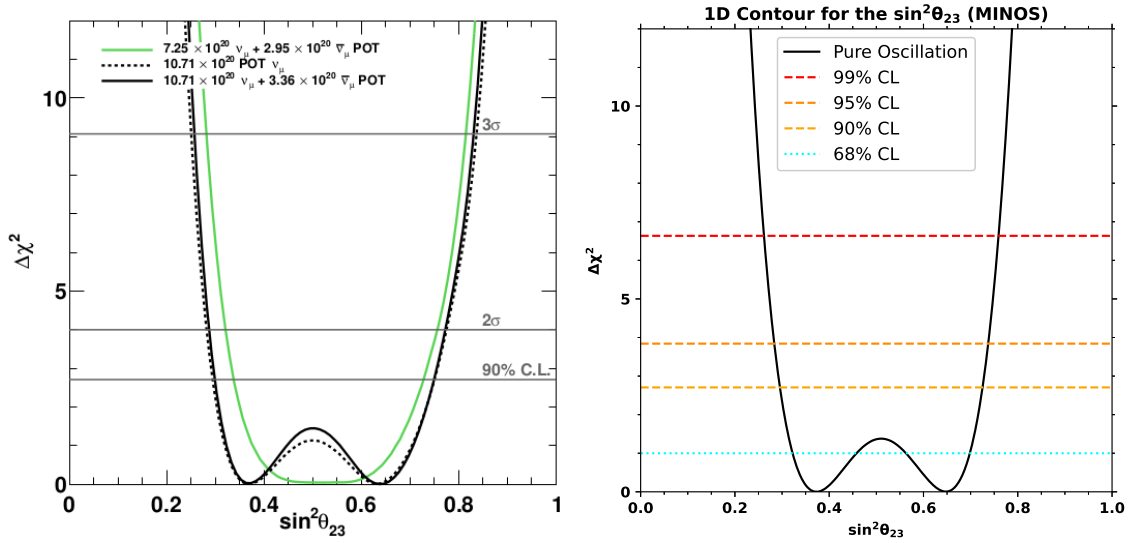

(a) **(b)**

Figure 5.5: MINOS 90% CL for different POTs for the $\sin^2(\theta_{23})$ parameter. The lines represent the same regions as the Figure prior. The sine interval has 2 different 68% CL intervals, we will be considering the one with the best fit value.

For the sine interval, we must again compare the dashed line from Figure 5.5a with the one in Figure 5.5b, given that it is the one with the ν_μ CC events. Considering our 90% CL interval, we arrive at the following:

$$0.29 < \sin^2(\theta_{23}) < 0.72, \tag{5.3}$$

meanwhile, the reference presents its region as:

$$0.29 < \sin^2(\theta_{23}) < 0.74, \tag{5.4}$$

for the sine, we can see that both approaches leads to approximately the same 90% CL region, as the upper bound difference is too small.

We can consider our recreated plot validated and add the POT from the MINOS+ spectra and compare it to the results we already have.

5.1.2 MINOS+ effect in the MINOS data

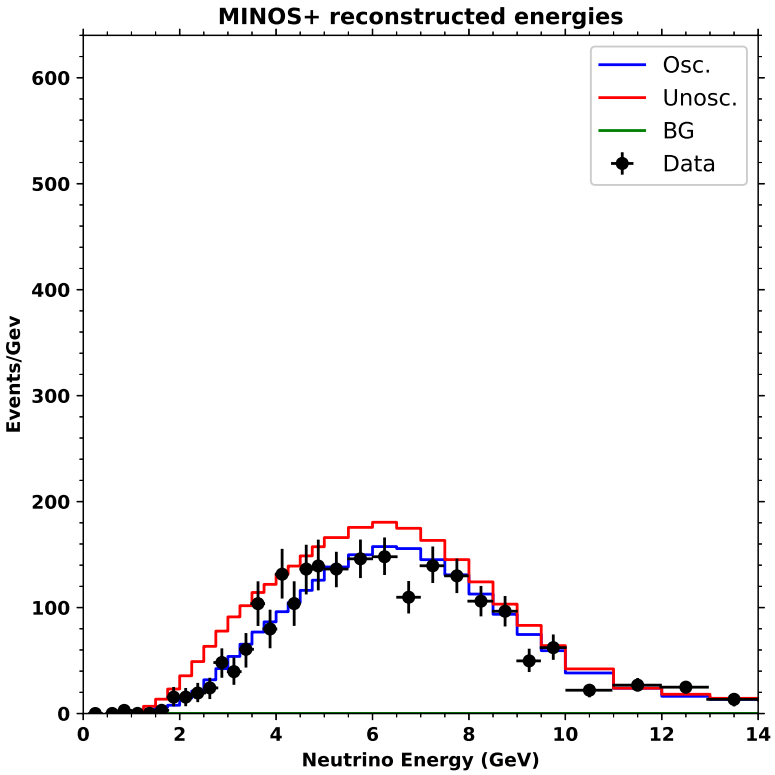

Figure 5.6: Reconstruction of the MINOS+ histogram for validation in the data extraction.

The best fit values that we arrive with the combined data set can be seen in the second line of Table 5.2. Comparing it with our MINOS results (see first line of the same table), we already see that the mass value has been shifted to a value closer to the one presented in Ref. [77] (see first line of Table 5.1). The sine value does not show much improvement, and our χ^2_{DF} is still lower than 1, suggesting an agreement of the model with the data.

Table 5.2: Best fit values for the Δm^2_{32} and $\sin^2(2\theta_{23})$ parameters, with our χ^2 and χ^2_{DF} values for the standard oscillation model. In the first line we have the values for our MINOS analysis (10.71×10^{20} POT ν_μ). In the second line we have our analysis best fit values for the MINOS & MINOS+ data ($10.71 \times 10^{20} + 1.68 \times 10^{20}$ POT ν_μ).

	Δm^2_{32} $(10^{-3} eV^2)$	$\sin^2(2\theta_{23})$	χ^2	χ^2_{DF}
MINOS	$2.298^{+0.152}_{-0.149}$	$0.935^{+0.049}_{-0.092}$	11.32	$11.32/21 \sim 0.54$
MINOS & MINOS+	$2.314^{+0.150}_{-0.143}$	$0.931^{+0.046}_{-0.093}$	39.57	$39.57/61 \sim 0.65$

We can further investigate this with the contour plots. For Figure 5.7 we can see that the sine has low impact, given that the region is still goes upwards of 0.8 for the sine. However, it does seem narrower along the mass axis and is shifted upwards compared to the MINOS dataset alone.

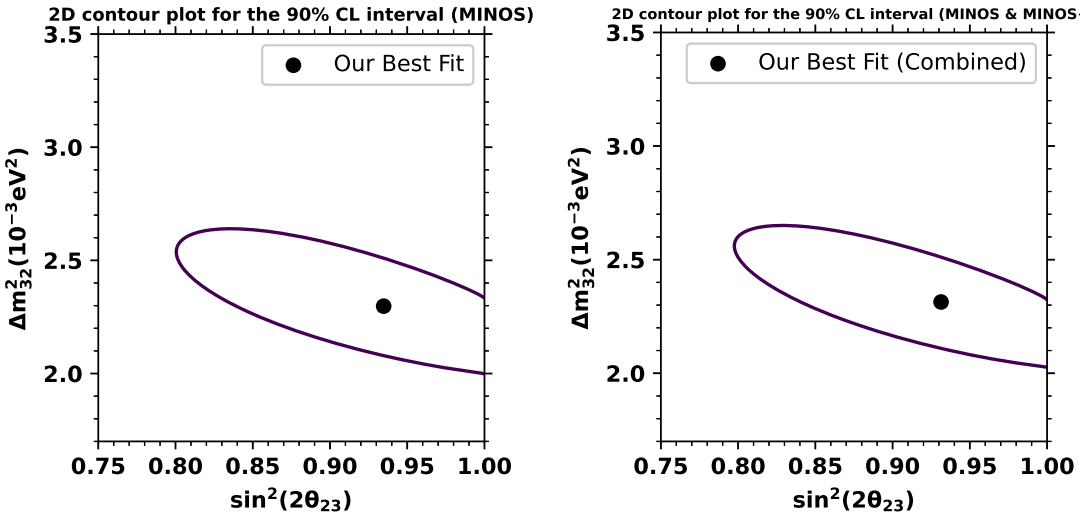

(a) **(b)**

Figure 5.7: (a) MINOS 90% CL region for our scan considering only the ν_μ oscillation scenario with 10.71×10^{20} POT. (b) MINOS & MINOS+ 90% CL region for our scan considering only the ν_μ oscillation scenario with 10.71×10^{20} POT from the MINOS experiment and 1.68×10^{20} POT from the MINOS+ experiment.

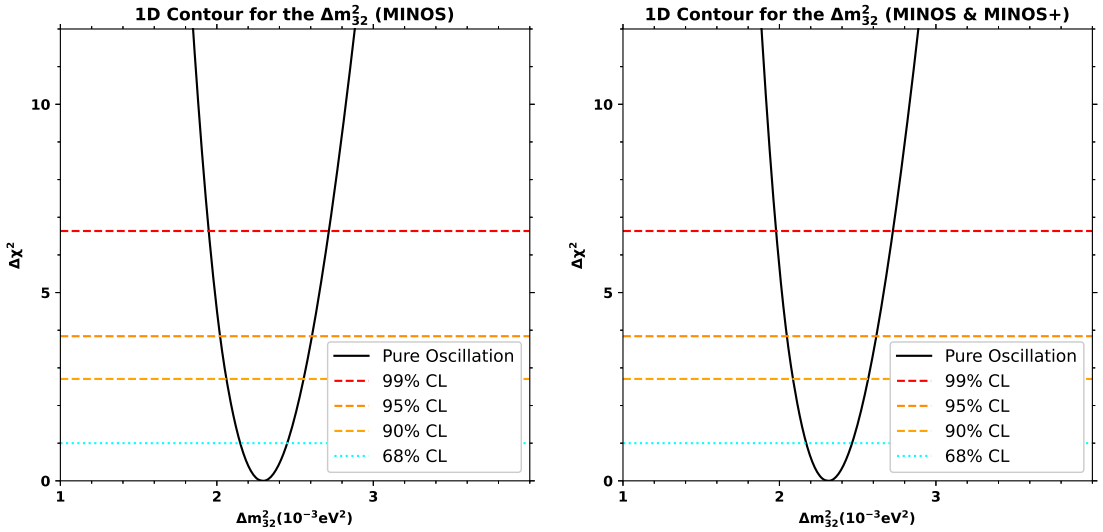

(a) **(b)**

Figure 5.8: (a) The 1D region obtained with our scanning of the MINOS experiment for the Δm^2_{32} parameter. The dashed lines represent different confidence levels and the points represent the bounds of the confidence intervals, while the black line represents our contour. (b) The same 1D region with same parameters and lines, but using the data set of the MINOS and MINOS+ experiment.

The change in intervals can also be seen by in the mass and sine parameters. For the mass, with Figures 5.8a and 5.8b, our previous plots considered the following 90% CL interval (the square mass values are in $10^{-3}eV^2$):

$$2.061 < \Delta m^2_{32} < 2.555, \tag{5.5}$$

the addition of the MINOS+ data gives the new following interval set:

$$2.086 < \Delta m^2_{32} < 2.567, \tag{5.6}$$

this show us that the presence of the MINOS+ data turns the 90% CL region narrower by a 0.0125 eV^2 (considering the width of the interval). Besides this, the mass is shifted 0.016 eV^2, that implies in a reduction in the error of about 1.73%, when compared with the

MINOS best fit (see Table 5.1). The shift in the mass parameter also implies in a shorter peaks of the oscillation probability.

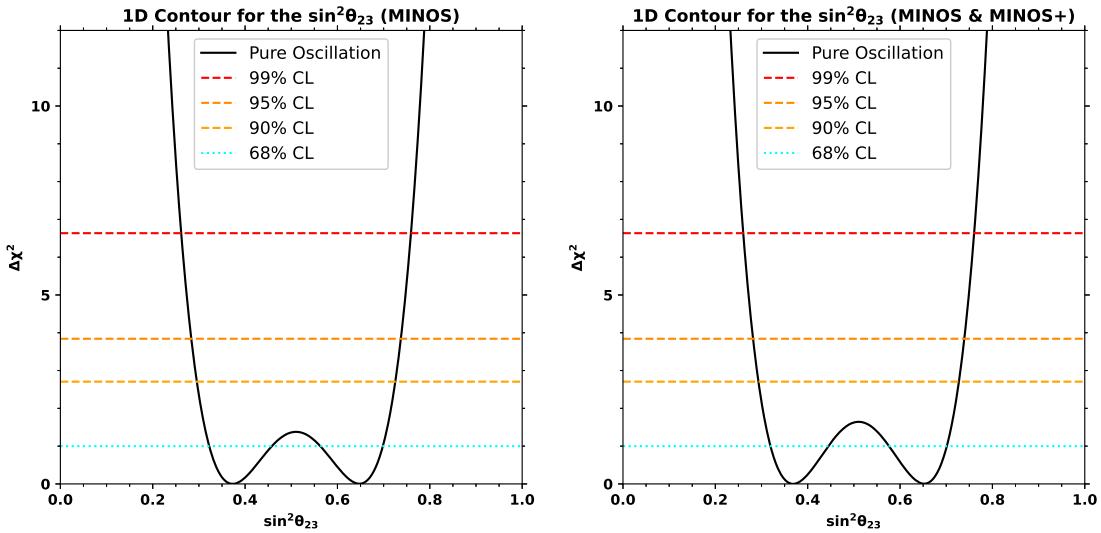

(a) **(b)**

Figure 5.9: The same caption as the Figure prior, but now for the $\sin^2\theta_{23}$ parameter. The sine interval has 2 different 68% CL intervals, we will be considering the one with the best fit value.

In the case of the angle, considering Figures 5.9a and 5.9b, there is no change in the intervals width, and the shift experienced in the best fit value is also negligible, therefore, not giving influence in the θ_{23} parameter.

The presence of the MINOS+ dataset, therefore, shows us that there is no improvement in the θ_{23} parameters, but improves the Δm^2_{32} when considering the MINOS best fit of 2.41×10^{-3} (eV^2). Given that we already know the influence of the MINOS+ data in the standard oscillation framework, we will consider the model of oscillation with decay in vacuum to study if any influence will arrise with the combined data sets and also to measure the α_3 parameter of decay.

5.2 Oscillation with decay in vacuum

5.2.1 Validation of the MINOS data

Our first approach is to validate our model, using now the following probability:

$$\begin{aligned} P_{\nu_\mu \to \nu_\mu} = U_{\mu 1}^4 + U_{\mu 2}^4 + U_{\mu 3}^4 \exp\left(-\alpha_3 \frac{L}{E}\right) + 2\left\{U_{\mu 1}^2 U_{\mu 2}^2 \cos\left(2.54\Delta m_{31}^2 \frac{L}{E}\right)\right. \\ + U_{\mu 1}^2 U_{\mu 3}^2 \exp\left(-\alpha_3 \frac{L}{2E}\right) \cos\left(2.54\Delta m_{31}^2 \frac{L}{E}\right) \\ \left. + U_{\mu 2}^2 U_{\mu 3}^2 \exp\left(-\alpha_3 \frac{L}{2E}\right) \cos\left(2.54\Delta m_{32}^2 \frac{L}{E}\right)\right\}. \end{aligned} \tag{5.7}$$

For this, we will be considering a similar analysis that used this probability and the MINOS data as a comparison (see Ref. [44]). We must also consider that the model in this referece does use a normalization constant. The contour plots of the reference consider the $\nu_\mu + \bar{\nu}_\mu$ CC events, hence, difference in regions are expected. There is no best fit value for the α_3 parameter using just the ν_μ data, hence we will be comparing it to the $\nu_\mu + \bar{\nu}_\mu$ CC events case, but the reference does provide a 90% confidence level interval for the α_3 parameter ν_μ CC events case. Again, we are trying to have the same effect, but not a perfect reconstruction of the regions and best fit.

We can see the best fit results from the reference and our analysis in Table 5.5. The table presents the value for τ_3/m_3 which, already considering the natural units constants, is the same as:

$$\frac{\tau_3}{m_3} = \frac{1}{3 \times 10^{14} \times \alpha_3}, \tag{5.8}$$

we will add an extra column for the equivalent value for the α_3 parameter.

Table 5.3: Best fit values for the Δm^2_{32}, $\sin^2(\theta_{23})$, τ_3/m_3, α_3 and the lower limit of 90% CL for the τ_3/m_3 parameter. In the first line we have the values for the MINOS analysis made in Ref. [44] (taking into consideration $\bar{\nu}_\mu$ events). In thse second line we have our analysis best fit values with the respective χ^2 and χ^2_{DF} values.

	$\mathbf{\Delta m^2_{32}}$ $(10^{-3}eV^2)$	$\mathbf{\sin^2(\theta_{23})}$	τ_3/m_3 (s/eV)	α_3 (GeV/km)	τ_3/m_3 (s/eV) $(90\%\ CL)$	χ^2	χ^2_{DF}
MINOS Reference	2.34	0.37	6.01×10^{-11}	5.55×10^{-5}	$>2.4\times10^{-12}$	—	—
Our Analysis	$2.263^{+0.171}_{-0.250}$	$0.675^{+0.077}_{-0.099}$	1.323×10^{-11}	2.52×10^{-4}	$>1.77\times10^{-12}$	11.14	$11.14/20\sim0.56$

Considering Table 5.5 we can already spot some discrepancies. The Δm^2_{32} is shifted to the left, but the reference value is still within the 68% CL interval of our analysis.

We can also see a big discrepancie in the $\sin^2\theta_{23}$ term, however, this difference is explained by the octant problem[8]. The value of the reference is at the lower octant, while our is in the higher octant. It can also be seen through the 1D contours of the $\sin^2$ function that has 2 minimum values. Hence, this difference is not as alarming as it seems.

The last value that has a difference is the α_3 parameter, being one order of magnitude lower than the reference. However, we should consider for the decay analysis the τ_3/m_3 parameter, for it contains the half-life term τ_3, even if it is in an indirect form. The τ_3/m_3 value in our analysis is in the same order of magnitude of the one presented by the reference, hence, even for the different values, they are within the expected order of magnitude (10^{-12}) for LBL experiments.

Finally, we can also see that our model still has a good agreement with the data set used, given that the χ^2_{DF} value is below 1.

We can consider that most of the different values emerges from the methodology used in the works. The best fit values we obtained, for a model without the normalization factor, already shows a well agreement with the expected in the literature.

[8]The value of θ_{23} is not maximal. That it to say that the neutrino data suggests two nearly degenerate solutions for the angle value, the first one being in the lower octant (LO: $\theta_{23} < 45°$) and the other in the higher octant (HO: $\theta_{23} > 45°$) [42].

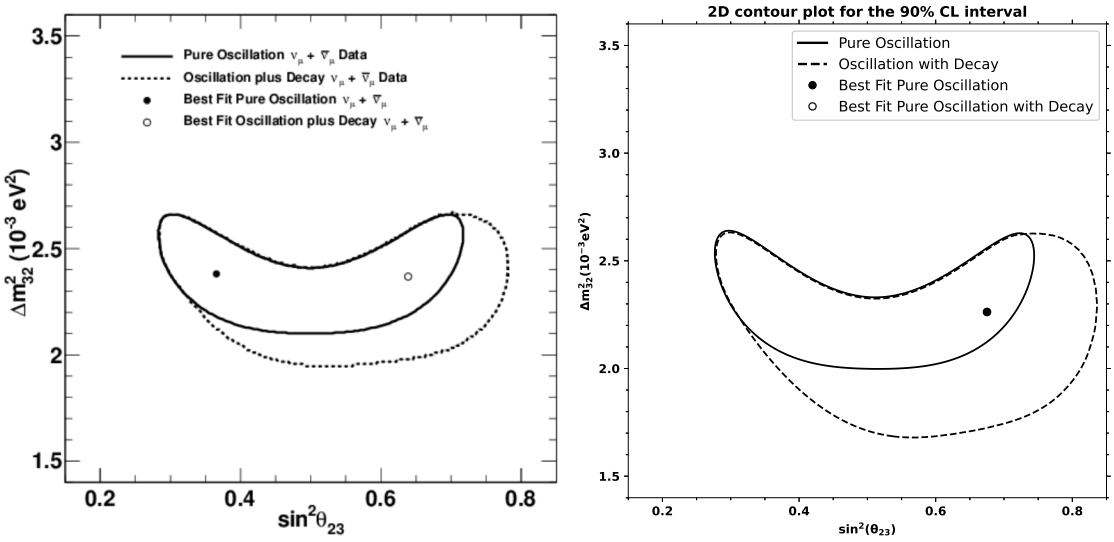

Figure 5.10: (a) Contour plot in the reference for the 90% CL region for the Δm^2_{32} with respect to $\sin^2\theta_{32}$, the solid black line represents the region for pure oscillation while the dashed line represents the region for oscillation with decay in vacuum. This region uses the data from ν_μ and $\bar{\nu}_\mu$ events. (b) Our contour plot for the 90% CL region for the same set of parameters, considering only the presence of ν_μ events, with the solid line representing the pure oscillation and the dashed line the pure oscillation with decay in vacuum.

Figure 5.10 show us the 2D 90% CL region for the parameters Δm^2_{32} and $\sin^2\theta_{23}$. In this plot, our region for the pure oscillation matches within reasonable agreement with the one in the referece. The decay region has the same effect of enlarging the right and lower regions, but with a bigger intensity.

This effect of the enlargment of the area is expected. If we consider a simpler model of 2 neutrino oscillations for ν_μ and ν_τ, and assume a limiting case of $\Delta m^2_{32} \to 0$, where the oscillations are only induced by decay, we arrive at [1]:

$$P_{\nu_\mu \to \nu_\mu} = \left[\cos^2\theta_{23} + \sin^2\theta_{23} e^{-\frac{\alpha_3 L}{2E}}\right]^2. \tag{5.9}$$

This simplified model of the oscillation give us an insight in the expansion of the region, being caused by a break in the symmetry of $\cos^2\theta_{23}$ with $\sin^2\theta_{23}$ by the presence of a

complex phase that carries the decay parameter. This explains the enlargment in the sine axis, but we can also see in the mass axis the same effect. This happens if we do not consider the limiting case, and have the total probability:

$$P_{\nu_\mu \to \nu_\mu} = \left[\cos^2\theta_{23} + \sin^2\theta_{23} e^{-\frac{\alpha_3 L}{2E}}\right]^2 - 4\cos^2\theta_{23}\sin^2\theta_{23} e^{-\frac{\alpha_3 L}{2E}} \sin^2\left(\frac{\Delta m^2_{32} L}{4E}\right), \quad (5.10)$$

where we can see that there is also a presence of a complex phase in the term that has influence by the mass, allowing for the enlargment seen.

The best fit in Figure 5.10a shows two different best fit points that differ along the sine axis. The symmetric region shows the possible octants for the sine. In the reference case, pure oscillation occurs in the lower octant, whereas oscillation with decay in vacuum is in the higher octant.. In our case, within Figure 5.10b we see that both of them are in the same octant. The difference seen can easily be considered by the different data being used and methodology.

These plots, therefore, allow us to see that the effects of decay in the oscillation probability with our model are coherent, even if they are more intense than the obtained in the literature.

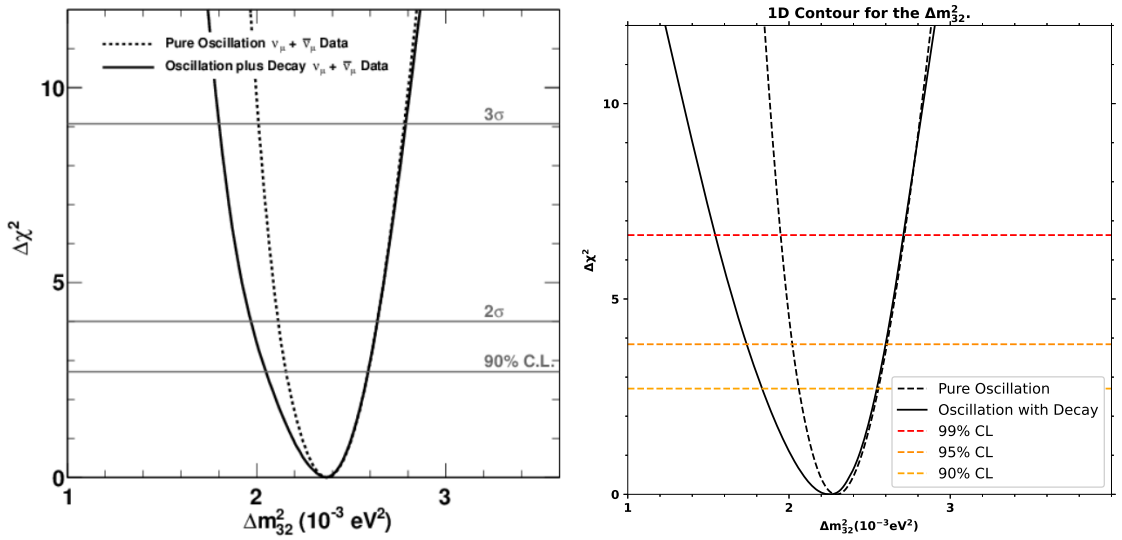

(a) **(b)**

Figure 5.11: The lines have the same caption as the Figure prior. (a) Represents the reference for the 90% CL region for the Δm^2_{32} parameter considering ν_μ and $\bar{\nu}_\mu$ events. (b) for the 90% CL region for the same parameter, considering only the presence of ν_μ events.

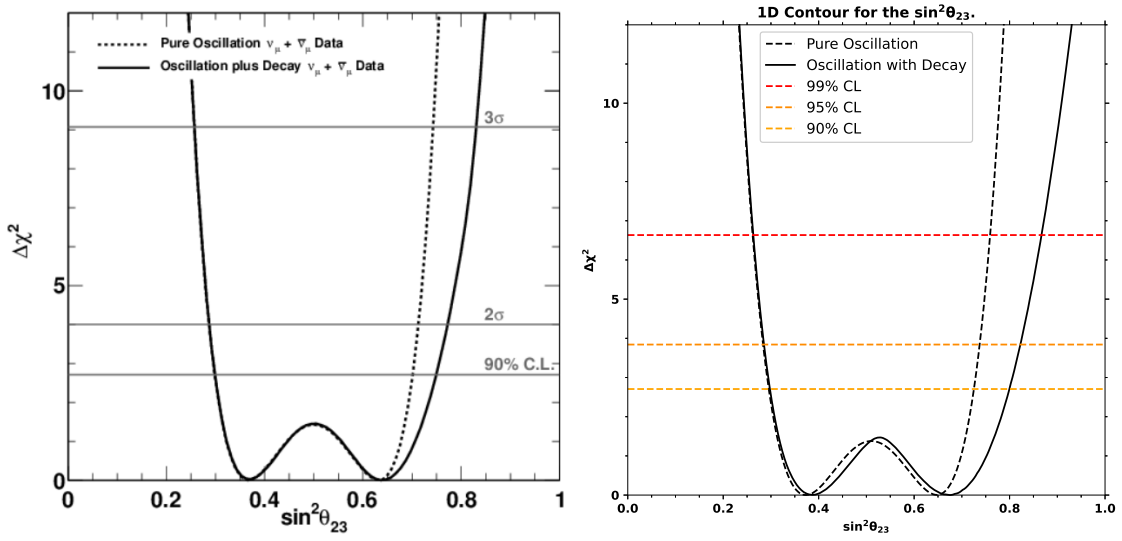

(a) **(b)**

Figure 5.12: Same caption as the Figure prior, but now for the $\sin^2\theta_{23}$ parameter.

The enlargment of the 2D region can be further confirmed by Figures 5.11 and 5.12. For the mass parameters, analysing Figures 5.11a and 5.11b we have a good agreement on the

behaviour of the oscillation with decay in vacuum probability following the left side, but having a wider gap in the right side, which implies that more values of mass are suited in the 90% CL range and being reflected in our 2D region (Figure 5.10b), explained in Eq. (5.10). For the sine, we also have the same effect of greater values of sines being allowed in the 90% CL region given to the break in symmetry showned in Eq. (5.9), we can also see that we have a shift to the right of the oscillation with decay in vacuum line with respect to the pure oscillation in Figure 5.12b that is not seen in Figure 5.12a.

Considering now the decay parameter in the form τ_3/m_3 we can see Figure 5.13. Our graph, represented in Figure 5.13b seems only shifted to the left when compared with the literature one (Figure 5.13a), which is not a major concern.

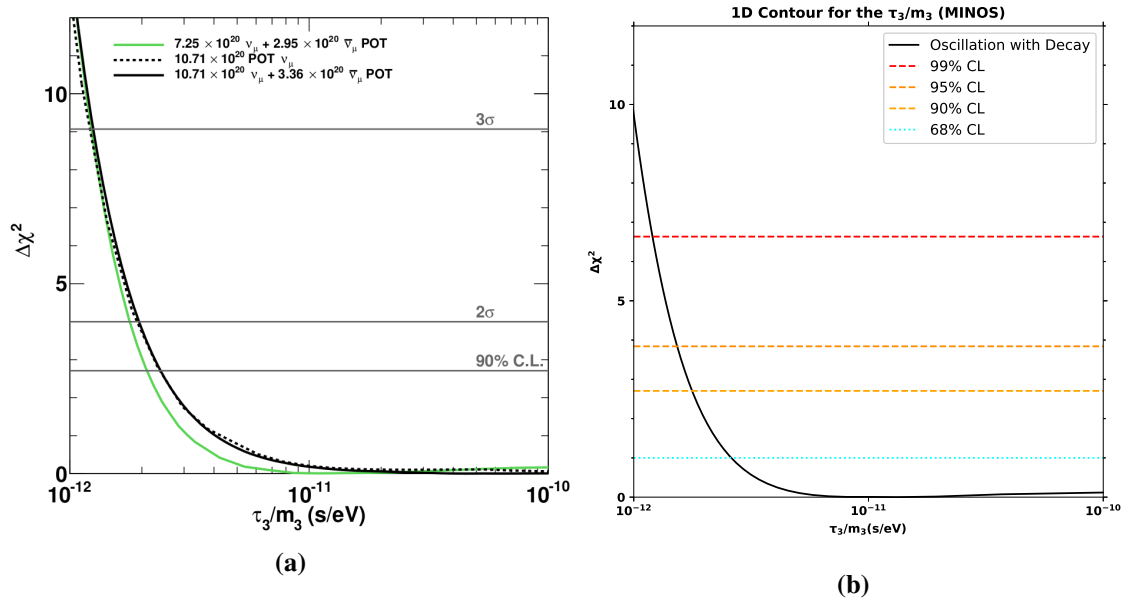

Figure 5.13: Same caption as the Figure 5.11, but now for the τ_3/m_3 parameter.

We can also compare the 90% CL limits from our analysis and the one in the literature. However, the reference does use the events from neutrinos and antineutrinos. The value reported by it is as follows:

$$\tau_3/m_3 > 2.4 \times 10^{-12}\ (s/eV), \tag{5.11}$$

while ours can be written as:

$$\tau_3/m_3 > 1.77 \times 10^{-12}\ (s/eV), \tag{5.12}$$

which is in the same order of magnitude of the presented in the reference.

The overall decay effect is present and in agreement with the literature. The different plots, as pointed in the start of this section, do have different data sets and methodology, hence, our objective was not to recreate them, but to validate if the effects of decay are in agreement. Given that they are, we will follow to the addition of the MINOS+ data and seeing how it affects the best fit and the confidence intervals.

5.2.2 MINOS+ effect in the MINOS data

The best fit obtained with both data sets can be seen in the second line of Table 5.4, while the standalone results from the MINOS are in the first line of the same table. The mass value this time is shifted to a lower value, we can also see that the angle had some influence and increased and the value for the decay parameters got lower, implying in a less strict value.

Table 5.4: Best fit values for the Δm^2_{32}, $\sin^2(\theta_{23})$, τ_3/m_3, α_3 and the lower limit of 90% CL for the τ_3/m_3 parameter, with our χ^2 and χ^2_{DF} values for the oscillation with decay in vacuum model. In the first line we have the values for our MINOS analysis (10.71×10^{20} POT ν_μ). In thse second line we have our analysis best fit values for the MINOS & MINOS+ data ($10.71 \times 10^{20} + 1.68 \times 10^{20}$ POT ν_μ)

	$\Delta m^2_{32}\ (10^{-3} eV^2)$	$\sin^2(\theta_{23})$	$\tau_3/m_3\ (s/eV)$	$\alpha_3\ (GeV/km)$	$\tau_3/m_3\ (s/eV)\ (90\%\ CL)$	χ^2	χ^2_{DF}
MINOS	$2.263^{+0.171}_{-0.250}$	$0.675^{+0.077}_{-0.099}$	1.323×10^{-11}	2.52×10^{-4}	$> 1.77 \times 10^{-12}$	11.14	$11.14/20 \sim 0.56$
MINOS & MINOS+	$2.214^{+0.192}_{-0.312}$	$0.712^{+0.069}_{-0.089}$	5.81×10^{-12}	5.74×10^{-4}	$> 1.52 \times 10^{-12}$	38.30	$38.30/60 \sim 0.64$

In Figure 5.17 we see that no major differences can be spotted in both the graphs. The more present one is simply the bottom part becoming more smooth and taking a larger area, suggesting that the addition of this data set increased the mass region instead of restraining

it. We can also consider that the best fit point got slightly shifted, but this is not one big discrepancie.

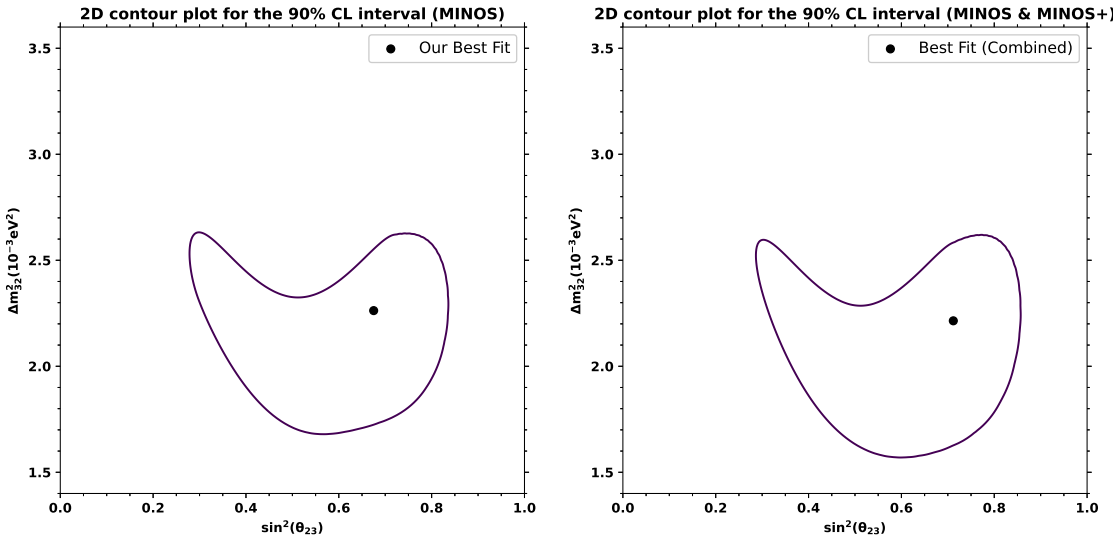

(a) **(b)**

Figure 5.14: (a) Contour plot for the 90% CL region for the Δm^2_{32} with respect to $\sin^2\theta_{32}$ using the MINOS data set. (b) The same contour plot now considering the MINOS and MINOS+ data set.

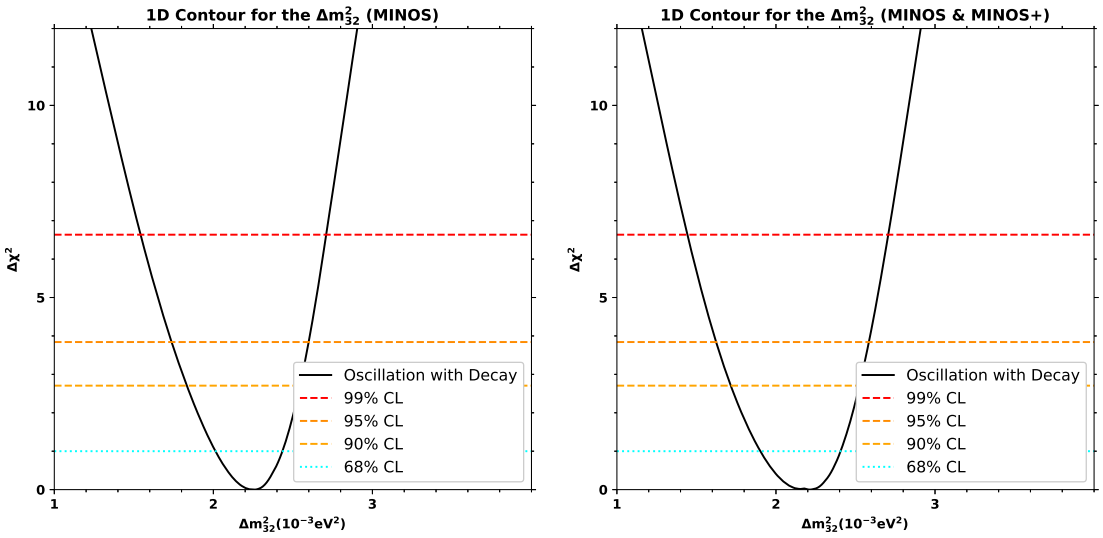

(a) **(b)**

Figure 5.15: (a) 1D contour plot for the marginalization of the Δm^2_{32} parameter using the MINOS data set. (b) The same contour plot now considering the MINOS and MINOS+ data set.

From Figure 5.15 the effect on the mass can be observed, the graph still retains the expected shape, however, we can see by it an increase in the width. If we consider the MINOS best fit with 90% CL interval, we arrive at (the square mass values are in $10^{-3}eV^2$):

$$1.833 < \Delta m^2_{32} < 2.544, \tag{5.13}$$

the addition of the MINOS+ data set increases this interval as follows:

$$1.716 < \Delta m^2_{32} < 2.525, \tag{5.14}$$

the total increase in the width is of 0.098 (eV^2). This suggests that the presence of the MINOS+ data shifts our best fit value in 0.049 (eV^2) and does not constrain the value.

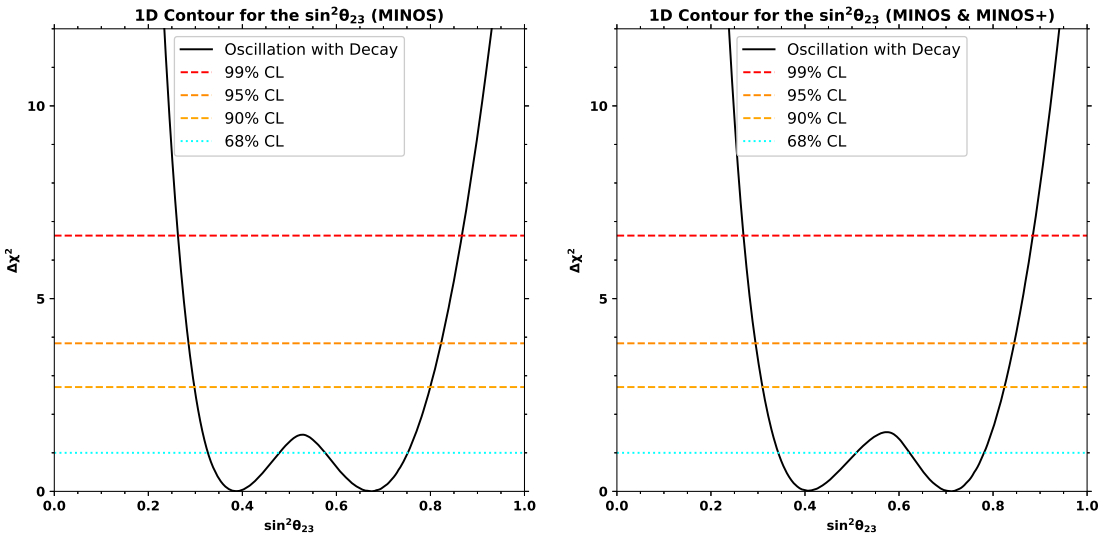

(a) **(b)**

Figure 5.16: Same caption as the Figure prior, but now considering the $\sin^2\theta_{23}$ parameter.

The sine also has some influence with the presence of the data set. Looking at Figure 5.16b we can see that the local maximum close to 0.6 is more asymmetric than the in Figure 5.16a. Considering the best fit values of the MINOS data set and the 90% CL region,

we have the following:

$$0.298 < \sin^2(\theta_{23}) < 0.8, \tag{5.15}$$

considering the effect of the MINOS+, the value then becomes:

$$0.31 < \sin^2(\theta_{23}) < 0.824, \tag{5.16}$$

again, we have a shift of the angle best fit value of 0.037 and an increase of 0.013 in the width of the graph for the 90% CL interval. This shows that there is no further restriction of the sine value and a best fit value that strays away from the literature expected for the higher octant.

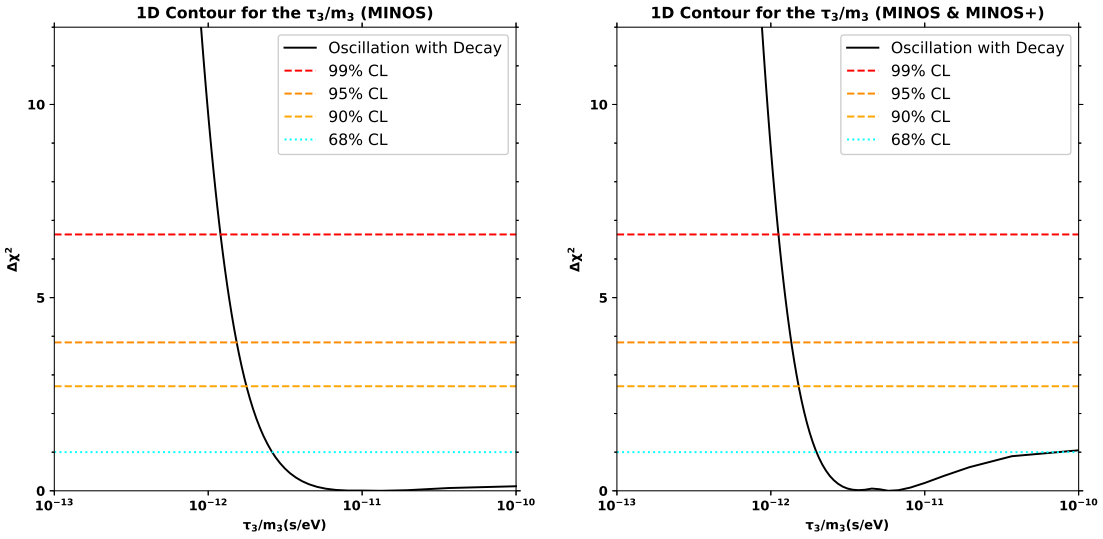

(a) **(b)**

Figure 5.17: Same caption as Figure 5.15, but now for the τ_3/m_3 parameter.

We can now take a look into the decay parameter τ_3/m_3 which does have a more significant impact in its value. The best fit value for the MINOS analysis is of:

$$\tau_3/m_3 = 1.323 \times 10^{-11}\ (s/eV), \tag{5.17}$$

while for the combined data we have:

$$\tau_3/m_3 = 5.81 \times 10^{-12}\ (s/eV), \tag{5.18}$$

one order of magnitude lower than the prior value. Hence, the addition of the MINOS+ data did not help in the restraining of this parameter, which is not as expected. Looking to Figure 5.17b we can also see that the tail of the graph has a subtle increase that does cross the 68% CL interval, not expected as seen in Figure 5.17a.

However, the 90% CL limit obtained does not diverge as the best fit value, the MINOS analysis give us an lower bound of:

$$\tau_3/m_3 > 1.77 \times 10^{-12}\ (s/eV), \tag{5.19}$$

while the combined values give us:

$$\tau_3/m_3 > 1.52 \times 10^{-12}\ (s/eV), \tag{5.20}$$

This best fit is in agreement with the expected of LBL experiments that usually have an lower bound in this order of magnitude $\left(10^{-12}\right)$ [5, 44].

5.2.3 Analysis of the results

As presented, the MINOS+ experiment did not yield great results when compared with the MINOS experiment. Only improving the value of the Δm^2_{32} value in the standard oscillation model and, in the oscillation with decay in vacuum models, not improving any of the parameters. Here, we will do a correlation of why this was the influence of the data set.

First, we need to understand where the experiment has most of its events. In Figure 5.18a the maximum of events is in the 0-4 GeV region, getting less events as the energy increases. Meanwhile, the MINOS+ experiment has its peak in around of 4-6 GeV.

In Chapter 3.1 it is stated that the MINOS experiment runned in lower energies while the MINOS+ experiment went to higher ones. So the events are in total agreement with what was proposed of the experiments. However, we also need to take into consideration how the probability behaves in different energies and with some α_3 parameters to see the same for the decay model.

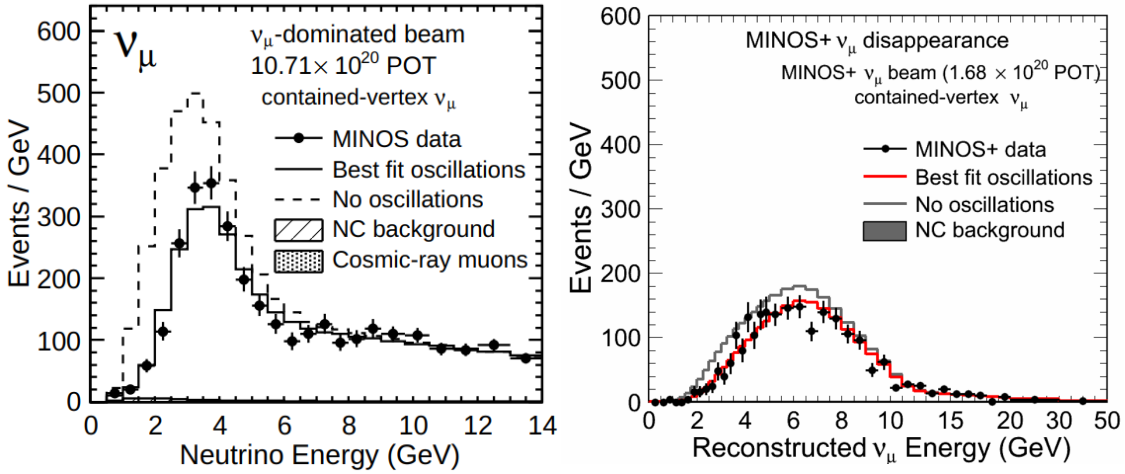

(a) **(b)**

Figure 5.18: (a) Histogram of the reconstructed events in function of the neutrino energy for the MINOS experiment. (b) Histogram of the reconstructed events in function of the neutrino energy for the MINOS+ experiment.

Figure 5.19 shows the effect of the neutrino energy for the probability. In the point where the energy is about 1 *GeV* (see Figure 5.19a) we can see a maximum in the probabilities, the lower the value of τ_3/m_3 the bigger the divergency of the graphs. In higher values of energy (Figure 5.19b) this divergency of the probability starts to get less noticeable.

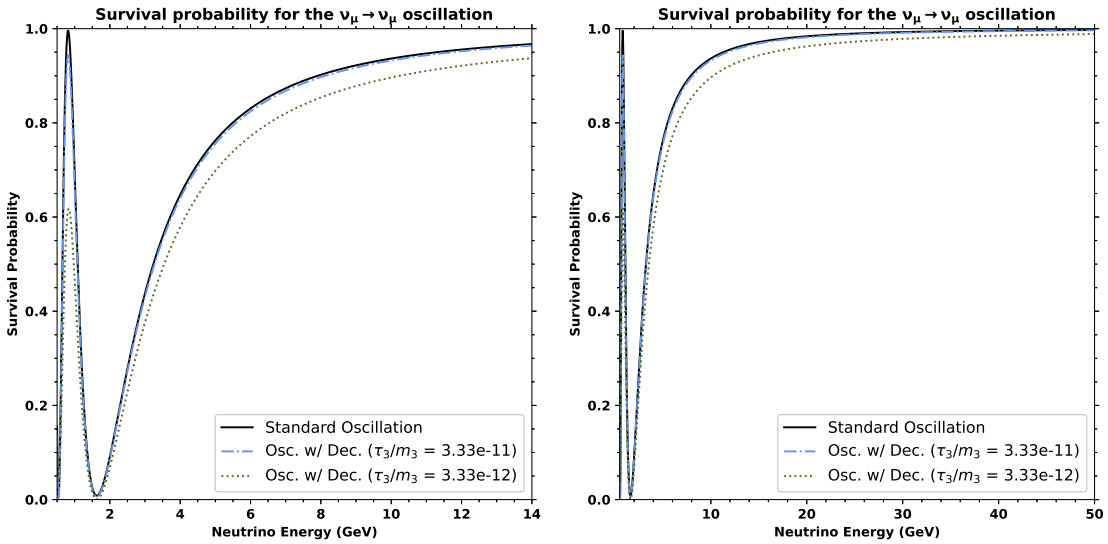

(a) **(b)**

Figure 5.19: (a) Survival probability for the ν_μ oscillation assuming different values of τ_3/m_3, the standard oscillation case is represented by the solid black line, meanwhile, the case for $\tau_3/m_3 = 3.33 \times 10^{-11}\ s/eV$ is represented by the blue dashed line and the case for $\tau_3/m_3 = 3.33 \times 10^{-12}\ s/eV$ with the red dotted line. Showing the probability as the energy increases within a low energy interval (b) We have the same graph as in case (a), but now considering higher energies.

With these graphs, we can then see that the reason the MINOS+ did not improve as much the standard oscillation case and the oscillation with decay in vacuum model. The region with higher sensitivity for this oscillation lies in the low energy spectra. Meanwhile, the events that MINOS+ provide are within the medium to high energy spectra. This comes to show that, for the case of $\nu_\mu \to \nu_\mu$ oscillation, the use of events of higher energy, even being more statistics, may not cause a good improvement in the results.

5.3 Oscillation with decay in matter

5.3.1 Numerical and analytical validation

In this section we seek to validate the numerical and analytical approaches for the oscillation with decay in matter model. The numerical approach will be the same as done by

Denton & Parke [76], and the analytical approach will be the series expansion from *Grönroos et al.* [3].

As a proof of concept, the computations are going to be made with the analytical formula. Another point to consider, is that we do not expect the matter effects to enhance any of our results so far, given that, for matter effects to have any implications with experiments on Earth, the neutrino flavor more susceptible to its influence would be ν_e, since we are studying the survival probability of ν_μ, there should be no benefit for our results.

Again, this section is to be used as a proof of concept, showing the use and possible results from the use of a more complex model that also can be useful for our analysis.

In Figure 5.20 we will see many comparisons between the analytical and numerical approaches with different values for the α_3 parameter in a "low" energy spectra (that is, until 14 GeV). Meanwhile, as for Figure 5.21d we will see the same graphs but for a "higher" energy spectra (until 50 GeV).

In the high end energy spectra, we can see that for values of $\alpha_3 \leq 10^{-4}\ GeV/km$ both functions behave with a very high agreement. If the value of $\alpha_3 \geq 10^{-3}\ GeV/km$ we can see that they do diverge in the low energy spectra and converge again for higher energies.

The step we are using for our α_3 can be seen in Table 4.3, but they start in a lower bound of $10^{-5}\ GeV/km$ and go upwards of $10^{-2}\ GeV/km$. Given that we expect our best fit to be in the order of magnitude of $10^{-4}\ GeV/km$ and our probability is not sensitive to the matter effects, we can consider them equivalent and will be using the analytical one as a proof of concept case.

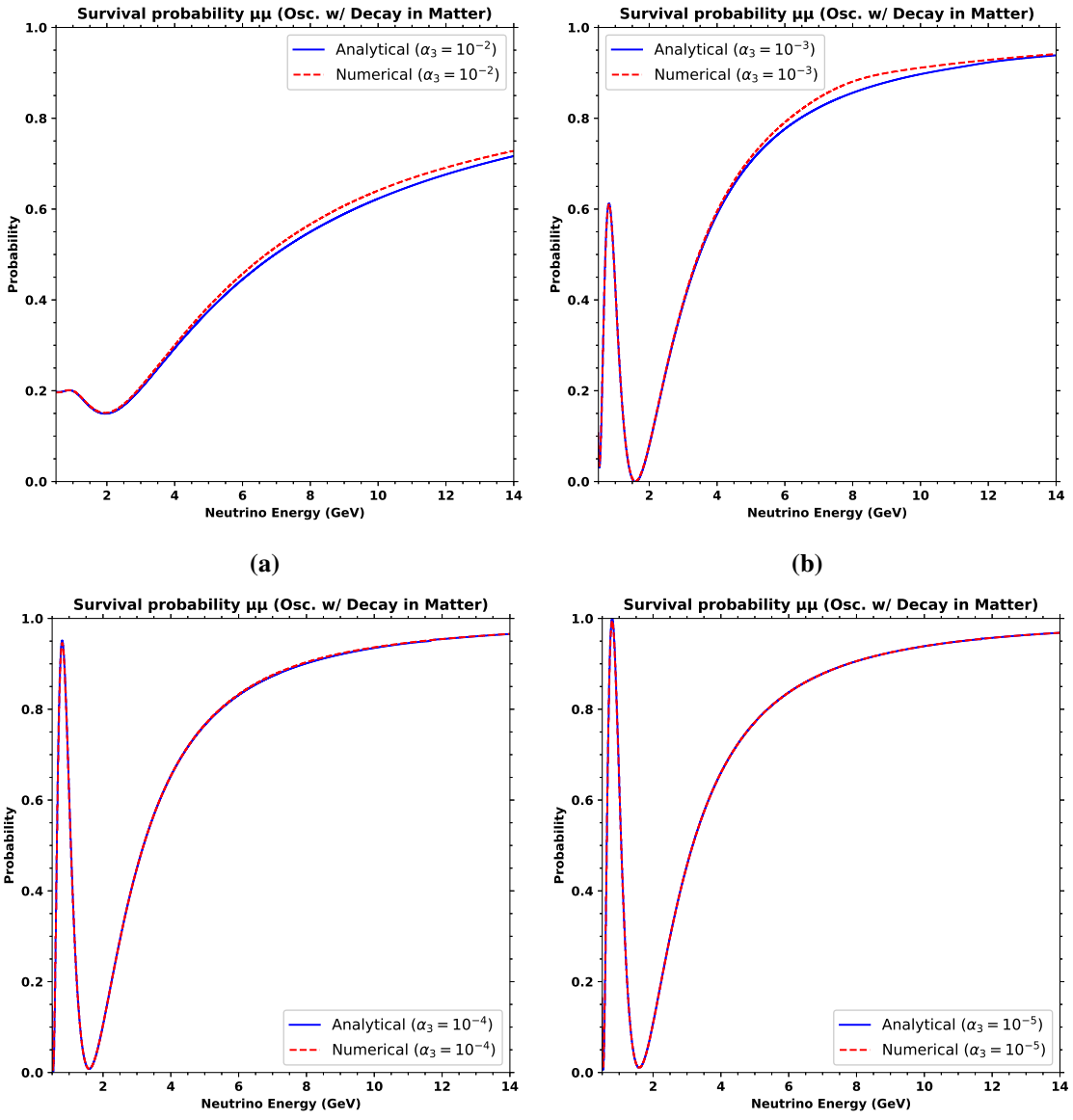

Figure 5.20: Survival probability for the ν_μ ν_μ oscillation with the numerical approach (red dashed line) and analytical approach (blue line) within the interval of 0 - 14 GeV. (a) Considering $\alpha_3 = 10^{-2}\ GeV/km$. (b) Considering $\alpha_3 = 10^{-3}\ GeV/km$. (c) Considering $\alpha_3 = 10^{-4}\ GeV/km$. (d) Considering $\alpha_3 = 10^{-5}\ GeV/km$.

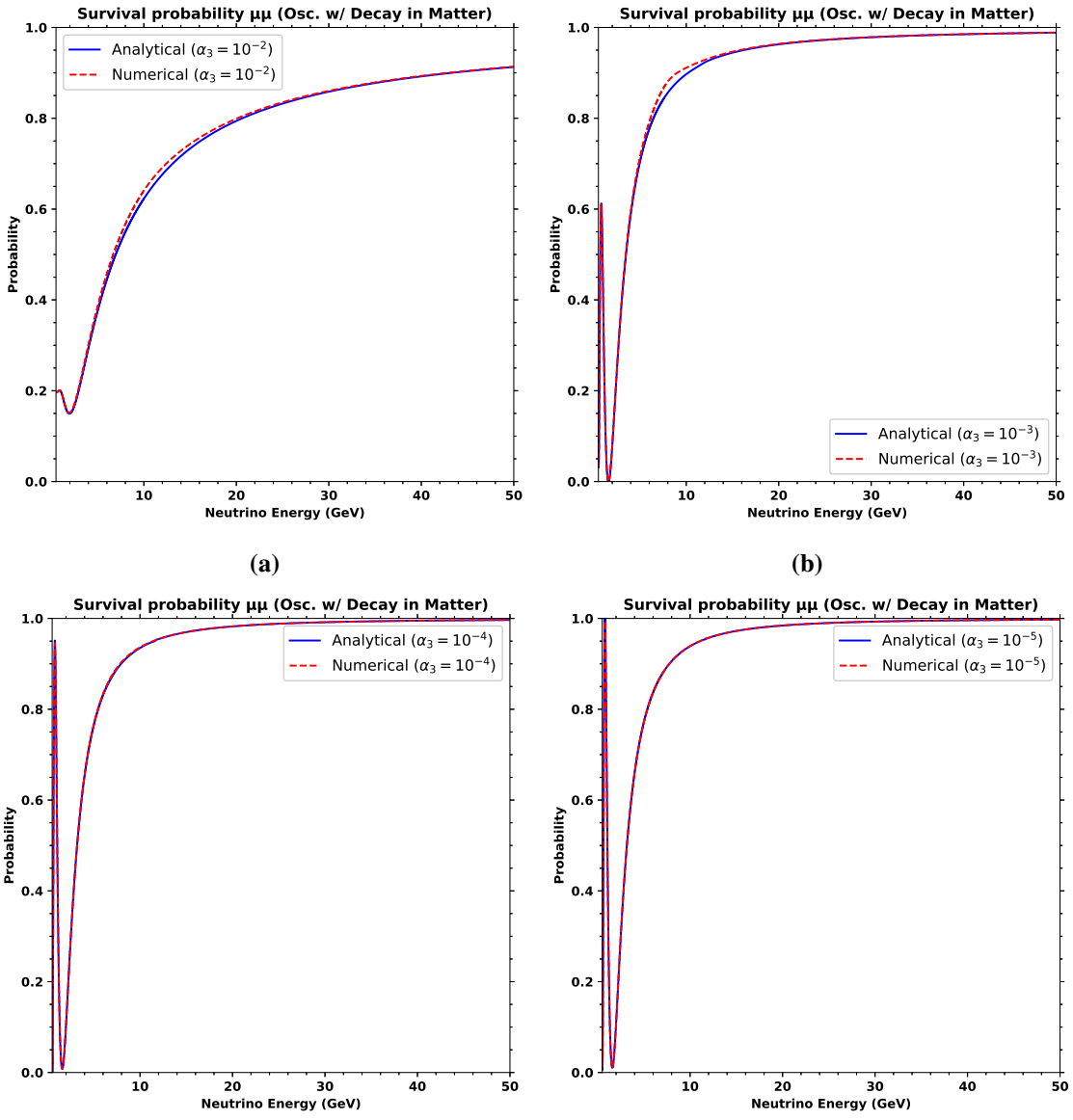

Figure 5.21: Same caption as the Figure prior, but now considering the 0 - 50 *GeV* energy interval.

5.3.2 The MINOS results

Considering the oscillation with decay in matter for the MINOS data, we arrive at the following best fit values:

Table 5.5: Best fit values for our analysis of MINOS data ν_μ (10.71×10^{20} POT) for the oscillation with decay in vacuum in model in the first line and for the oscillation with decay in matter model in the second line, for the physical parameters Δm^2_{32}, $\sin^2\theta_{23}$, τ_3/m_3, α_3 and a lower limit for the 90% CL of the τ_3/m_3 parameter.

	Δm^2_{32} $(10^{-3}eV^2)$	$\sin^2(\theta_{23})$	τ_3/m_3 (s/eV)	α_3 (GeV/km)	τ_3/m_3 (s/eV) $(90\%\ CL)$	χ^2	χ^2_{DF}
Osc. w/ Dec. in Vacuum	$2.263^{+0.171}_{-0.250}$	$0.675^{+0.077}_{-0.099}$	1.323×10^{-11}	2.52×10^{-4}	$> 1.77 \times 10^{-12}$	11.14	$11.14/20 \sim 0.56$
Osc. w/ Dec. in Matter	$2.275^{+0.167}_{-0.259}$	$0.678^{+0.098}_{-0.097}$	1.323×10^{-11}	2.52×10^{-4}	$> 1.77 \times 10^{-12}$	11.15	$11.15/20 \sim 0.56$

If we compare the first line with the second we can see that there are no major improvements for any of the parameters. We observe a negligible change in the best fit values for mass and sine, with a change in the 68% CL interval, more pronounced for sine than for mass. We also note that the decay parameter has not changed, nor has the χ^2 value

Making a comparison with the decay 2D plot, as can be seen in Figure 5.22, we can see that there are no changes in the regions, nor the best fit position.

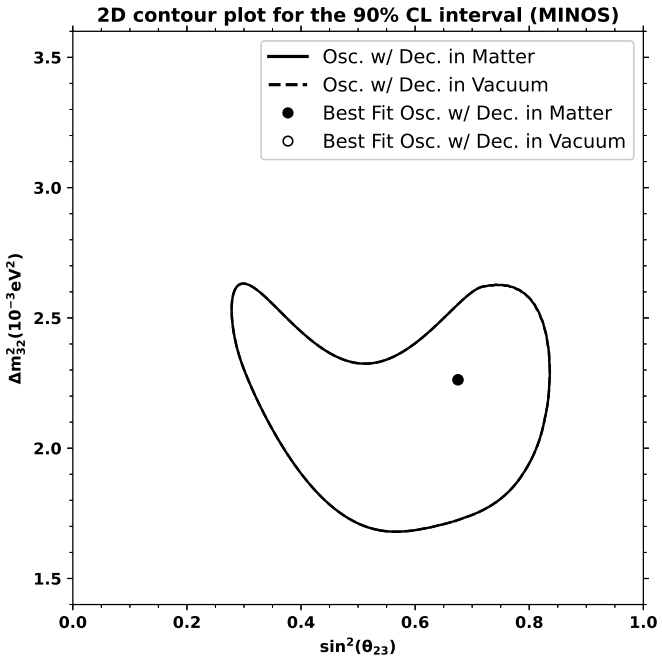

Figure 5.22: Comparison of the 2D contour plot for the 90% CL region for the Δm^2_{32} with respect to $\sin^2\theta_{23}$ using the MINOS data set in the oscillation with decay in vacuum model (dashed line), and the oscillation with decay in matter model (solid line).

For the mass parameter, we have that using the model of oscillation with decay in vacuum, the best fit for the Δm^2_{32} and the interval of 90% CL is given by Eq. (5.13) and, with matter effects we have (the square mass term is in $10^{-3}eV^2$):

$$1.833 < \Delta m^2_{32} < 2.552. \tag{5.21}$$

This shows that there is just a negligible change in the interval and a small shift in the best fit value. This can be better seen in Figure 5.23 comparing the mass 1D contour.

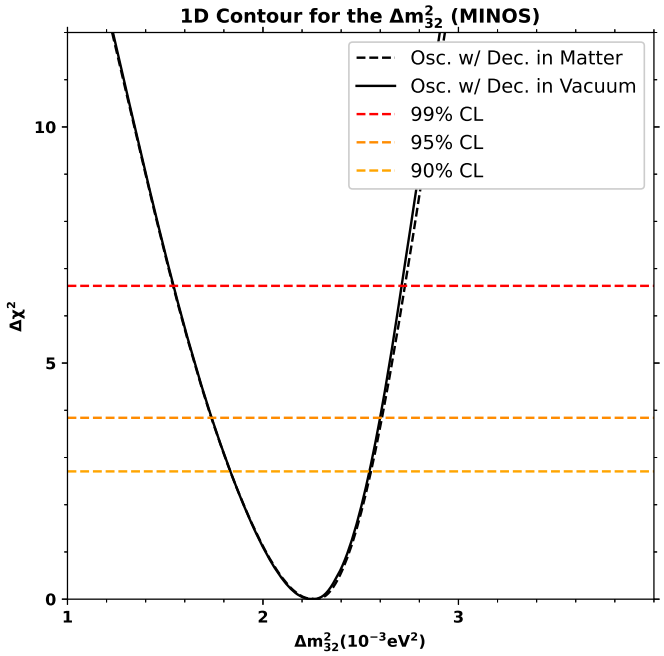

Figure 5.23: Comparison of the 1D contour plot for the Δm^2_{32} using the MINOS data set in the oscillation with decay in vacuum model (dashed line), and the oscillation with decay in matter model (solid line).

The sine parameter also has no major change, seeing Eq. (5.15) we have the best fit for the MINOS in the decay model and, adding the matter effects, we have:

$$0.298 < \sin^2(\theta_{23}) < 0.804. \tag{5.22}$$

Again, we have just negligible changes in both the interval and the best fit value. This further enhances our first guess that the matter effects would not have any great impact. The plot for the sine comparison can be seen in Figure 5.24.

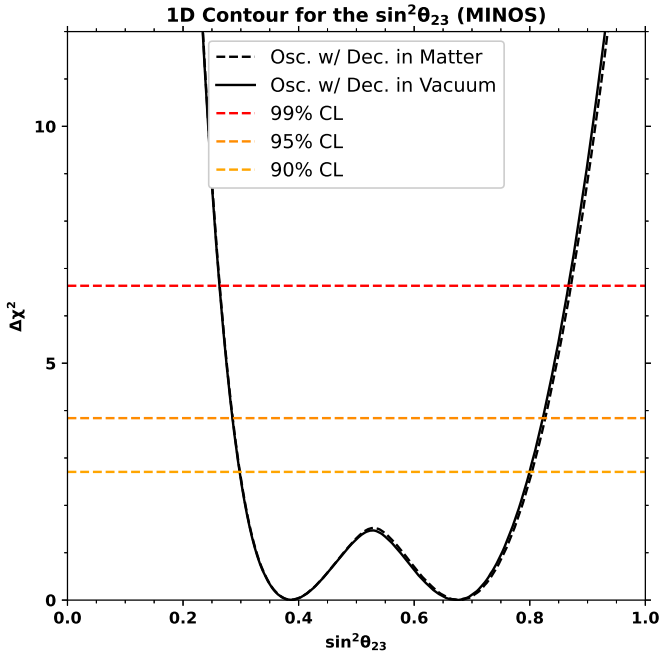

Figure 5.24: Same caption as the Figure prior, but no for the $\sin^2\theta_{23}$ parameter.

For the decay parameter τ_3/m_3 the best fit and the 90% CL lower bound are identical, the graph of the comparison (Figure 5.25) shows no divergence from the decay model in vacuum with the one in matter.

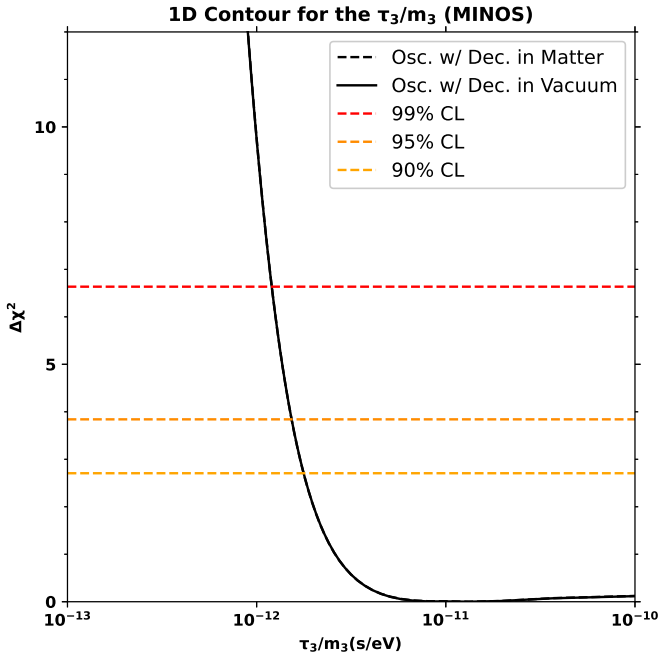

Figure 5.25: Same caption as Figure 5.23, but now for the τ_3/m_3 parameter.

The lack of any change, as commented prior, is due to the survival probability of ν_μ not being sensitive for the matter effects when considering the Earth medium.

5.3.3 The MINOS & MINOS+ results

The final set to be considered is the MINOS and MINOS+ combined results with oscillation with decay in matter being compared with the one in vacuum. We already showned that the matter effects had little effect in our MINOS results, however, these results are being made with a model that is more adequate for our scenario and, hence, the combined data set of MINOS and MINOS+ will be the one used to represent our final best fit value.

For the combined data set we can see the second line of Table 5.6 while for the MINOS standalone results we can consult the first line of the same table. We can verify once more that the mass and sine had negligible variations and the decay parameter was the same.

Table 5.6: Best fit values for the Δm^2_{32}, $\sin^2(\theta_{23})$, τ_3/m_3, α_3 and the lower limit of 90% CL for the τ_3/m_3 parameter, with our χ^2 and χ^2_{DF} values for the neutrino oscillation with decay in vacuum model in the upper half and for the neutrino oscillation with decay in matter model in the lower half. For the MINOS analysis we have 10.71×10^{20} POT ν_μ. And for the MINOS & MINOS+ data we have $10.71 \times 10^{20} + 1.68 \times 10^{20}$ POT ν_μ

	Data Set	Δm^2_{32} $(10^{-3}eV^2)$	$\sin^2(\theta_{23})$	τ_3/m_3 (s/eV)	α_3 (GeV/km)	τ_3/m_3 (s/eV) $(90\%\ CL)$	χ^2	χ^2_{DF}
Osc. w/ Dec. in Vaccum	MINOS	$2.263^{+0.171}_{-0.250}$	$0.675^{+0.077}_{-0.099}$	1.323×10^{-11}	2.52×10^{-4}	$> 1.77 \times 10^{-12}$	11.14	$11.14/20 \sim 0.56$
	MINOS & MINOS+	$2.214^{+0.192}_{-0.312}$	$0.712^{+0.069}_{-0.089}$	5.81×10^{-12}	5.74×10^{-4}	$> 1.52 \times 10^{-12}$	38.30	$38.30/60 \sim 0.64$
Osc. w/ Dec. in Matter	MINOS	$2.275^{+0.167}_{-0.259}$	$0.678^{+0.098}_{-0.097}$	1.323×10^{-11}	2.52×10^{-4}	$> 1.77 \times 10^{-12}$	11.15	$11.15/20 \sim 0.56$
	MINOS & MINOS+	$2.226^{+0.195}_{-0.322}$	$0.715^{+0.070}_{-0.087}$	5.81×10^{-12}	5.74×10^{-4}	$> 1.52 \times 10^{-12}$	38.28	$38.28/60 \sim 0.64$

We can further confirm that the 2D contour plot also had no major divergences as can be seen in Figure 5.26. We see again that both regions are the same and that the best fit points also stay in the same point.

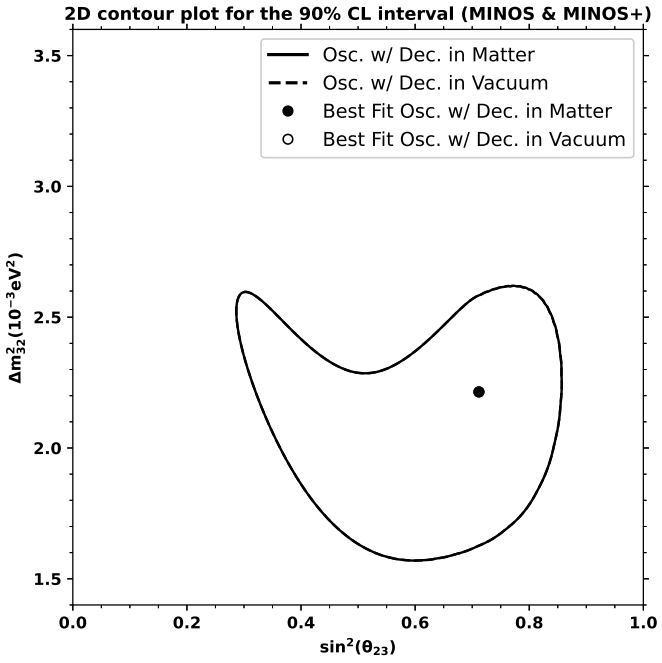

Figure 5.26: Comparison of the 2D contour plot for the 90% CL region for the Δm^2_{32} with respect to $\sin^2\theta_{23}$ using the combined MINOS and MINOS+ data set in the oscillation with decay in vacuum model (dashed line), and the oscillation with decay in matter model (solid line).

Using Figure 5.27 we can see how the matter effect changes the 90% CL interval and the best fit value for the Δm^2_{32} in $10^{-3}eV^2$:

$$1.717 < \Delta m^2_{32} < 2.54, \tag{5.23}$$

we can compare it with Eq. (5.14) to see that our best fit is again shifted slightly to the right and the interval is also increased by a small amount.

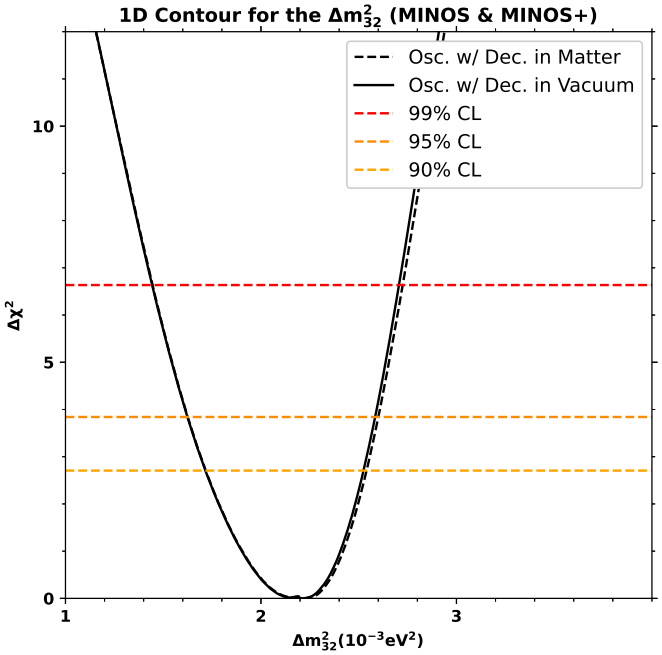

Figure 5.27: Comparison of the 1D contour plot for the Δm^2_{32} using the combined MINOS and MINOS+ data set in the oscillation with decay in vacuum model (dashed line), and the oscillation with decay in matter model (solid line).

For the sine parameter, we do not observe significant discrepancies. Considering Figure 5.28, we obtain the following best fit value and 90% CL interval:

$$0.31 < \sin^2(\theta_{23}) < 0.828, \tag{5.24}$$

and comparing this with Eq. (5.16) we see that the best fit and interval are changed in a negligible way.

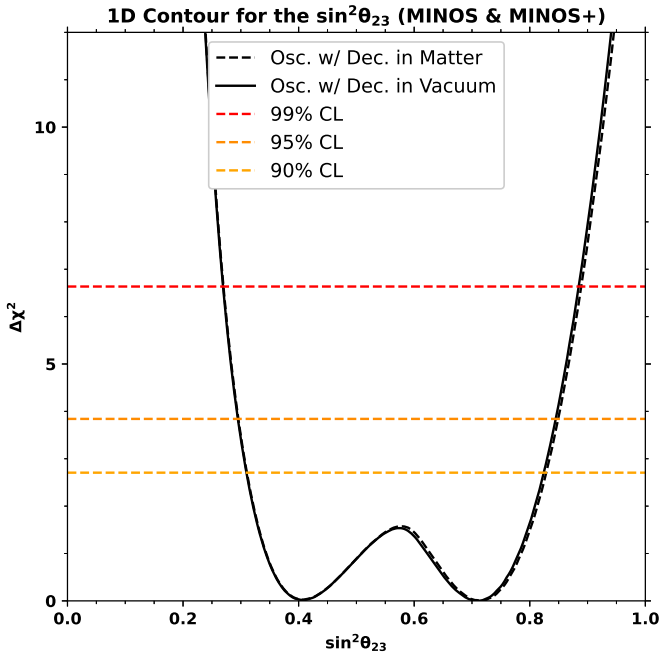

Figure 5.28: Same caption as the Figure prior, but now for the $\sin^2\theta_{23}$ parameter.

The decay parameter, τ_3/m_3, remains unchanged, as does the 90% CL lower bound. The comparison graph can be seen in Figure 5.29. Given that we expected no alteration of the best fit, we can see that there was no problem in the implementation of the probability with decay in matter.

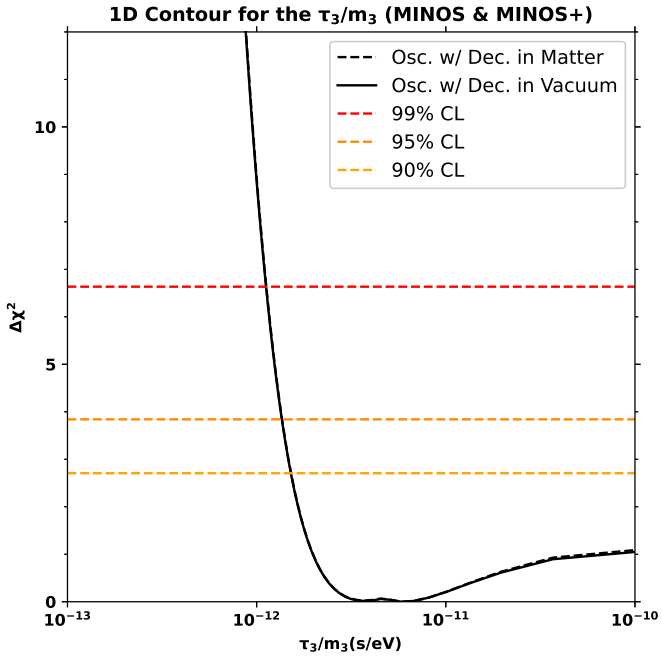

Figure 5.29: Same caption as Figure 5.27, but now for the τ_3/m_3 parameter.

Chapter 6

Conclusions and future perspectives

The work had three main objectives: to examine how the MINOS+ data would affect the MINOS free parameters in standard oscillation and oscillation with decay in vacuum; to achieve a lower bound limit for the τ_3/m_3 parameter, which is the inverse of the α_3 value; and to implement a more robust model that consider the decay phenomenon in matter.

The final table, consisting of all our best fit values can be seen in Table 6.1, condensing all of the results gathered in this work.

Table 6.1: Comparison between our analysis using different models: standard oscillation, oscillation with decay in vacuum and oscillation with decay in matter, for the MINOS and MINOS+ data sets. The values for the square mass are in $10^{-3}\ eV^2$ and the τ_3/m_3 best fit, and lower 90% CL limit, are in s/eV.

Model	Data Set	χ^2_{DF}	Δm^2_{32}	$\sin^2 2\theta_{23}$	$\sin^2\theta_{23}$	τ_3/m_3	τ_3/m_3 90%CL
Std. Osc.	MINOS	11.32/21	2.298	0.935	0.372	—	—
	MINOS & MINOS+	39.57/61	2.314	0.931	0.370	—	—
Osc. + Dec.	MINOS	11.14/20	2.263	0.878	0.675	1.323×10^{-11}	$> 1.77 \times 10^{-12}$
	MINOS & MINOS+	38.30/60	2.214	0.820	0.712	5.81×10^{-12}	$> 1.52 \times 10^{-12}$
Osc + Dec. + Mat.	MINOS	11.15/20	2.275	0.873	0.678	1.323×10^{-11}	$> 1.77 \times 10^{-12}$
	MINOS & MINOS+	38.28/60	2.226	0.815	0.715	5.81×10^{-12}	$> 1.52 \times 10^{-12}$

We have shown that the MINOS+ data contains more events within the 4 - 6 *GeV* range and that the oscillation probability, considering decay, is more sensitive at lower energies (1 - 2 *GeV*). The additional statistics were sufficient to slightly enhance the standard oscillation

mass parameter; however, they did not improve any parameters in the oscillation with decay model

The analysis allowed us to find a best fit value for τ_3/m_3 parameter, in the case of oscillation with decay in matter, we have found that this value is of $5.81 \times 10^{-12}\ s/eV$ while the 90% CL lower bound is at $> 1.52 \times 10^{-12}\ s/eV$. These values are in the agreement with the order of magnitude we expect LBL experiments to achieve.

The implementation of the matter effects in our analysis was also in agreement with expected, even if it was not capable on improve our results, it serves as a proof of concept that can be applied for other analysis.

We managed to achive our objectives, however, this work can be further improved. Other experiments can be used to see how they influence the MINOS data set, given that higher energies do not yield better results, experiments that are in the lower spectra can be investigated. A better value of the τ_3/m_3 can also be achieved, by considering the use of atmospheric neutrinos, as was done by *Gonzalez-Garcia & Maltoni* [6] to have a good impact in this parameter, with also considering other LBL experiments within the lower energy spectra. Finally, the matter effects can be better investigated by consider events of neutral current or, in the case of MINOS, considering also the probability apperance of ν_e.

Appendix A

Data extraction

A.1 Graph calibration

The data extraction starts with a histogram as the one that can be seen in figure A.1 and that will be used in this analysis. The histogram is composed of bins, which are the vertical bars in it. It should also be noticed that all the bins take a certain interval of energy, while the data points will always be in the average energy of the bin.

It is needed a tool for the data extraction and, for this work, we have used the *WebPlot-Digitizer*, however, other tools such as *G3Data Graph Analyzer* can also be used.

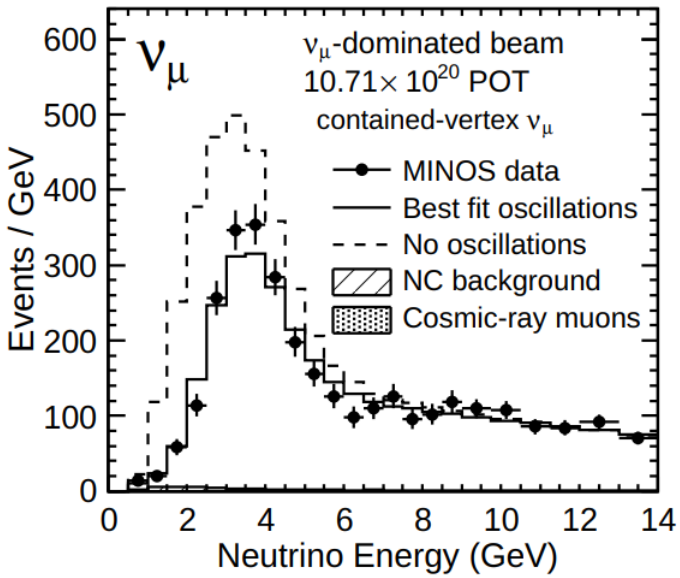

Figure A.1: Number of events as a function of the reconstructed ν energy for the 2013 analysis of MINOS [77].

This tool being used has an online version which was the one used. When we load into the site, we will be grated by a generic graph. Our first step is to select the the image we want to work, this can be done by selecting “Load Image” in the right or, in the top right corner,

selecting the "Image" tab and the same option there. Once we load the image, a window will show up with several options. For all of the histograms, we have used the *2D (X-Y) Plot* extraction method.

Once this is done, we must calibra the axis by first selecting the pair of (X_1, X_2) and (Y_1, Y_2). The X axis indicates the energy, and the Y axis will indicate the events. In some graphs, such as the one in A.1, it is normal to find the events in different units, such as events per GeV or even events per a quantity of GeV, such as $0.1GeV$, if the events are in correlation with the energy, it must be converted to just the events for the calculations, but, for reconstructions, must be in the same units of the original graph. After these points are selected, we should have something close to Figure A.2.

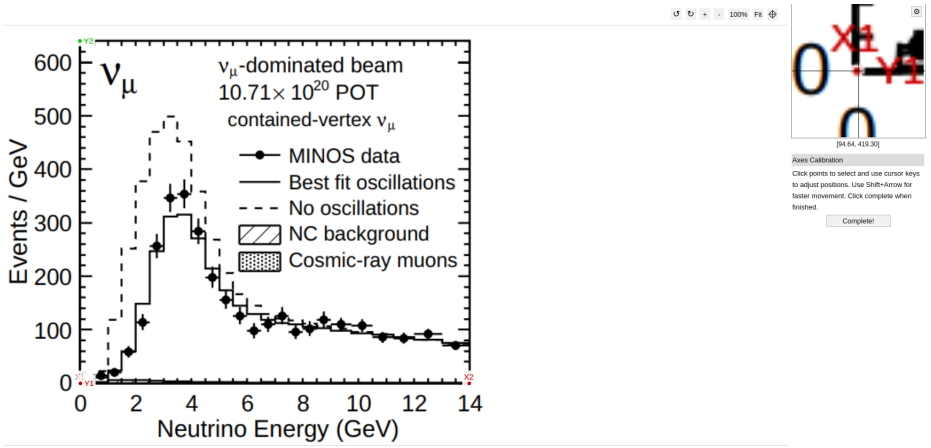

Figure A.2: Demonstration of the the axis calibration. We can see in the left image the graph with red points denoted as X_1 and X_2 as well as green points denoted as Y_1 and Y_2 showing the boundries of the graph. In the right, we can see a zoom region showing the X_1 and Y_1 points with more detail. We can also see a button of "Complete" below the zoom region, which will take us to the second part of the calibration.

We consider that the real value of the events are in the middle of the line, such that when we select the points for the axis, we try to find the middle of the vertical and horizontal lines. It is not wrong to select the edges of the lines, however, if this is done a correction must be applied in the extracted values such that you will have the "original" value (this value can be

found by seeing if all the lines have the same thickness and subtracting half of its value from the exctracted one).

With the points now setted, it can be seen a "Complete" button below the zoom zone, as described and seen in Figure A.2. This button must be pressed to confirm we have the points in the right position and go to the second part of the calibration. Once done, a window will show up as can be seen in Figure A.3.

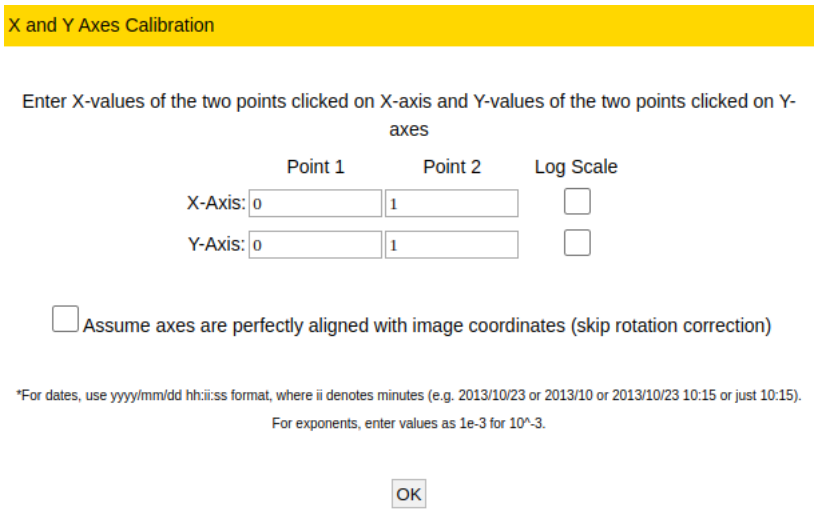

Figure A.3: A window showing the next part of the calibration, consisting in defining the points that were placed. In the first line you can define the region of the X axis and if it is in log scale, the same can be seen below for the Y axis, finally, you can apply a rotation correction.

In this new window, we must define the interval of energy and events. If the graph is in a log scale, it can be selected as such. We also assume that the axes are perfectly aligned, not needing a rotation correction. Once this is done, the graph is calibrated.

A.2 Data extraction

The axes are now calibrated and the data extraction can be done. We have three different quantities represented in the graph that require their own approach. We have the oscillations and no oscillation lines, we also have the data points, and the error bars.

If we want to extract the values of the oscillation and no oscillation lines, the same process for the axes calibration must be done. That is, to extract the point in the center of the line. This can be seen in Figure A.4a.

The extraction of the error bars are done in a different manner, we will define the point in the end of the horizontal (energy error bar) or vertical (events error bar) bars to be our data. Figure A.4b shows this.

Finally, the real data points, are consider to be the ones in the center of the black dot. To be certain that we are in the center of the point, we can take into consideration that this data point is in the central energy of the bin. Therefore, we can use the energy axis as a guide and, if further help is needed, use the error bars to center it. In Figure A.4c we can see this process.

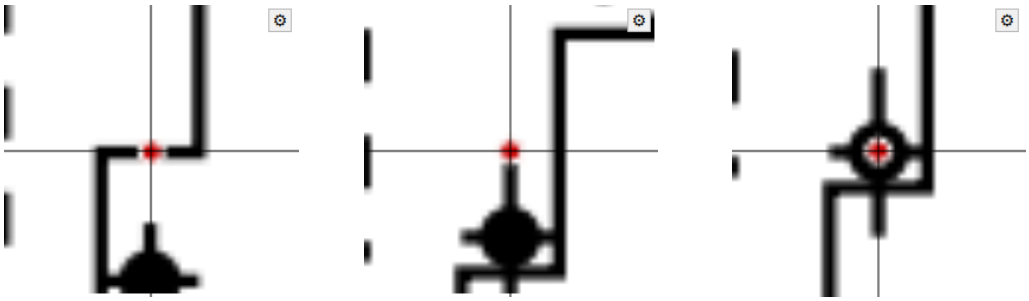

(a) **(b)** **(c)**

Figure A.4: (a) Representation of where the point of extraction must be to the oscillation and no oscillation lines. (b) Demonstration of extraction for error bars, in this case, representing the extraction of the up error bar, the extraction is made in the end of the bars. (c) Extraction of data points, being in its center to consider the "real" value.

The extractions must be done one at a time. Once the points have been selected, they can be downloaded into a *.CSV* file. The data is then cleaned and the process repeats itself for the next set of points. All of the set of points are extracted using the same axes calibration.

For the MINOS+ histogram it is needed to take into account that the energy axis was not linear nor logarithm. The graph was divided into regions where the energy behaved linearly,

afterwards, the points were extracted and combined so the reconstruction could be done. The histogram can be seen in Figure A.5.

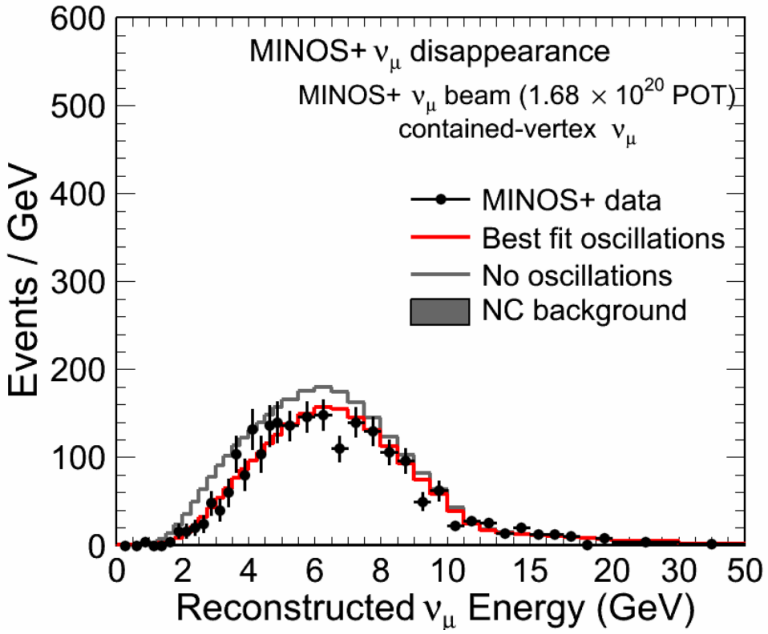

Figure A.5: Number of events as a function of the reconstructed ν_μ energy for the analysis of MINOS+ [36].

Given that the MINOS+ histogram had different regions, the final step was to combine all of the extracted points into one *.CSV* file.

Appendix B

χ^2 Distribution

The theoretical model is already stablished and can be seen in Eq. (4.2). However, we still want to see how well the predicted values of our probability are in agreement with the observed data. For this, we will need to consider a function that correlates a model with the real data and verifies if they are both in agreement. This function that we are going to use is the χ^2 function.

This function can be defined as follows:

$$\chi^2(x_1,\cdots,x_N) = \sum_{i=1}^{n} \left[\frac{N_{theo,i} - N_{data,i}}{\sigma_{tot,i}} \right]^2, \tag{B.1}$$

this function takes into consideration the theoretical model, which implies that our probability is being taken into account. The probability has free parameters, denoted as the $(x_1,\cdots,x_N)$ notation, where each x_i represents one of these parameters. We wish to find the set of parameters that will give us a minimum value for the χ^2 function, which is the one with the best correlation and, therefore, our best fit.

The function also contains a sum, the number of terms in the sum (n) is defined as the number of bins the histogram has. Given that we are going to apply our model in each bin individually to try and recreate them, we need to take into consideration their influece. This will guarantee that we are taking all the values and, given that we expect our distribution to have an average value, to be found within the standard deviation interval of it.

Besides the presence of our model, the real data, the bins and the free parameters, we also need to take into consideration our errors. The total value of the error can be represented as

follows:

$$\sigma_{tot} = \sqrt{\sigma_{data}^2 + \sigma_{sys}^2 + \sigma_{stat}^2}, \tag{B.2}$$

It is also important to consider that, our confidence levels considers a Gaussian distribution. In Figure B.1 we can see some χ^2 distributions for different number of events:

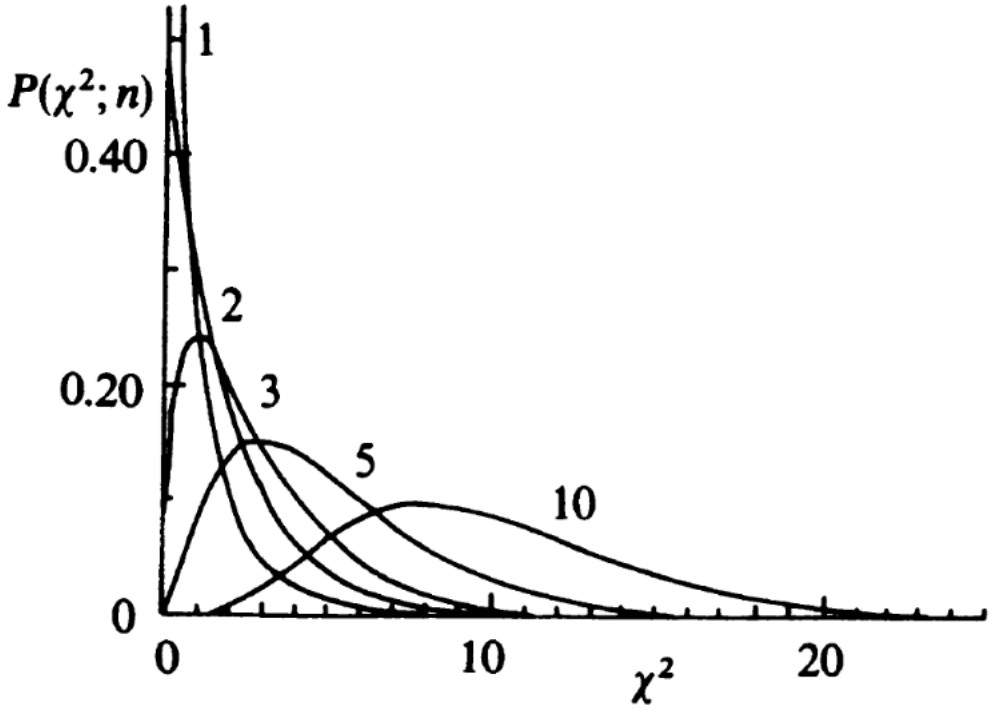

Figure B.1: Different χ^2 distributions for the values of $n = 1, 2, 3, 5$ and 10 [78].

$$P(\chi^2, D) = \frac{2^{-D/2}}{\Gamma(D/2)} \chi^{D-2} e^{-\chi^2/2}, \tag{B.3}$$

where Γ is the Gamma function and D is the degrees of freedom.

If the number of events is high, that is, $n \geq 10$ we already have a distribution close to a Gaussian. This ensures that we can use the χ^2 function istead of a different one for our confidence intervals.

Bibliography

[1] Gomes, R.; Gomes, A.; Peres, O. Constraints on neutrino decay lifetime using long-baseline charged and neutral current data. *Phys. Lett. B* **2015**, *740*.

[2] Choubey, S.; Ghosh, M.; Kempe, D.; Ohlsson, T. Exploring invisible neutrino decay at ESSnuSB. *JHEP* **2021**, *05*, 133.

[3] Grönroos, J.; Ohlsson, T.; Vihonen, S. Revisiting series expansions of neutrino oscillation and decay probabilities in matter. *Phys. Rev. D* **2025**, *111*, 035003.

[4] Choubey, S.; Dutta, D.; Pramanik, D. Invisible neutrino decay in the light of NOvA and T2K data. *JHEP* **2018**, *2018*.

[5] Adamson, P. et al. Search for sterile neutrino mixing in the MINOS long-baseline experiment. *Phys. Rev. D* **2010**, *81*, 052004.

[6] Gonzalez-Garcia, M.; Maltoni, M. Status of Oscillation plus Decay of Atmospheric and Long-Baseline Neutrinos. *Phys. Lett. B* **2008**, *663*, 405–409.

[7] Aiello, S. et al. Probing invisible neutrino decay with KM3NeT/ORCA. *JHEP* **2023**, *2023*.

[8] Choubey, S.; Goswami, S.; Gupta, C.; Mohan, L.; Thakore, T. Sensitivity to neutrino decay with atmospheric neutrinos at the INO-ICAL detector. *Phys. Rev. D* **2018**, *97*, 033005.

[9] Abrahao, T.; Minakata, H.; Nunokawa, H.; Quiroga, A. Constraint on Neutrino Decay with Medium-Baseline Reactor Neutrino Oscillation Experiments. *JHEP* **2015**, *2015*.

[10] Ghoshal, A.; Giarnetti, A.; Meloni, D. Neutrino invisible decay at DUNE: a multi-channel analysis. *J. Phys. G* **2021**, *48*, 055004.

[11] Choubey, S.; Ghosh, M.; Kempe, D.; Ohlsson, T. Exploring invisible neutrino decay at ESSnuSB. *JHEP* **2021**, *2021*.

[12] Tang, J.; Wang, T.-C.; Zhang, Y. Invisible neutrino decays at the MOMENT experiment. *JHEP* **2019**, *2019*.

[13] Chadwick, J. The intensity distribution in the magnetic spectrum of beta particles from radium (B + C). *Verh. Phys. Gesell.* **1914**, *16*, 383–391.

[14] Pauli, W. Dear radioactive ladies and gentlemen. *Phys. Today* **1978**, *31N9*, 27.

[15] Chadwick, J. Possible Existence of a Neutron. *Nature* **1932**, *129*, 312.

[16] Cowan, C. L.; Reines, F.; Harrison, F. B.; Kruse, H. W.; McGuire, A. D. Detection of the free neutrino: A Confirmation. *Science* **1956**, *124*, 103–104.

[17] Reines, F.; Cowan, C. L. The neutrino. *Nature* **1956**, *178*, 446–449.

[18] Gomes, A. L. G. Decoerência quântica em neutrinos de aceleradores. Ph.D. thesis, Goiás Federal U., 2019.

[19] Gomes, L. R. P. Sensitivities to neutrino non-standard interactions from the disappearance of muon (anti)neutrinos at the NOvA experiment. M.Sc. thesis, Goiás Federal U., 2019.

[20] Franklin, A. Is Seeing Believing?: Observation in Physics. *Phys. Perspect.* **2017**, *19*.

[21] Danby, G.; Gaillard, J. M.; Goulianos, K. A.; Lederman, L. M.; Mistry, N. B.; Schwartz, M.; Steinberger, J. Observation of High-Energy Neutrino Reactions and the Existence of Two Kinds of Neutrinos. *Phys. Rev. Lett.* **1962**, *9*, 36–44.

[22] Perl, M. L. et al. Evidence for Anomalous Lepton Production in $e^+ - e^-$ Annihilation. *Phys. Rev. Lett.* **1975**, *35*, 1489–1492.

[23] Kodama, K. et al. Final tau-neutrino results from the DONuT experiment. *Phys. Rev. D* **2008**, *78*, 052002.

[24] Bahcall, J. N.; Pinsonneault, M. H.; Basu, S. Solar Models: Current Epoch and Time Dependences, Neutrinos, and Helioseismological Properties. *Astrophys. J.* **2001**, *555*, 990.

[25] Vitagliano, E.; Redondo, J.; Raffelt, G. Solar neutrino flux at keV energies. *J. Cosmol. Astropart. Phys.* **2017**, *2017*, 010.

[26] Cleveland, B. T.; Daily, T.; Raymond Davis, J.; Distel, J. R.; Lande, K.; Lee, C. K.; Wildenhain, P. S.; Ullman, J. Measurement of the Solar Electron Neutrino Flux with the Homestake Chlorine Detector. *Astrophys. J.* **1998**, *496*, 505.

[27] Suzuki, Y. Kamiokande-II results on solar neutrinos and the Super-Kamiokande experiment. 11th Moriond Workshop: Tests of Fundamental Laws in Physics. 1991; pp 427–435.

[28] Boger, J. et al. The Sudbury Neutrino Observatory. *Nucl. Instrum. Methods Phys. Res. A* **2000**, *449*, 172–207.

[29] Ianni, A. Solar neutrinos and the Solar Model. *Phys. Dark Universe* **2014**, *4*.

[30] Ahmad, Q. R. et al. Direct Evidence for Neutrino Flavor Transformation from Neutral-Current Interactions in the Sudbury Neutrino Observatory. *Phys. Rev. Lett.* **2002**, *89*.

[31] Pontecorvo, B. Inverse beta processes and nonconservation of lepton charge. *Zh. Eksp. Teor. Fiz.* **1957**, *34*, 247.

[32] Maki, Z.; Nakagawa, M.; Sakata, S. Remarks on the unified model of elementary particles. *Prog. Theor. Phys.* **1962**, *28*, 870–880.

[33] Giganti, C.; Lavignac, S.; Zito, M. Neutrino oscillations: The rise of the PMNS paradigm. *Prog. Part. Nucl. Phys.* **2018**, *98*, 1–54.

[34] Pontecorvo, B. Neutrino Experiments and the Problem of Conservation of Leptonic Charge. *Zh. Eksp. Teor. Fiz.* **1967**, *53*, 1717–1725.

[35] Giunti, C.; Wook, K. C. *Fundamentals of Neutrino Physics and Astrophysics*; Oxford Univ.: Oxford, 2007.

[36] Medeiros, M. M. Estudo da oscilação de neutrinos muônicos usando dados atmosféricos e de acelerador nos experimentos MINOS e MINOS+. Tese de doutorado, Universidade Federal de Goiás, Goiânia, Brasil, 2015.

[37] Griffiths, D. J. *Introduction to elementary particles; 2nd rev. version*; Physics textbook; Wiley: New York, NY, 2008.

[38] Kraus, C.; Bornschein, B.; Bornschein, L.; Bonn, J.; Flatt, B.; Kovalik, A.; Ostrick, B.; Otten, E. W.; Schall, J. P.; Thümmler, T.; Weinheimer, C. Final results from phase II of the Mainz neutrino mass searchin tritium β decay. *Eur. Phys. J. C* **2005**, *40*, 447–468.

[39] Denton, P. B. Neutrino Oscillations in the Three Flavor Paradigm. **2025**,

[40] Lipkin, H. J. Quantum theory of neutrino oscillations for pedestrians: simple answers to confusing questions. *Phys. Lett. B* **2006**, *642*, 366–371.

[41] Pich, A. CP violation. *ICTP Ser. Theor. Phys.* **1994**, *10*, 14–42.

[42] Barger, V.; Learned, J. G.; Pakvasa, S.; Weiler, T. J. Neutrino Decay as an Explanation of Atmospheric Neutrino Observations. *Phys. Rev. Lett.* **1999**, *82*, 2640–2643.

[43] Acker, A.; Pakvasa, S.; Pantaleone, J. T. Decaying Dirac neutrinos. *Phys. Rev. D* **1992**, *45*, 1–4.

[44] GOMES, A. L. G. Limites nos parâmetros do modelo de oscilação com decaimento de neutrinos usando os dados do experimento MINOS. Dissertação (Mestrado em Física), Universidade Federal de Goiás, Goiânia, 2014.

[45] Bandyopadhyay, A.; Choubey, S.; Goswami, S. Neutrino decay confronts the SNO data. *Phys. Lett. B* **2003**, *555*, 33–42.

[46] Wolfenstein, L. Neutrino Oscillations in Matter. *Phys. Rev. D* **1978**, *17*, 2369–2374.

[47] Mikheev, S. P.; Smirnov, A. Y. Resonance Oscillations of Neutrinos in Matter. *Sov. Phys. Usp.* **1987**, *30*, 759–790.

[48] Kayser, B. Neutrino Physics. 2005; `https://arxiv.org/abs/hep-ph/0506165`.

[49] Honda, M.; Okamura, N.; Takeuchi, T. Matter Effect on Neutrino Oscillations from the violation of Universality in Neutrino Neutral Current Interactions. 2006; `https://arxiv.org/abs/hep-ph/0603268`.

[50] Ohlsson, T.; Snellman, H. Three flavor neutrino oscillations in matter. *J. Math. Phys.* **2000**, *41*, 2768–2788.

[51] Chattopadhyay, D. S.; Chakraborty, K.; Dighe, A.; Goswami, S. Analytic treatment of 3-flavor neutrino oscillation and decay in matter. *JHEP* **2023**, *2023*.

[52] Michael, D. The MINOS experiment. *Prog. Part. Nucl. Phys.* **2002**, *48*, 99–109.

[53] Adamson, P. et al. Search for Sterile Neutrinos in MINOS and MINOS+ Using a Two-Detector Fit. *Phys. Rev. Lett.* **2019**, *122*.

[54] Habig, A.; Grashorn, E. W. The MINOS Detectors. 2005; `https://arxiv.org/abs/hep-ex/0507018`.

[55] Evans, J. The MINOS experiment: results and prospects. 2013; `https://arxiv.org/abs/1307.0721`.

[56] Adamson, P. et al. The NuMI neutrino beam. *Nucl. Instrum. Methods Phys. Res. A* **2016**, *806*, 279–306.

[57] Tzanankos, G.; Bishai, M.; Diwan, M.; Escobar, C. O.; Gomes, R. A.; Gouffon, P.; Blake, A.; Thomson, M.; Patterson, R. B.; Adamson, P.; Childress, S. *MINOS+: a Proposal to FNAL to run MINOS with the medium energy NuMI beam*; 2011.

[58] Whitehead, L. Neutrino oscillations with MINOS and MINOS+. *Nucl. Phys. B* **2016**, *908*, 130–150.

[59] Timmons, A. The Results of MINOS and the Future with MINOS+. *Adv. High Energy Phys.* **2016**, *2016*.

[60] Ayres, D. S.; others., The NOvA Technical Design Report. **2007**,

[61] Syphers, M. J. An Improved 8-GeV Beam Transport System for the Fermi National Accelerator Laboratory. **1987**,

[62] The NuMI Technical Design Handbook. **2002**,

[63] Orchanian, M.-A. H. Electron Neutrino Appearance in the MINOS Experiment. Ph.D. thesis, Caltech, 2012.

[64] Zwaska, R. M. Accelerator Systems and Instrumentation for the NuMI Neutrino Beam. Ph.D. thesis, Texas U., 2005.

[65] Evans, J. J. Measuring Antineutrino Oscillations with the MINOS Experiment. Ph.D. thesis, Oxford U., 2008.

[66] Himmel, A. FHC And RHC Horn Focusing Figure - Blessing Package. NOvA Internal Document 20855. **2017**,

[67] Holin, A. M. Electron Neutrino Appearance in the MINOS Experiment. Ph.D. thesis, 2010.

[68] Michael, D. et al. The magnetized steel and scintillator calorimeters of the MINOS experiment. *Nucl. Instrum. Methods Phys. Res. A* **2008**, *596*, 190–228.

[69] Ambats, I.; Wojcicki, S. G. *The MINOS Detectors Technical Design Report*; 1998.

[70] Adamson, P. et al. Study of muon neutrino disappearance using the Fermilab Main Injector neutrino beam. *Phys. Rev. D* **2008**, *77*.

[71] Chapman, J. D. Atmospheric neutrino observations in the MINOS far detector. Ph.D. thesis, Cambridge U., 2007.

[72] Blake, A. A Study of Atmospheric Neutrino Oscillations in the MINOS Far Detector. PhD thesis, University of Cambridge, 2005.

[73] MINOS Collaboration, Observation of muon neutrino disappearance with the MINOS detectors and the NuMI neutrino beam. *Phys. Rev. Lett.* **2006**, *97*, 191801.

[74] Himmel, A. I. Antineutrino Oscillations in the Atmospheric Sector. Ph.D. thesis, California Institute of Technology, 2011.

[75] Cundiff, T.; Dawson, J.; Drake, G.; Haberichter, W.; Reyna, D. The MINOS Near Detector Front End Electronics. IEEE Nuclear Science Symposium Conference Record. 2004; pp 2227–2230.

[76] Denton, P. B.; Parke, S. J. Fast and Accurate Algorithm for Calculating Long-Baseline Neutrino Oscillation Probabilities with Matter Effects: NuFast. *Phys. Rev. D* **2024**, *110*, 073005.

[77] Adamson, P. et al. Measurement of Neutrino and Antineutrino Oscillations Using Beam and Atmospheric Data in MINOS. *Phys. Rev. Lett.* **2013**, *110*, 251801.

[78] Barlow, R. J. *Statistics: A Guide to the Use of Statistical Methods in the Physical Sciences*; Manchester Physics Series; Wiley: Chichester, UK, 1989.